

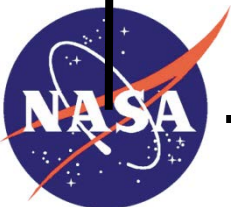
**GSFC JPSS CMO
August 21, 2014
Released**

**Joint Polar Satellite System (JPSS) Ground Project
Code 474
474-00040**

**Joint Polar Satellite System (JPSS)
VIIRS Surface Albedo
Algorithm Theoretical Basis Document
(ATBD)**

For Public Release

The information provided herein does not contain technical data as defined in the International Traffic in Arms Regulations (ITAR) 22 CFC 120.10. This document has been approved For Public Release.



National Aeronautics and
Space Administration

**Goddard Space Flight Center
Greenbelt, Maryland**

Joint Polar Satellite System (JPSS) VIIRS Surface Albedo Algorithm Theoretical Basis Document (ATBD)

JPSS Electronic Signature Page

Prepared By:

Ray Godin

JPSS Data Products and Algorithms, EDR Lead

(Electronic Approvals available online at https://jpssmis.gsfc.nasa.gov/mainmenu_dsp.cfm)

Approved By:

Eric Gottshall

DPA Manager

(Electronic Approvals available online at https://jpssmis.gsfc.nasa.gov/mainmenu_dsp.cfm)

**Goddard Space Flight Center
Greenbelt, Maryland**

Preface

This document is under JPSS Ground AERB configuration control. Once this document is approved, JPSS approved changes are handled in accordance with Class I and Class II change control requirements as described in the JPSS Configuration Management Procedures, and changes to this document shall be made by complete revision.

Any questions should be addressed to:

JPSS Ground Project Configuration Management Office
NASA/GSFC
Code 474
Greenbelt, MD 20771

Change History Log

Revision	Effective Date	Description of Changes (Reference the CCR & CCB/ERB Approve Date)
Original	04/22/2011	474-CCR-11-0055: This version baselines D43755, VIIRS Surface Albedo Algorithm Theoretical Basis Document ATDB (ref y2398), Rev D dated 07/14/2010 as a JPSS document, version Rev -. This is the version that was approved for NPP launch. Per NPOESS CDFCB - External, Volume V – Metadata, doc number D34862-05, this has been approved for Public Release into CLASS. This CCR was approved by the JPSS Algorithm ERB on April 22, 2011.
A	03/13/2013	474-CCR-13-0904: This CCR was approved by the JPSS Algorithm ERB on March 13, 2013. Changes affect Table 3.8 and Appendix A.2.
B	05/28/2014	474-CCR-14-1722: This CCR was approved by the JPSS Algorithm ERB on May 28, 2014. Changes affect Section 3.3.2, 3.3.2.1.2.2, 3.6, and Table 3.8. Added Appendix D.

Northrop Grumman Space & Mission Systems Corp.
Space Technology
One Space Park
Redondo Beach, CA 90278



**Engineering & Manufacturing Development (EMD) Phase
Acquisition & Operations Contract**

CAGE NO. 11982

**Surface Albedo Algorithm Theoretical
Basis Document ATBD (ref Y2398)**

Document Number: D43755

Document Date: 07/14/2010

Revision: D

PREPARED BY: _____
Alain Sei, Models & Simulations

ELECTRONIC APPROVAL SIGNATURES:



Merit Shoucri, Models & Simulation Lead

Prepared by
Northrop Grumman Space Technology
One Space Park
Redondo Beach, CA 90278

Prepared for
Department of the Air Force
NPOESS Integrated Program Office
C/O SMC/CIK
2420 Vela Way, Suite 1467-A8
Los Angeles AFB, CA 90245-4659

Under
Contract No. F04701-02-C-0502

DISTRIBUTION STATEMENT F: Distribution statement "F" signifies that further dissemination should only be made as directed by the controlling DoD Office (NPOESS IPO). Ref DODD 5230.24.

Northrop Grumman Space & Mission Systems Corp. Space Technology One Space Park Redondo Beach, CA 90278		 	
Revision/Change Record		Document Number	D43755
Revision	Document Date	Revision/Change Description	Pages Affected
---	1/24/2007	Initial PCIM Release to bring document into Matrix Accountability. Reference original document number: Y2398 delivered in 2004	All
A	3/31/2008	Modifications to extend BPSA algorithm to process sea ice pixels. ECR A-147	29, 82-99
B	3/01/2010	In preparation for Public Release of this ATBD, the following administrative changes were made: all ITAR markings were removed, and Distribution Statement F added.	All
C	6/16/2010	Fixed typographical error in the Roujean kernel definition in Table 3.6	20
D	7/14/2010	Removed TBx from document in Table 3.9 Update solar angle threshold ECR A-318B	iii, ix, 30 9

3.4 ALGORITHM SENSITIVITY STUDIES 31

 3.4.1 EDR Requirements..... 31

 3.4.2 Performance Metrics 32

 3.4.3 Individual Error Sources 34

 3.4.3.1 Past Sensor Error Evaluations 34

 3.4.3.2 Atmospheric Correction Errors 36

 3.4.3.3 BRDF Effects..... 37

 3.4.3.4 Narrow to Broadband Conversion..... 40

 3.4.3.5 TOA Reflectance Errors..... 42

 3.4.3.6 BPSA Intrinsic Errors 52

3.5. PRACTICAL CONSIDERATIONS..... 55

 3.5.1. Numerical Computation Considerations 55

 3.5.2. Programming and Procedural Considerations..... 55

 3.5.3. Configuration of Retrievals..... 56

 3.5.4. Quality Assessment and Diagnostics..... 56

 3.5.5. Exception Handling 56

3.6. RETRIEVAL SAMPLES..... 56

 3.6.1. BRDF Retrieval 57

 3.6.2. Albedo Retrieval 58

 3.6.3. Albedo Sensitivity 62

3.7. VALIDATION 65

4.0 ASSUMPTIONS AND LIMITATIONS 68

 4.1 ASSUMPTIONS..... 68

 4.2 LIMITATIONS..... 68

5.0 REFERENCES..... 69

APPENDIX A..... 74

 VIIRS NARROWBAND TO BROADBAND LAND SURFACE ALBEDO
 CONVERSION..... 74

 References..... 77

APPENDIX B..... 78

 THE BPSA ALGORITHM FOR ESTIMATING LAND SURFACE BROADBAND
 SHORTWAVE ALBEDO FROM VIIRS 78

 References..... 82

APPENDIX C..... 83

 THE BPSA ALGORITHM FOR ESTIMATING SEA ICE SURFACE BROADBAND
 SHORTWAVE ALBEDO FROM VIIRS 83

References.....102

APPENDIX D.....103

THE BPSA ALGORITHM UPDATE FOR PROVISIONAL VERSION RELEASE103

LIST OF TABLES

Page

Table 2.1 The nine VIIRS spectral bands used in the baseline Surface Albedo algorithm. 9

Table 3.1. Inputs required by the Surface Albedo algorithm unit..... 12

Table 3.2. Outputs of the Surface Albedo algorithm unit. 13

Table 3.3. VIIRS input data for computing Surface Albedo EDR and Surface Albedo IP.13

Table 3.4 Parameter definitions relevant to the Surface Albedo EDR..... 15

Table 3.5 Volumetric scattering kernels used in VIIRS land surface albedo algorithm... 19

Table 3.6 Geometric-optical scattering kernels used in VIIRS land surface albedo algorithm..... 20

Table 3.7 Kernel model combinations 20

Table 3.8. Solar-view geometry grid for BPSA coefficients. 29

Table 3.9 VIIRS SRD prescribed requirements for the Surface Albedo EDR. 31

Table 3.10 Field data sets from NASA’s FIFE and BOREAS experiment..... 37

Table 3.11. Height (h/b) /Shape (b/r) sensitivity 38

Table 3.12. Indexed combinations of channels considered for conversion from narrow to broadband albedo for previous evaluation of the Lambertian-based regression algorithm. 41

Table 3.13. Summary of dimensions for the TOA Reflectance and BPSA stick modeling data set..... 42

Table 3.14. Results for the BPSA over snow, at the edge of the VIIRS scan. 53

Table C1 Sea Ice Physical Properties for New Young, First Year and Multi-year ice 86

Table C2. Physical Properties of Snow for the Global Surface Albedo Product 86

Table C3. Snow and Sea Ice Surface Parameter Ranges 87

Table C4. Northern Hemisphere Relative Ice Age Type Frequencies 91

Table C5. Southern Hemisphere Relative Ice Age Type Frequencies 91

LIST OF FIGURES

	<u>Page</u>
Figure 2.1 Summary of VIIRS design concepts and heritage.	6
Figure 2.2 VIIRS detector footprint aggregation scheme for building "pixels." Dimensions shown are approximate.	6
Figure 2.3 Benefits of VIIRS aggregation scheme in reducing pixel growth at edge of scan.....	7
Figure 2.4 VIIRS spectral bands, visible and near infrared.....	8
Figure 2.5 VIIRS spectral bands, short wave infrared.	8
Figure 3.1 Software processing architecture for the Surface Albedo EDR.	11
Figure 3.2 Software processing architecture for the Gridded Surface Albedo IP.....	12
Figure 3.3 Spectral decoupling of atmospheric and surface properties for derivation of broadband albedo.....	28
Figure 3.4 Plots of retrieved reflectance vs. measurement reflectance of data set ssa-obs.....	38
Figure 3.5. Histogram of the actual and retrieved reflectance using simulation data....	40
Figure 3.6. Narrow to broadband albedo conversion errors from previous evaluation of a Lambertian-based linear regression algorithm, using the combinations of channels listed in Table 9 for four different backgrounds.	42
Figure 3.7 TOA reflectance errors at 412 nm, for nadir and edge of scan, at solar zenith of 30 degrees (top) and 70 degrees (bottom), using both specified and predicted sensor performance as input.	44
Figure 3.8 TOA reflectance errors at 445 nm, for nadir and edge of scan, at solar zenith of 30 degrees (top) and 70 degrees (bottom), using both specified and predicted sensor performance as input.	45
Figure 3.9 TOA reflectance errors at 488 nm, for nadir and edge of scan, at solar zenith of 30 degrees (top) and 70 degrees (bottom), using both specified and predicted sensor performance as input.	46
Figure 3.10 TOA reflectance errors at 555 nm, for nadir and edge of scan, at solar zenith of 30 degrees (top) and 70 degrees (bottom), using both specified and predicted sensor performance as input.	47

Figure 3.11 TOA reflectance errors at 645 nm, for nadir and edge of scan, at solar zenith of 30 degrees (top) and 70 degrees (bottom), using both specified and predicted sensor performance as input. 48

Figure 3.12 TOA reflectance errors at 865 nm, for nadir and edge of scan, at solar zenith of 30 degrees (top) and 70 degrees (bottom), using both specified and predicted sensor performance as input. 49

Figure 3.13 TOA reflectance errors at 1240 nm, for nadir and edge of scan, at solar zenith of 30 degrees (top) and 70 degrees (bottom), using both specified and predicted sensor performance as input. 50

Figure 3.14 TOA reflectance errors at 1610 nm, for nadir and edge of scan, at solar zenith of 30 degrees (top) and 70 degrees (bottom), using both specified and predicted sensor performance as input. 51

Figure 3.15 TOA reflectance errors at 2250 nm, for nadir and edge of scan, at solar zenith of 30 degrees (top) and 70 degrees (bottom), using both specified and predicted sensor performance as input. 52

Figure 3.16 Albedo accuracy performance for the BPSA, spec and predicted, at edge of scan for a solar zenith of 30 degrees. Note negligible difference between spec and predicted sensor performance for calibration, assuming the algorithm is trained post-launch with real VIIRS data. 54

Figure 3.17 Albedo uncertainty performance for the BPSA, spec and predicted, at nadir for a solar zenith of 70 degrees. Nadir uncertainty requirement (fine product) is 0.03 threshold. 54

Figure 3.18 BRDF inversion results over the MODIS tile h08v05 for VIIRS DPSA (full inversion = green and yellow, magnitude inversion = red, history = white, fill value = magenta). 57

Figure 3.19 BRDF model parameter f0 over the MODIS tile h08v05 for VIIRS DPSA .. 58

Figure 3.20 VIIRS DPSA retrieved using the test VIIRS input data and artificial BRDF data. 59

Figure 3.21 VIIRS DPSA histogram. The values are scaled by 10000..... 60

Figure 3.22 VIIRS BPSA retrieved using the test VIIRS input data 61

Figure 3.23 VIIRS BPSA histogram. The values are scaled by 10000..... 62

Figure 3.24 Histogram of the DPSA difference if AOT increases 0.1 63

Figure 3.25 Histogram of the BPSA difference if TOA reflectance increases 2%..... 64

Figure 3.26 Histogram of the BPSA difference due to AOT model information error. ... 65

Figure A1 Fit using a linear regression Equation (A1)..... 76

Figure A2 Fit using Equation (A2) 76

Figure B1 Illustration of the DPSA Algorithm 78

Figure C1. Processing Flow of Snow Covered Sea Ice BRDF and TOA Albedo Generation..... 85

Figure C2: Relative Sea Ice thickness from the Ross Sea used to derive Ice classification for the Southern hemisphere. 92

Figure C3. NSIDC partial ice concentrations for New Young (upper left), First Year (upper middle) and Multi-year (upper right). NGST derived ice age classification map (lower left) and histogram of ice age classification map values. 93

Figure C4: Sensitivity of Directional Hemispheric Reflectance to soot concentration. ... 94

Figure C5: Sensitivity of Bi-hemispheric Reflectance (albedo) to soot particle radius for coarse grain (1000 μ m) dirty snow albedo is also plotted for reference..... 95

Figure C6: Comparison of computed and observed sea ice albedoes 95

Figure C7: Comparison of computed and observed sea ice albedoes 96

Figure C8: Sensitivity of albedo to snow depth (1) 96

Figure C9: Sensitivity of albedo to snow depth (2) 97

Figure C10: Sensitivity of albedo to snow depth (3) 97

Figure C11: Sensitivity of albedo to snow depth (4) 98

Figure C12: Ice age classification derived from NSIDC Data (1) 98

Figure C13: Ice age classification derived from NSIDC Data (2) 99

Figure C14: Ice age classification derived from NSIDC Data (3) 100

Figure C15: Ice age classification derived from NSIDC Data (4) 100

Figure C16: Regression for the entire dataset 101

Figure C17: Regression with solar zenith angle binning 101

GLOSSARY OF ACRONYMS

ACE	Aerosol Characterization Experiment
ADD	Algorithm Data Definition
AERONET	Aerosol Robotic Network
AirMISR	Airborne Multi-angle Imaging Spectroradiometer
ALI	Advanced Land Imager
AOT	Aerosol Optical Thickness
APAR	Absorbed Photosynthetically Active Radiation
ARM CART	Atmospheric Radiation Measurement, Cloud and Radiation Testbed
ASAS	Advanced Solid-state Array Spectroradiometer
ATBD	Algorithm Theoretical Basis Document
ATS	Applications Technological Satellite
ATSR	Along-Track Scanning Radiometer
AVHRR	Advanced Very High Resolution Radiometer
AVIRIS	Airborne Visible and Infrared Imaging Spectrometer
AVP	Albedo Validation Plan
BOREAS	Boreal Ecosystem/Atmosphere Study
BPSA	Bright Pixel Sub-Algorithm (MODIS albedo algorithm)
BRDF	Bidirectional Reflectance Distribution Function
BRF	Bidirectional Reflectance Factor
DoD	Department of Defense
DPSA	Dark Pixel Sub-Algorithm (Regression algorithm)
DISORT	DIScrete-Ordinate-method Radiative Transfer
EDR	Environmental Data Record
EOPACE	Electro-optic Propagation Assessment in Coastal Environment
EOS	Earth Observing System
ETM+	Enhanced Thematic Mapper plus (+) – Landsat 7 satellite
FIFE	First ISLSCP Field Experiment
FOV	Field of View
GCM	General Circulation Model
GIFOV	Ground Instantaneous Field of View

GPS	Global Positioning System
HAPEX	Hydrological-Atmospheric Pilot Experiment
HCS	Horizontal Cell Size
HSR	Horizontal Spatial Resolution
ICD	Interface Control Document
ID	Identification Number of Input/Output Data for Processing Modules
IFOV	Instantaneous Field of View
IP	Intermediate Product
IPO	Integrated Program Office
ISIS	Integrated Surface Irradiance Study
ISLSCP	International Satellite Land Surface Climatology Project
LAI	Leaf Area Index
TM	Enhanced Thematic Mapper plus (+) – Landsat 5 satellite and earlier
LLLS	Low Light Level Sensor
LOWTRAN	LOW resolution TRANsmission model
LQF	Land Quality Flag
LUT	Look-up table
MAS	MODIS Airborne Simulator
MFRSR	Multifilter Rotating Shadowband Radiometer
MISR	Multiangl e Imaging Spectroradiometer
MMR	Modular Multiband Radiometer
MODIS	Moderate Resolution Imaging Spectroradiometer
MODTRAN	MODerate resolution TRANsmission model
MTF	Modulation Transfer Function
NASA	National Aeronautics and Space Administration
NBAR	Nadir BRDF-Adjusted Reflectance
NCEP	National Centers for Environmental Prediction
NDVI	Normalized Difference Vegetation Index
NIR	Near Infrared
NOAA	National Oceanic and Atmosphere Administration
NPP	NPOESS Preparatory Project
NPOESS	National Polar-orbiting Operational Environmental Satellite System

OLS	Operational Linescan System
OTTER	Oregon Transect Ecosystem Research
PARABOLA	Portable Apparatus for Rapid Acquisition of Bidirectional Observations Atmosphere
POLDER	Polarization and Directionality of the Earth's Reflectances
PSF	Point Spread Function
RDR	Raw Data Record
RMS	Root Mean Square
SBRS	Santa Barbara Remote Sensing
SCAR-B	Smoke, Clouds, and Radiation (Brazil)
SDR	Sensor Data Record
SDSM	Solar Diffuser Stability Monitor
SeaWiFS	Sea-viewing, Wide-Field-of-view Sensor
SNR	Signal-to-Noise Ratio
SRD	Sensor Requirements Document
SWIR	Short Wave Infrared
TARFOX	Tropospheric Aerosol Radiative Forcing Observational Experiment
THEMIS	Thermal Emission Imaging System
TIROS	Television/Infrared Observation Satellite
TM	Landsat Thematic Mapper
TOA	Top-of-Atmosphere
TOC	Top-of-Canopy
VIIRS	Visible/Infrared Imager/Radiometer Suite

ABSTRACT

This document describes the algorithm for creating the Land Surface Albedo Environmental Data Record (EDR) as part of the requirements for the Visible/Infrared Imager/Radiometer Suite (VIIRS), the primary visible and infrared sensor to be flown onboard the platforms of the National Polar-orbiting Operational Environmental Satellite System (NPOESS) and the NPOESS Preparatory Project (NPP). Surface Albedo is defined in the VIIRS System Requirements Document (PS154650) to be a ratio of the outgoing to incoming broadband fluxes at the Earth's surface, extending spectrally from 0.4 to 4.0 μm . The requirements for the Surface Albedo are challenging for even moderately bright surfaces, particularly with respect to precision. This EDR encompasses a Moderate Resolution Imaging Spectroradiometer (MODIS)-like approach for dark surfaces such as vegetation and water, combined with a regression approach for bright surfaces such as desert and snow. This approach will first produce an intermediate product (IP) that contains daily, gridded surface Bi-directional Reflectance Distribution Function (BRDF) information using a 16-day Gridded Daily Surface Reflectance IP data set. The gridded BRDF information will then be used to derive black-sky and white-sky albedo values in moderate pixel resolution, which are further interpolated into the pixel spectral albedo value using an atmospheric diffusion coefficient derived from Aerosol Optical Thickness (AOT) data. The spectral albedo values are then converted into the broadband surface albedo for the dark surfaces. A regression algorithm is run using the Top Of Atmosphere (TOA) reflectance values at the pixel level, for bright pixels. Preliminary analyses of the regression approach suggest that the requirements are also achievable for snow and desert. However, verification of these results requires more rigorous and realistic treatment of surface bi-directional effects. Recent validations of the MODIS algorithm performance instill significant confidence that the EDR requirements can be met for dark surfaces. The risk mitigation strategy for discontinuities in albedo fields involves executing the dark pixel and bright pixel algorithms for all clear pixels.

1.0 INTRODUCTION

The purpose, scope, relevant VIIRS documents and revision history of this document are briefly described in this section. Section 2 gives an overview of the EDR retrieval objectives and operations concept. Section 3 describes the baseline algorithm, its input data requirements, the theoretical background, sensitivity analyses, error budgeting, and some practical considerations. Section 4 lists the assumptions and limitations associated with the algorithm presented here, and Section 5 presents the references cited.

1.1 PURPOSE

This Algorithm Theoretical Basis Document (ATBD) explains the physical and mathematical background for an algorithm to derive the Land Surface Albedo Environmental Data Record (EDR) and the Intermediate Product (IP) as a part of the requirements for the Visible/Infrared Imager/Radiometer Suite (VIIRS). VIIRS is the primary visible and infrared instrument to be flown onboard the platforms of the National Polar-orbiting Operational Environmental Satellite System (NPOESS). This document provides an overview of the required input data, a physical and mathematical description of the algorithm and its predicted performance, assumptions and limitations, and a sensitivity study of the described algorithm. The EDR described in this document is one of over two dozen EDRs within the NPOESS/VIIRS system.

1.2 SCOPE

This document covers the theoretical basis for the derivation of the Surface Albedo EDR and the Gridded Surface Albedo IP. Focus and emphasis are placed on the two sub-algorithms baselined for operational retrievals. Surface reflectance values, now required as an intermediate derived product for the Surface Albedo EDR, are retrieved by a separate algorithm, which is described in the Surface Reflectance ATBD [Y2411].

1.3 VIIRS DOCUMENTS

This document contains references to other VIIRS documents that are given in italicized brackets. Most of the references are indexed to the Raytheon Santa Barbara Remote Sensing (SBRS) Y-number database for officially released documents. The VIIRS documents thus cited are listed below:

Y1629 VIIRS Testbed Sensor Modeling Efforts, Phase I. Raytheon Systems Company Internal Memorandum

D43313 (Y2388) VIIRS Aerosol Optical Thickness and Particle Size ATBD

D43757 (Y2400) VIIRS Vegetation Index ATBD

D43759 (Y2402) VIIRS Surface Type ATBD

D43765 (Y2411) VIIRS Surface Reflectance ATBD

D43776 (Y2412) VIIRS Cloud Mask ATBD
Y2468 VIIRS Operations Concept Document
Y2469 VIIRS Context Level Software Architecture
Y2470 VIIRS Interface Control Document (ICD)
Y2474 VIIRS Land Module Level Software Architecture
Y2483 VIIRS Surface Albedo Unit Level Detailed Design
Y3234 VIIRS Snow Cover Unit Level Detailed Design
Y3236 VIIRS Software Integration and Test Plan
Y3237 VIIRS Algorithm Verification and Validation Plan
D43777 (Y3261) VIIRS Radiometric Calibration ATBD
Y3270 VIIRS System Verification and Validation Plan
Y6635 VIIRS Algorithm Software Development Plan
Y6661 VIIRS Algorithm Software Maturity Assessment
Y7040 VIIRS Algorithm/Data Processing Technical Report
D43778 (Y7051) VIIRS Earth Gridding ATBD
SS154650 VIIRS System Specification
PS154650 VIIRS Sensor Specification

1.4 REVISIONS

This is revision A of the Surface Albedo ATBD, dated March 2008. Version 5 revision 1 was dated May 2004. The major changes in this revision are 1) a detailed description of the algorithm to generate the Gridded Albedo IP, 2) criterion discussions for the Dark Pixel Sub-Algorithm (DPSA) and Bright Pixel Sub-Algorithm (BPSA) algorithms, 3) narrowband-to-broadband conversion algorithms and coefficients. The original version of this document was dated July 1998. Version 1 was dated September 1998. Version 2 was dated June 1999. Version 3 was dated May 2000. The authors of this revision recognize the contributions to this and previous versions of this document made by Peter Vogt, Dr. Shunlin Liang, Dr. Crystal Schaaf, and Dr. Feng Gao.

2.0 EXPERIMENT OVERVIEW

2.1 OBJECTIVES OF SURFACE ALBEDO RETRIEVAL

Albedo specifies the fraction of incident broadband solar radiation that is reflected at the Earth's surface. It is a critical parameter for characterizing the earth's radiative regime and its impact on biospheric and climatic processes (Dickinson, 1983; Mintz, 1984; Running, 1990; Saunders, *et al.* 1990; Henderson-Sellers and Pitman, 1992; Henderson-Sellers *et al.*, 1993; Running *et al.*, 1994; Dickinson, 1995; Lofgren, 1995; Sellers *et al.*, 1996)). Surface Albedo defines the lower boundary layer for atmospheric radiative transfer and details the total shortwave energy input into the biosphere and thus is a key component of the surface energy budget. The spatial and temporal distribution of surface properties captured by the bi-directional reflectance distribution function (BRDF) and albedo features reflect a variety of natural and human influences on the surface that are of interest to global climate research.

Historically, land cover maps (Matthews, 1983; Wilson and Henderson-Sellers, 1985) have been used to derive the albedo. Satellite data offer a unique opportunity to create maps of land cover or any other parameter of interest (Leaf Area Index [LAI], Fraction of Absorbed Photosynthetically Active Radiation (FAPAR), Net Primary Production, etc.). They permit the global observation and quantification of the temporal and spatial distribution and variability of different land cover types. The albedo of a given land cover type can change quickly through processes such as deforestation, soil moisture change, agricultural expansion, harvesting, flooding, and snow melting. These changes result in a modification of the hydrological and thermal state of the surface on local to regional scale (e.g. Nemani *et al.*, 1996). On a long-term scale, they might result in severe drought periods as for the Sahel-region (Charney *et al.*, 1977).

Rapid growth in human population and industrialization within the past hundred years has led to a significant increase in biomass burning. This apparently results in a noticeable augmentation of atmospheric CO₂ concentration during this same period (Graedel and Crutzen, 1994). The thermal radiation emitted by the earth is absorbed and re-radiated by methane, CO₂, and especially water vapor. This process induces atmospheric heating via the greenhouse effect. This heating directly interacts with the albedo via snow/ice melting or desertification. Thus, an accurate assessment of the albedo is crucial for the evaluation of climate change. Complex models have been designed to assess the effect of anthropogenic changes to the environment. Ecosystem studies and general circulation models (GCMs) critically depend on the surface albedo in order to forecast the impact of natural and anthropogenic changes to the environment (Sellers *et al.*, 1994; Lean and Rowntree, 1993; Garratt, 1993; Chase *et al.*, 1996; Culf *et al.*, 1995). They forecast future developments and permit the appropriate economic, social and political reactions. These reactions might include changes in land use, provisions to reduce greenhouse gas emissions, and the redirection of scientific research aims in order to better understand the chemical and biogeophysical interaction between climate change and the anthroposphere.

Spectral radiance (or reflectance) values in land remote sensing are a function of many components, which include the continuously varying incident solar irradiance (e.g., geometry and spectral distribution), atmospheric conditions (e.g., water vapor and aerosols),

meteorological conditions (e.g., cloud cover, temperature, wind field, relative humidity), reflectance properties of the surface (e.g., spatial, spectral, and biophysical), and sensor viewing conditions (geometry, time of observation). The spectral bidirectional reflectance factor (BRF) describes these components while the spatial distribution of the BRFs is provided by the BRDF. A surface displaying identical BRFs for all directions is called isotropic or Lambertian. The assumption of a Lambertian surface leads to very simple algorithmic approaches for albedo retrieval, but research in the past 1-2 decades provides evidence that the Earth's surface is non-Lambertian (anisotropic). Kimes and Sellers (1985) demonstrated the importance of considering BRDF effects. They showed that when BRDF effects are neglected, errors in spectral albedo of up to 40 percent could occur. Off-nadir viewing data is no longer treated as "noisy data" with respect to nadir observation but as a potential new information source to determine:

- Vegetation-specific characteristics (e.g., LAI, crown size, ground cover fraction; Pinty and Verstraete, 1991; Kimes and Sellers, 1985).
- Land cover classification (Leroy *et al.*, 1997).
- Water leaving radiances, and thus marine phytoplankton concentration, in areas exposed to sun glint at nadir observation (Gordon *et al.*, 1983).
- Atmospheric phase-function (Martonchik and Diner, 1992).

Partially in response to these issues, different sensors have been built with the capability to increase our understanding of BRDF effects, including the Moderate Resolution Imaging Spectroradiometer (MODIS), the Multi-angle Imaging SpectroRadiometer (MISR), the Along Track Scanning Radiometer (ATSR), and POLarization and Directionality of the Earth's Reflectances (POLDER). These sensors offer more spectral channels and directions of observation than had been previously available. As a result, the quality of albedo retrievals is expected to improve. The VIIRS algorithm will leverage this algorithm technological progress to provide an operational albedo product that will build and improve upon an already burgeoning heritage.

2.2 INSTRUMENT CHARACTERISTICS

The VIIRS instrument will now be briefly described to clarify the context of the descriptions of the Surface Albedo EDR presented in this document. VIIRS can be pictured as a convergence of three existing sensors, two of which have seen extensive operational use at this writing.

The Operational Linescan System (OLS) is the operational visible/infrared scanner for the Department of Defense (DoD). Its unique strengths are controlled growth in spatial resolution through rotation of the ground instantaneous field of view (GIFOV) and the existence of a low-level light sensor (LLLS) capable of detecting visible radiation at night. OLS has primarily served as a data source for manual analysis of imagery. The Advanced Very High Resolution Radiometer (AVHRR) is the operational visible/infrared sensor flown on the National Oceanic and Atmospheric Administration (NOAA) Television Infrared Observation Satellite (TIROS-N) series of satellites (Planet, 1988). Its unique strengths are

low operational and production cost and the presence of five spectral channels that can be used in a wide number of combinations to produce operational and research products. In December 1999, NASA launched the EOS morning satellite, *Terra*, which includes MODIS. This sensor possesses an unprecedented array of thirty-two spectral bands at resolutions ranging from 250 m to 1 km at nadir, allowing for currently unparalleled accuracy in a wide range of satellite-based environmental measurements.

VIIRS will reside on a platform of the NPOESS series of satellites. It is intended to be the product of a convergence between DoD, NOAA and NASA in the form of a single visible/infrared sensor capable of satisfying the needs of all three communities, as well as the research community beyond. As such, VIIRS will require three key attributes: high spatial resolution with controlled growth off nadir, minimal production and operational cost, and a large number of spectral bands to satisfy the requirements for generating accurate operational and scientific products.

Figure 2.1 illustrates the design concept for VIIRS, designed and built by Raytheon Santa Barbara Remote Sensing (SBRS). At its heart is a rotating telescope scanning mechanism that minimizes the effects of solar impingement and scattered light. VIIRS is essentially a combination of the Sea-viewing, Wide-Field-of-View Sensor (SeaWiFS) fore-optics and an all-reflective modification of MODIS/THERMIS (THERmal EMISSION Imaging System) aft-optics. Calibration is performed onboard using a solar diffuser for short wavelengths and a blackbody source and deep space view for thermal wavelengths. A solar diffuser stability monitor (SDSM) is also included to track the performance of the solar diffuser. The nominal altitude for NPOESS will be 833 km. The VIIRS scan will therefore extend to 56 degrees on either side of nadir.

The VIIRS SRD places explicit requirements on spatial resolution for the Imagery EDR. Specifically, the horizontal spatial resolution (HSR) of bands used to meet threshold Imagery EDR requirements must be no greater than 400 m at nadir and 800 m at the edge of the scan. This led to the development of a unique scanning approach which optimizes both spatial resolution and Signal to Noise Ratio (SNR) across the scan. The concept is summarized in Figure 2.2 for the imagery bands; the nested lower resolution radiometric bands follow the same paradigm at exactly twice the size. The VIIRS detectors are rectangular, with the smaller dimension along the scan. At nadir, three detector footprints are aggregated to form a single VIIRS "pixel." Moving along the scan away from nadir, the detector footprints become larger both along track and along scan, due to geometric effects and the curvature of the Earth. The effects are much larger along scan. At around 32 degrees in scan angle, the aggregation scheme is changed from 3x1 to 2x1. A similar switch from 2x1 to 1x1 aggregation occurs at 48 degrees. The VIIRS scan consequently exhibits a pixel growth factor of only 2 both along track and along scan, compared with a growth factor of 6 along scan which would be realized without the use of the aggregation scheme. Figure 2.3 illustrates the benefits of the aggregation scheme for spatial resolution.

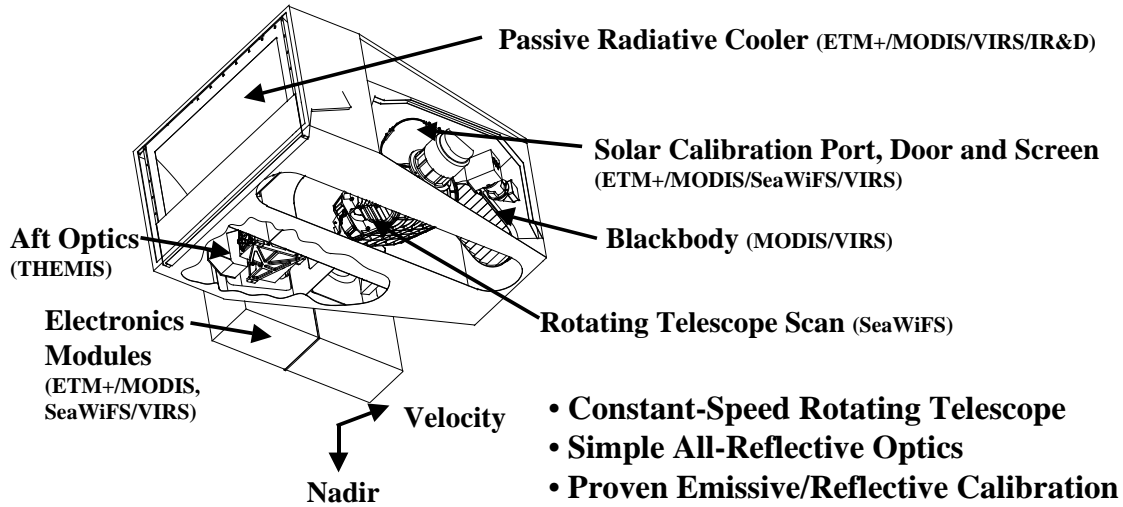


Figure 2.1 Summary of VIIRS design concepts and heritage.

Fine-Resolution Bands

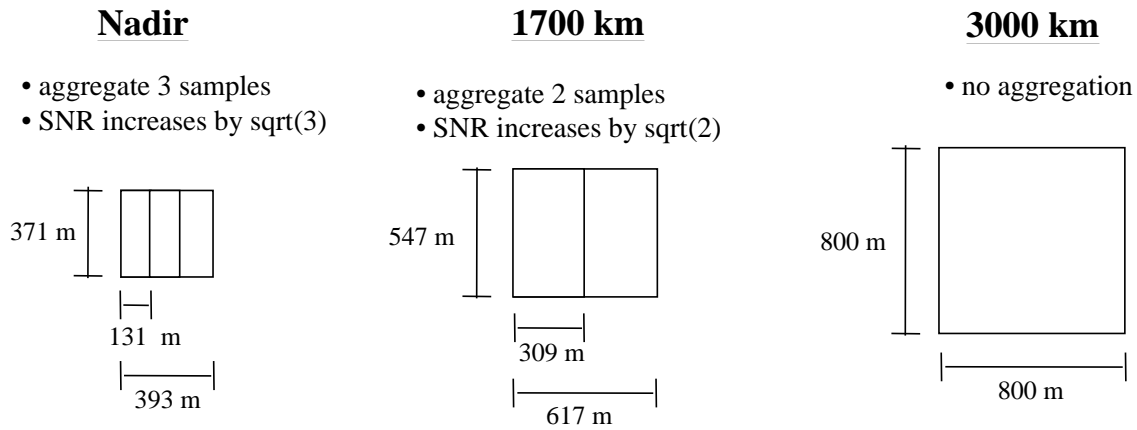


Figure 2.2 VIIRS detector footprint aggregation scheme for building "pixels." Dimensions shown are approximate.

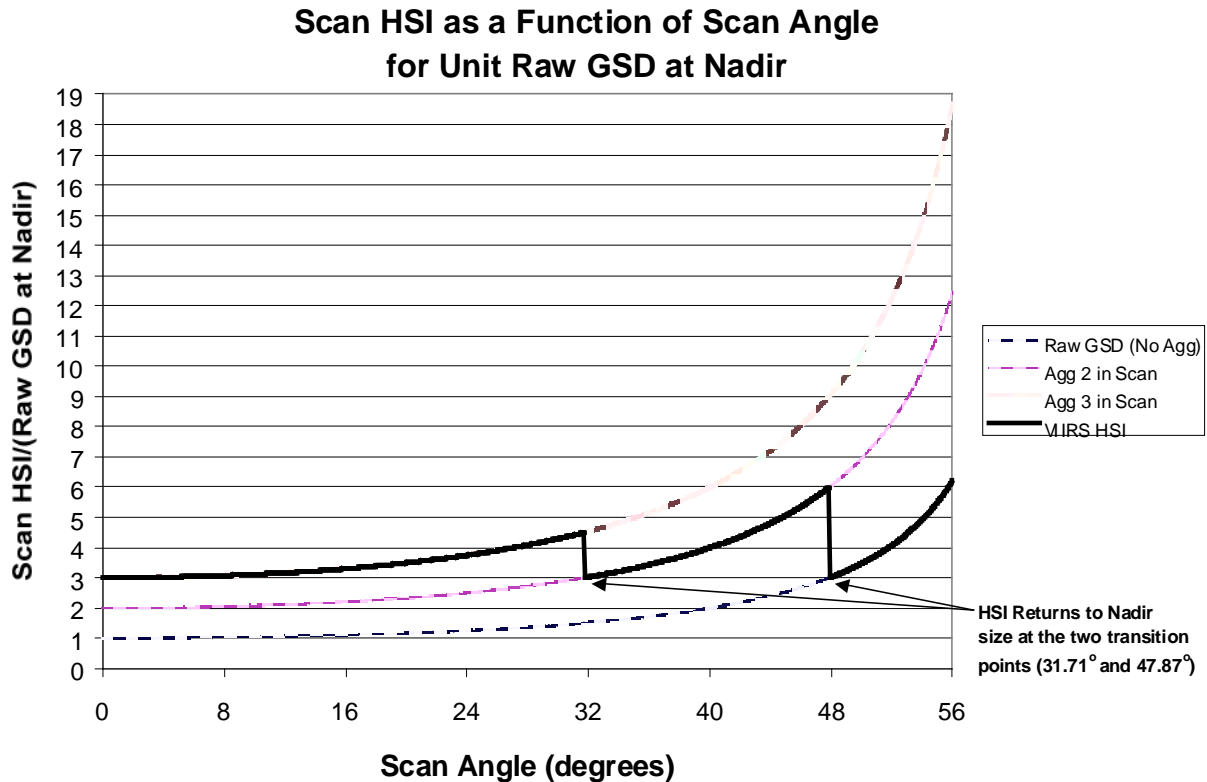


Figure 2.3 Benefits of VIIRS aggregation scheme in reducing pixel growth at edge of scan.

This scanning approach is extremely beneficial for the retrieval of land products such as Surface Albedo. The increasing importance of land cover change detection makes high spatial resolution in surface albedo and its input reflectance values much more important, and SNR becomes a secondary issue. The positioning of the VIIRS spectral bands in the range required by the Surface Albedo EDR is summarized in Figure 2.4 and Figure 2.5. Details of the radiometric, spectral, and spatial performance of these bands can be found in the VIIRS Sensor Specification [PS154650].

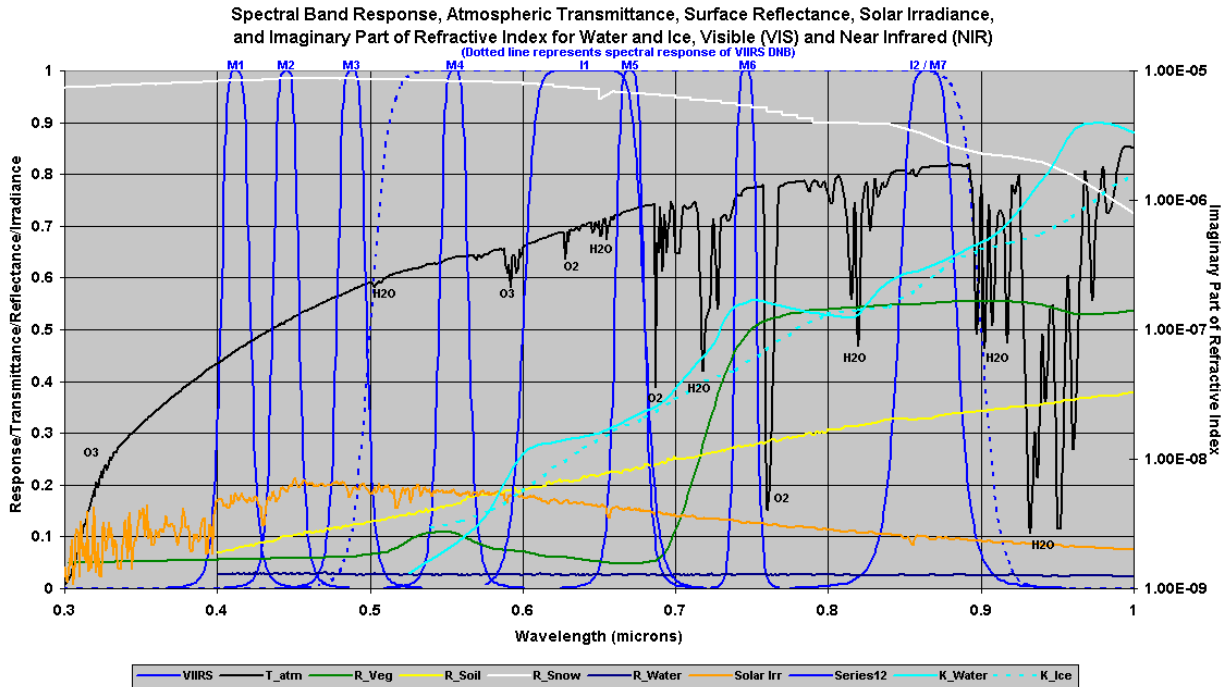


Figure 2.4 VIIRS spectral bands, visible and near infrared.

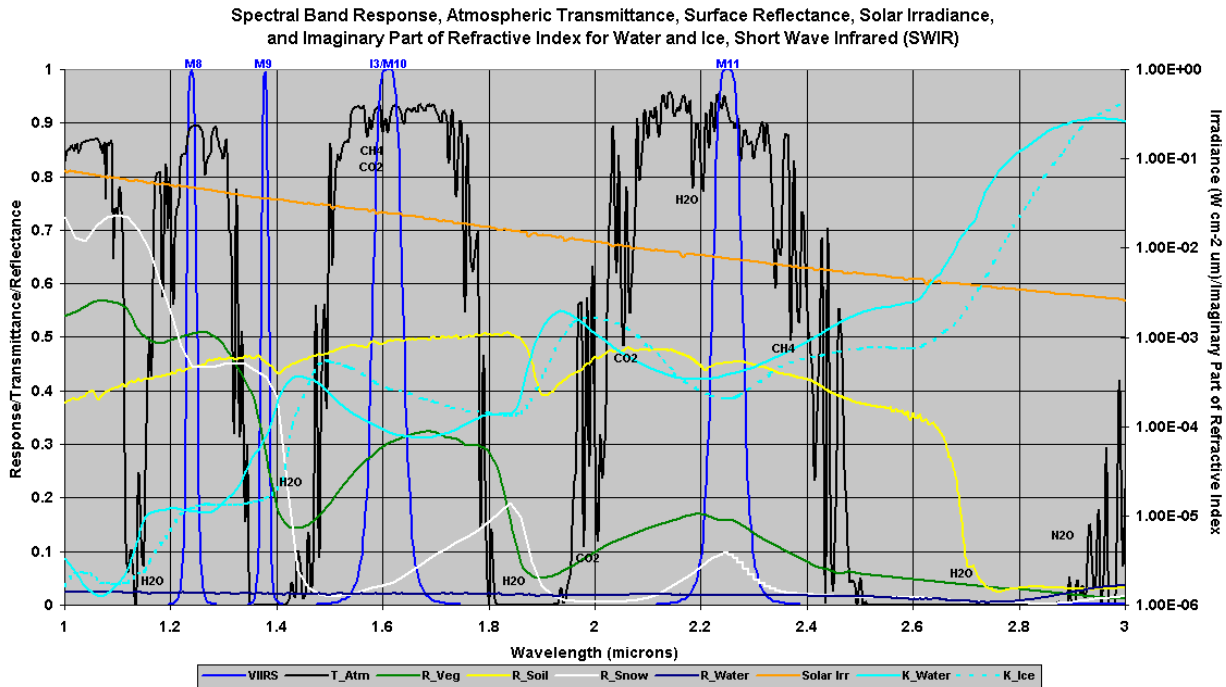


Figure 2.5 VIIRS spectral bands, short wave infrared.

2.3 RETRIEVAL STRATEGY

The Surface Albedo EDR will be computed for all clear, daytime, land surface pixels at the VIIRS moderate resolution (approximately 750 m at nadir). A clear moderate resolution pixel

in this context has been flagged either “definitely clear,” “probably clear,” or “probably cloudy” by the VIIRS Cloud Mask. If the pixel is “probably clear” or “probably cloudy,” the retrieval will be flagged in the generalized Land Quality Flag (LQF) output appended to the VIIRS Surface Reflectance Intermediate Product (IP) and copied to the Surface Albedo EDR output file. Retrievals will also be generated for pixels that have been categorized as thin cirrus by the VIIRS Cloud Mask [Y2412, VIIRS Cloud Mask ATBD]. The strategy for correcting thin cirrus and the limits of applying this correction are discussed in [VIIRS Surface Reflectance ATBD]. A daytime pixel is one for which the average solar zenith angle is less than or equal to 85 degrees. Pixels with a solar zenith angle of 65 degrees or higher are flagged in the LQF output. Nine spectral bands from VIIRS are used to generate the Surface Albedo EDR; these are listed in Table 2.1. In Version 4 of this ATBD, imagery bands were used in place of the presently listed M5, M7, and M10 bands. We have altered this approach to exclusive use of moderate resolution bands, to address concerns of matching point spread functions between the different resolutions.

Table 2.1 The nine VIIRS spectral bands used in the baseline Surface Albedo algorithm.

Band Name	Center (microns)	Width (microns)	Nadir Spatial Resolution (m)
M1	.412	.020	750
M2	.445	.018	750
M3	.488	.020	750
M4	.555	.020	750
M5	.672	.020	750
M7	.865	.039	750
M8	1.24	.020	750
M10	1.61	.060	750
M11	2.25	.050	750

There are two sub-algorithms utilized to produce the Surface Albedo EDR. The dark pixel sub-algorithm (DPSA) is based on the MODIS approach, and is used for all dark surfaces, including most vegetation and water. The bright pixel sub-algorithm (BPSA) is a regression approach, and is used for all bright surfaces, including snow, desert, and many instances of bare soil. Both algorithms will be executed for all pixels satisfying the conditions listed in the previous paragraph. A dark pixel or bright pixel flag is inherited from Aerosol Optical Thickness IP (see Y2388) that indicates the preference of the DPSA and BPSA products. This preference flag recommends which albedo product best represents the true albedo. The DPSA involves the production of the Gridded Surface Albedo IP, which contains the

BRDF information as well as Nadir BRDF-Adjusted Reflectance (NBAR) values, in 1-km ground resolution. In real time processing, the BRDF information is applied to derive black sky and white sky albedos that are interpolated to produce the albedo EDR. As a result, the surface BRDF information and NBAR values are available independently from the instantaneous retrieval of albedo in VIIRS pixels.

3.0 ALGORITHM DESCRIPTION

3.1 PROCESSING OUTLINE

Figure 3.1 illustrates the software architecture for the real-time processing of the Surface Albedo EDR. The reader is directed to [Y2474] for the latest official architecture. Once a pixel has qualified as land surface, daytime and cloud clear, the DPSA will be run using the Gridded Surface Albedo IP, the generation of which is shown pictorially in Figure 3.1(again, the reader should consult [Y2474] for the most up-to-date configuration). The BPSA will be applied using the VIIRS 750-m Earth View Sensor Data Record (SDR [Y3261]). The details of the DPSA and the BPSA are presented in Sections 3.3.2.1 and 3.3.2.2, respectively.

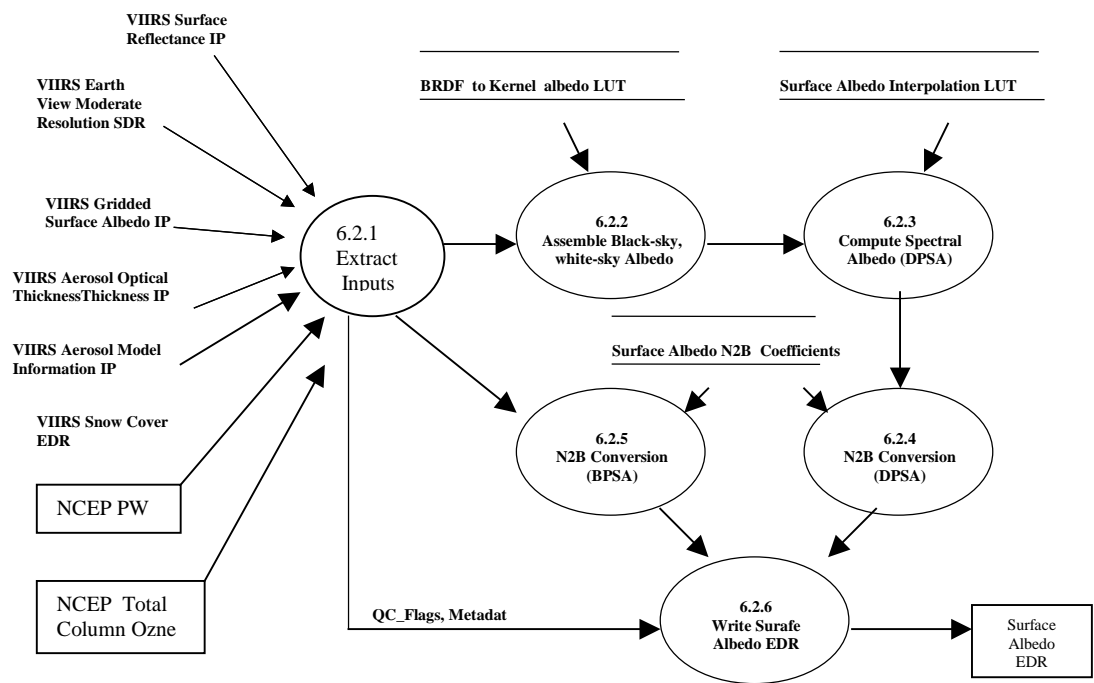


Figure 3.1 Software processing architecture for the Surface Albedo EDR.

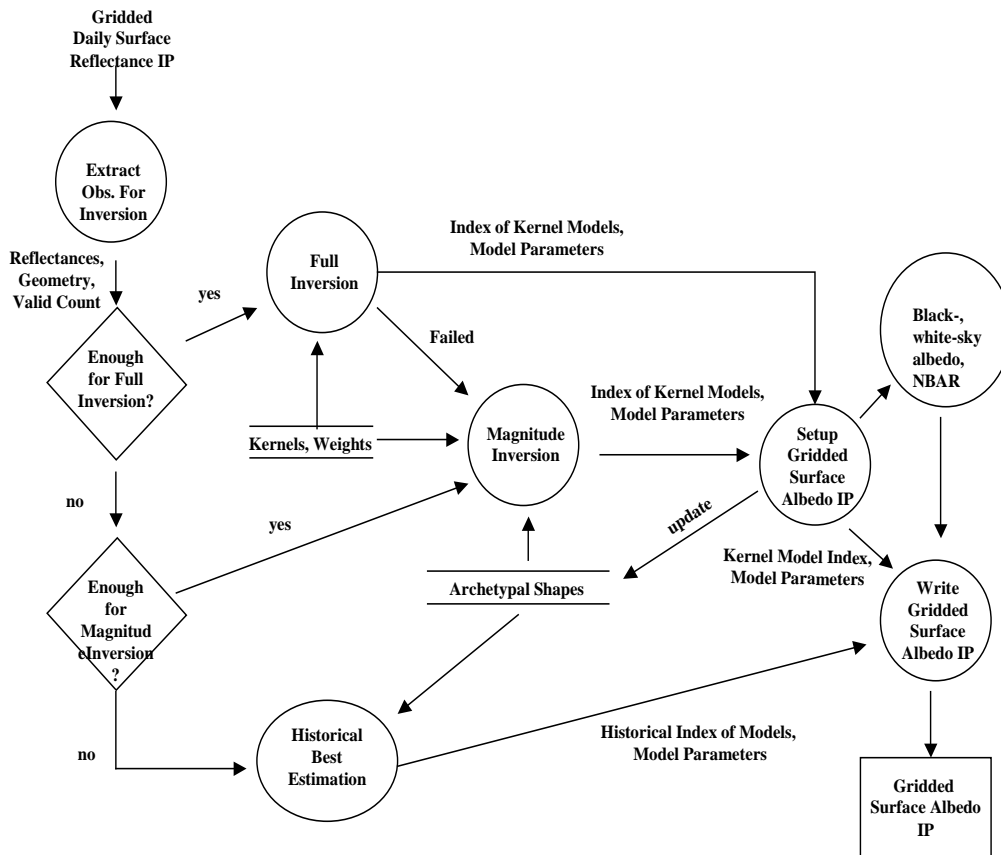


Figure 3.2 Software processing architecture for the Gridded Surface Albedo IP.

3.2 ALGORITHM INPUT AND OUTPUT

The required inputs for the Surface Albedo algorithm unit are listed in Table 3.1, while the outputs of it are listed in Table 3.2.

Table 3.1. Inputs required by the Surface Albedo algorithm unit.

Input Data	Source of Data	Reference
VIIRS 750-m Earth View SDR	VIIRS Build SDR Module	[Y3261]
VIIRS Surface Reflectance IP	VIIRS Land Module	[Y2411]
VIIRS Aerosol Optical Thickness IP	VIIRS Aerosol Module	[Y2388]
VIIRS Aerosol Model Information IP	VIIRS Aerosol Module	[Y2388]
VIIRS Snow Cover EDR	VIIRS Snow and Ice Module	[Y3234]

VIIRS Gridded Daily Surface Reflectance IP	Build SDR Module	[Y7051]
Historical BRDF Archetype	Offline Processing	<i>This document</i>
NCEP-Total Column Ozone	Offline Processing	<i>Auxiliary Data Set</i>
NCEP-Precipitable Water	Offline Processing	<i>Auxiliary Data Set</i>

Table 3.2. Outputs of the Surface Albedo algorithm unit.

Output products	Source of Data	Purpose
Land Surface BRDF Information	VIIRS Gridded Albedo IP	<i>Input for Albedo EDR</i>
Mean Solar Zenith Angle (MSZA)	VIIRS Gridded Albedo IP	<i>Input for NBAR</i>
Land Surface NBAR at MSZA	VIIRS Gridded Albedo IP	<i>Required by Gridding Module</i>
Land Surface White-sky Albedo	VIIRS Gridded Albedo IP	<i>Input for Albedo EDR</i>
Land Surface Black-sky Albedo at MSZA	VIIRS Gridded Albedo IP	<i>Extra Information</i>
Land Surface Broadband Albedo (DPSA)	VIIRS Albedo EDR	<i>Albedo EDR Requirement</i>
Land Surface Broadband Albedo (BPSA)	VIIRS Albedo EDR	<i>Albedo EDR Requirement</i>
Updated Historical BRDF Archetype	Historical BRDF Archetype	<i>Input for Gridded Albedo IP</i>

3.2.1 Input VIIRS Data

To compute the Gridded Surface Albedo IP and Surface Albedo EDR, individual information is needed from different VIIRS products. Table 3.3 shows all the information needed for the computation.

Table 3.3. VIIRS input data for computing Surface Albedo EDR and Surface Albedo IP.

Input VIIRS Data	Information Needed	Target Product
750-m Earth View SDR	geolocation , TOA reflectance	<i>Albedo EDR</i>
Surface Reflectance IP	Land Quality Flags, TOC reflectance	<i>Albedo EDR</i>
Aerosol Optical Thickness IP	AOT values	<i>Albedo EDR</i>
Aerosol Model Information IP	aerosol model type	<i>Albedo EDR</i>
Snow Cover EDR	snow cover flag	<i>Albedo EDR</i>
Gridded Albedo IP	BRDF information	<i>Albedo EDR</i>
Gridded Daily Surface Reflectance IP	surface reflectance	Albedo IP
Historical BRDF Archetype	historical BRDF	Albedo IP

3.2.2. Input Non-VIIRS Data

A historical BRDF data set is required in case there are not enough valid surface reflectance observations available for estimating the BRDF. This data set will be updated with newly retrieved BRDF after each run. MODIS BRDF data will be used to build up such a data set at beginning.

There are two National Centers for Environmental Prediction (NCEP) data sets needed in the VIIRS Albedo algorithm: the total column ozone mass and the precipitable water. These data sets are used to correct corresponding atmospheric absorptions from TOA reflectance that are the input for computing bright pixel surface albedo.

3.2.3. Lookup Tables

In addition to the above gridded and swath level input data, there are four lookup tables (LUTs) that may be considered as input data:

- 1) skylight diffusion coefficients LUT;
- 2) BPSA regression weight coefficients LUT;
- 3) DPSA Narrowband-to-Broadband Coefficients LUT;
- 4) Kernel black-sky and white-sky albedo LUT.

Details of these input data are described in Section 3.3.

3.2.4 Output

Both the DPSA and BPSA albedo values are provided through the albedo EDR. Users are also provided with a flag for each pixel indicating if the DPSA or BPSA is preferred. The flag is passed from the AOT IP.

The Gridded Albedo IP consists of the BRDF information inverted from the gridded daily surface reflectance IP data, NBAR, mean solar zenith angle of the reflectance data, and white-sky and black-sky spectral albedo. The BRDF information contains index numbers indicating what kernels are selected for building up a BRDF kernel combination model, and a set of model parameters. The NBAR values (as well as the mean solar zenith angle) are required by the gridding module for data composition. The white-sky albedo and black-sky albedo are the input for spectral albedo computation in the albedo EDR processing. It is worth to note that the black-sky albedo produced here cannot be used directly for the spectral albedo interpolation processing, because solar zenith angle at swath level is different to the MSZA in the gridded albedo IP. Details about how to generate the Gridded Surface Albedo IP are described through sections 3.3.2.1.1 to 3.3.2.1.6.

3.3. THEORETICAL DESCRIPTION OF ALGORITHM

3.3.1. Physics of the Problem

Albedo is related to surface reflectance through the integration of the BRDF, which describes the intrinsic anisotropic character of the surface. Specification of the BRDF provides surface reflectance explicitly in terms of its spectral, directional, spatial and temporal characteristics. Both BRDF and albedo are determined by surface structure and optical properties. Typical structural phenomena for vegetation include: the gap distribution between vegetated areas, vegetation height and style, leaf angle distribution function, and the hotspot—a local reflectance maximum caused by the absence of shadows in the retrosolar position. Over ocean, the wind speed roughens the water surface. Over snow, the snow grain size and the contribution of soot have a strong impact on the reflectance field.

The importance of including BRDF features in the interpretation of satellite-derived data has been emphasized by many researchers (Pinty and Verstraete, 1991; Liang and Strahler, 1993; Nilson and Kuusk, 1989; Ross and Marshak, 1989; Jupp and Strahler, 1991; Andrieu *et al.*, 1997; Vogt, 1997). Neglecting BRDF effects can result in serious deviations when calculating the spectral and broadband albedo (Han, 1996; Qi *et al.*, 1995; Schaaf and Strahler, 1993; Lee and Kaufman, 1986).

3.3.2. Mathematical Description of Algorithm

The fundamental definitions of parameters related to Surface Albedo retrievals are summarized in Table 3.4. In this document, The Surface Albedo satellite retrieval algorithm yields outputs very close to that provided in Lucht *et al.* (2000).

Table 3.4 Parameter definitions relevant to the Surface Albedo EDR.

Symbol	Definition/Comments	Units
θ	Solar zenith angle	rad
ϑ	View zenith angle	rad
ϕ	Relative azimuth angle	rad
λ	Wavelength	μm
Λ	Waveband Λ of width $\Delta\lambda$	None
$\tau(\lambda)$	Atmospheric optical depth	None
$S(\theta, \tau(\lambda))$	Fraction of diffuse skylight, assumed isotropic	None
$D(\theta, \lambda, \tau(\lambda))$	Bottom of atmosphere downwelling radiative flux	$\text{Wm}^{-2}\mu\text{m}^{-1}$
$U(\theta, \lambda, \tau(\lambda))$	Bottom of atmosphere upwelling radiative flux	$\text{Wm}^{-2}\mu\text{m}^{-1}$
D_{BB}	Broadband bottom of atmosphere downwelling flux	Wm^{-2}
U_{BB}	Broadband bottom of atmosphere upwelling flux	Wm^{-2}
$\rho(\theta, \vartheta, \phi, \Lambda)$	Observed surface reflectance (atmospherically corrected)	None
$\rho_{\text{TOA}}(\theta, \vartheta, \phi, \Lambda)$	Observed top of atmosphere reflectance	None
$R(\theta, \vartheta, \phi, \Lambda)$	Bidirectional reflectance distribution function (BRDF)	None
$K_k(\theta, \vartheta, \phi)$	BRDF model kernel k	None

$h_k(\theta)$	Integral of BRDF model kernel k over ϑ and ϕ	None
H_k	Integral of $h_k(\theta)$ over θ	None
$f_k(\Lambda)$	BRDF kernel model parameter k in waveband Λ	None
$a_{bs}(\theta, \lambda)$	Spectral black-sky albedo	None
$a_{ws}(\lambda)$	Spectral white-sky albedo	None
$a(\theta, \lambda)$	Spectral albedo	None
$A(\theta)$	Broadband albedo	None

Consider a satellite-based sensor observing the surface at a view zenith angle ϑ . The sun illuminates this surface at a solar zenith angle θ , and ϕ is the relative azimuth angle between the sun and the sensor. A number of important quantities relating to albedo are functions of spectral wavelength, which will be designated by λ . The sensor observing the surface will integrate over λ to deliver measurements in a spectral waveband Λ .

Intervening between the surface and the sensor is an atmosphere, which has an optical depth $\tau(\lambda)$. In the bands most relevant to albedo retrieval, the majority of this optical depth arises from Rayleigh and aerosol scattering, and the effects of these processes become larger with decreasing λ . Where there is no atmosphere present, the only significant radiation propagating from the sun to the surface and back to the sensor is in the form of direct beams. The more aerosols are present in the atmosphere, or the shorter the wavelength λ , the greater the fraction of direct and reflected solar radiation that exists as diffuse, scattered light. The fraction of diffuse skylight, assumed here to be isotropic, is represented by $S(\theta, \tau(\lambda))$. At the bottom of the atmosphere, combined diffuse and direct downwelling radiative flux is $D(\theta, \lambda, \tau(\lambda))$, and the upwelling flux is $U(\theta, \lambda, \tau(\lambda))$.

The surface reflects some portion of the incident solar radiation, a process that can be characterized by the surface reflectance, which is a function of the solar and viewing geometry combined with the properties of the surface itself. We define the atmospherically corrected observed reflectance in a given waveband as $\rho(\theta, \vartheta, \phi, \Lambda)$. This quantity exists within the VIIRS system as the Gridded Daily Surface Reflectance IP. It is a directional reflectance corresponding to one particular combination of solar and viewing geometry. The manner in which geometry alone affects $\rho(\theta, \vartheta, \phi, \Lambda)$ in a given band is characterized by the surface bi-directional reflectance distribution function (BRDF), $R(\theta, \vartheta, \phi, \Lambda)$.

Spectral albedo is defined as the ratio of spectral upwelling radiative flux $U(\theta, \lambda, \tau(\lambda))$ to spectral downwelling radiative flux $D(\theta, \lambda, \tau(\lambda))$ at the surface, and therefore involves integration over the hemisphere represented by the range of possible values for ϑ and ϕ . Broadband albedo, the primary output of the Surface Albedo EDR, is defined as the ratio of broadband fluxes $U_{BB}(\theta, \tau(\lambda))$ and $D_{BB}(\theta, \tau(\lambda))$. Spectral albedo $a(\theta, \Lambda)$ can be considered a combination of two other quantities: the spectral black-sky albedo $a_{bs}(\theta, \Lambda)$ and the spectral white-sky albedo $a_{ws}(\Lambda)$. The spectral black-sky albedo is defined as the spectral albedo in the absence of a diffuse component, and the spectral white-sky albedo is defined as the spectral albedo in the absence of a direct component, assuming an isotropic diffuse surface. Therefore, for a given band Λ , Black-sky albedo is therefore a function of the solar zenith

angle θ , while white-sky albedo is not. The degree to which each of $a_{bs}(\theta, \Lambda)$ and $a_{ws}(\Lambda)$ contribute to $a(\theta, \Lambda)$ is determined by the fraction of diffuse skylight $S(\theta, \tau(\lambda))$. Conversion from the observed spectral albedo $a(\theta, \Lambda)$ to the observed broadband albedo $A(\theta)$ involves approximating an integration over λ using measurements from several spectral bands Λ .

3.3.2.1 Dark Pixel Sub-Algorithm (DPSA)

The VIIRS DPSA algorithm is derived from the MODIS albedo algorithm (Wanner *et al.*, 1995; 1997; Lucht *et al.*, 2000; Schaaf *et al.*, 2001), with a few modifications. In principle, it consists of four steps: 1) surface BRDF is estimated using a set of accumulated surface reflectance data and semi-empirical BRDF models; 2) black-sky albedo $a_{bs}(\theta, \Lambda)$ and white-sky albedo $a_{ws}(\Lambda)$ are computed using the estimated BRDF; 3) the spectral surface albedo is then derived from the black-sky and white-sky albedo using the interpolation factor $S(\theta, \tau(\lambda))$, as shown in Lewis and Barnsley (1994):

$$a(\theta, \Lambda) = [1 - S(\theta, \tau(\Lambda))]a_{bs}(\theta, \Lambda) + S(\theta, \tau(\Lambda))a_{ws}(\Lambda) \quad (3.1)$$

A tabulated relationship between the aerosol optical thickness and the fraction of diffuse skylight $S(\theta, \tau(\lambda))$ can be established using radiative transfer simulation program such as 6S. In this algorithm, a scripting program is created that runs the 6S simulation automatically with loops over the solar zenith angles, the aerosol optical thickness (AOT), the aerosol models and the VIIRS bands. The solar zenith angle is set from 0 to 85 degrees with increment of 1 degree, and the AOT is set from 0.0 to 2.0 with increment of 0.02. There are eight land surface aerosol models defined in the VIIRS Aerosol Model Information Unit [AL60822-VIR-007]: 6S-Maritime, 6S-Continental, Dust, Smoke-High Absorption, Smoke-Low Absorption, Urban-Polluted, Urban-Clean and Oceanic.

Finally, all the narrowband spectral albedos are converted into a short-wave band (0.4 to 4.0 μm) albedo using a set of linear regression coefficients. Appendix A.1 gives detail descriptions of this narrowband-to-broadband conversion coefficients set.

In this algorithm, the first two steps are processed offline, that results in the Gridded Daily Albedo IP. At real time, the gridded albedo IP, as well as other VIIRS data, are ingested to generate the swath level Surface Albedo EDR. Following subsections describe how the BRDF is estimated from the accumulated surface reflectance observations.

3.3.2.1.1 BRDF Kernel Model and Kernel Black- and White-sky Albedo

The linear kernel-based BRDF model was firstly introduced by Roujean *et al.* (1992), and was later further developed and widely applied (e.g. Wanner *et al.*, 1995; Gao *et al.*, 2000; Lucht *et al.*, 2000; Lucht and Roujean, 2000; Leroy, 2001; Pokrovsky and Roujean, 2002; Schaaf *et al.*, 2002). The model is written in the form

$$R(\theta, \vartheta, \phi, \Lambda) = \sum_k f_k(\Lambda) K_k(\theta, \vartheta, \phi), \quad (3.2)$$

where $R(\theta, \vartheta, \phi, \Lambda)$ is the BRDF at waveband Λ , $K_k(\theta, \vartheta, \phi)$ the BRDF model kernel k , and $f_k(\Lambda)$ the kernel model parameter k at waveband Λ . The kernel function K describes surface scattering features, and is dependent on the sun-satellite-view geometry: the solar zenith angle θ , the satellite viewing angle ϑ , and sun-satellite relative azimuth angle ϕ . If we define a directional-hemispherical integral of the BRDF model kernels with respect to the viewing zenith and relative azimuth as *kernel black-sky albedo*, it is written as

$$h_k(\theta) = \frac{1}{\pi} \int_{\phi=0}^{2\pi} \int_{\vartheta=0}^{\pi/2} K_k(\theta, \vartheta, \phi) \sin(\vartheta) \cos(\vartheta) d\vartheta d\phi \quad (3.3)$$

Similarly, *kernel white-sky albedo* can be defined as a bi-hemispherical integral of the BRDF model kernels with respect to the solar zenith as kernel white-sky albedo. It is

$$H_k = 2 \int_{\theta=0}^{\pi/2} h_k(\theta) \sin(\theta) \cos(\theta) d\theta, \quad (3.4)$$

where k indicates the kernel function K_k . Obviously, the spectral black-sky albedo is a weighted sum of the kernel black-sky albedo, as

$$a_{bs}(\theta, \Lambda) = \sum_k f_k(\Lambda) h_k(\theta) \quad (3.5)$$

and the spectral white-sky albedo is the weighted sum of the kernel white-sky albedo

$$a_{ws}(\Lambda) = \sum_k f_k(\Lambda) H_k. \quad (3.6)$$

An important property of the BRDF kernel model is that the kernel functions are geometric dependent only. Therefore, the kernel black-sky albedo $h_k(\theta)$ and white-sky albedo H_k can be pre-computed and stored as lookup tables. Retrieval of the spectral black-sky and white-

sky albedo, at run time, is targeted to obtain the kernel model parameters $f_k(\Lambda)$ for each kernel at each waveband. This is a typical inversion process that will be discussed shortly.

3.3.2.1.2 Kernels

The most common used BRDF kernel model is a three-term linear model, written as

$$R(\theta, \vartheta, \phi, \Lambda) = f_{iso}(\Lambda) + f_{vol}(\Lambda)K_{vol}(\theta, \vartheta, \phi) + f_{geo}(\Lambda)K_{geo}(\theta, \vartheta, \phi). \quad (3.7)$$

In this model, the three kernels describe three fundamental types of scattering: 1) isotropic scattering (represented by subscript *iso*), which is a constant kernel; 2) volumetric scattering of the classical radiative transfer type (represented by subscript *vol*); and 3) geometric-optical scattering (represented by subscript *geo*) which represents shadow-casting and/or mutual shadowing (Lucht and Roujean, 2000).

3.3.2.1.2.1 Volumetric Scattering Kernels

There are two volumetric scattering kernels applied for the VIIRS algorithm. The first one is the Ross-thick kernel. It is a single scattering approximation to radiative transfer theory in plant canopies by Ross (1981) assuming equality of leaf transmission and reflectance, uniform leaf angle distribution and a Lambertian background (Roujean *et al.*, 1992). Table 3.5 listed the above kernels.

Table 3.5 Volumetric scattering kernels used in VIIRS land surface albedo algorithm

Kernel	Formula
Ross-thick	$K_{Ross-thick} = \frac{(\pi/2 - \xi) \cos \xi + \sin \xi}{\cos \theta + \cos \vartheta} - \frac{\pi}{4}$
Ross-thin	$K_{Ross-thin} = \frac{(\pi/2 - \xi) \cos \xi + \sin \xi}{\cos \theta \cos \vartheta} - \frac{\pi}{2}$
Note: $\cos \xi = \cos \theta \cos \vartheta + \sin \theta \sin \vartheta \cos \phi$	

The Ross-thick kernel primarily applies to the case of thick canopy of scattering. For thin canopy scattering, the Ross-thin kernel may apply.

3.3.2.1.2.2 Geometric Scattering Kernels

A number of geometric-optical scattering kernel functions have been derived; among them, the Li series kernels (Li and Strahler, 1986, 1992; Strahler, 1994) are widely applied. This algorithm also employs the Li series kernels for the BRDF model generation. In addition, Roujean (1992) kernel is used. These kernels represent most of land surface canopies

scattering features and therefore are appropriate for the VIIRS global land surface albedo retrieval. The geometric-optical scattering kernels are listed in Table 3.6.

Table 3.6 Geometric-optical scattering kernels used in VIIRS land surface albedo algorithm

Kernel	Formula
non-reciprocal Li-Sparse	$K_{Li-Sparse}^{non-reciprocal} = O(\theta, \vartheta, \phi) - \sec \theta' - \sec \vartheta' + \frac{1}{2}(1 + \cos \xi') \sec \vartheta'$
reciprocal Li-Sparse	$K_{Li-Sparse}^{reciprocal} = O(\theta, \vartheta, \phi) - \sec \theta' - \sec \vartheta' + \frac{1}{2}(1 + \cos \xi') \sec \theta' \sec \vartheta'$
non-reciprocal Li-Dense	$K_{Li-Dense}^{non-reciprocal} = \frac{(1 + \cos \xi') \sec \vartheta'}{\sec \theta' + \sec \vartheta' - O(\theta', \vartheta', \phi)} - 2$
reciprocal Li-Dense	$K_{Li-Dense}^{reciprocal} = \frac{(1 + \cos \xi') \sec \theta' \sec \vartheta'}{\sec \theta' + \sec \vartheta' - O(\theta', \vartheta', \phi)} - 2$
non-reciprocal Li-Transit	$K_{Li-Transit} = \begin{cases} K_{Li-Sparse} & \text{if } B(\theta, \vartheta, \phi) \leq 2 \\ K_{Li-Dense} & \text{if } B(\theta, \vartheta, \phi) > 2 \end{cases}$
Roujean	$K_{Roujean} = \frac{1}{2\pi} [(\pi - \phi) \cos \phi + \sin \phi] \tan \theta \tan \vartheta - \frac{1}{\pi} (\tan \theta + \tan \vartheta + D)$
<p>Note: in the above kernels, these functions and parameters apply</p> $O(\theta, \vartheta, \phi) = \frac{1}{\pi} (t - \sin t \cos t) (\sec \theta' + \sec \vartheta'), \quad \cos t = \frac{h}{b} \frac{\sqrt{D^2 + (\tan \theta' \tan \vartheta' \sin \phi)^2}}{\sec \theta' + \sec \vartheta'}$ $D = \sqrt{\tan^2 \theta' + \tan^2 \vartheta' - 2 \tan \theta' \tan \vartheta' \cos \phi}, \quad \cos \xi' = \cos \theta' \cos \vartheta' + \sin \theta' \sin \vartheta' \cos \phi$ $\theta' = \tan^{-1} \left(\frac{b}{r} \tan \theta \right), \quad \vartheta' = \tan^{-1} \left(\frac{b}{r} \tan \vartheta \right), \quad B(\theta, \vartheta, \phi) = \sec \theta' + \sec \vartheta' - O(\theta, \vartheta, \phi)$ <p>where h describes the crown model central height above the ground, r and b describe the vertical and horizontal dimensions of the crown spheroid.</p>	

Using these kernels, 12 BRDF model combinations can be obtained based on Equation (3.7). Table 3.7 lists these model combinations.

Table 3.7 Kernel model combinations

number	Kernel model
0	Ross-thick and non-reciprocal Li-Sparse
1	Ross-thin and non-reciprocal Li-Sparse
2	Ross-thick and reciprocal Li-Sparse
3	Ross-thin and reciprocal Li-Sparse
4	Ross-thick and non-reciprocal Li-Dense
5	Ross-thin and non-reciprocal Li-Dense
6	Ross-thick and reciprocal Li-Dense
7	Ross-thin and reciprocal Li-Dense
8	Ross-thick and Li-Transit

9	Ross-thin and Li-Transit
10	Ross-thick and Roujean
11	Ross-thin and Roujean

It is worth noting that MODIS Surface Albedo algorithm uses a fixed model combination, while VIIRS decided to use all the above possible model combinations. Although research with MODIS data shows that Ross-thick and reciprocal Li-Sparse is a dominant kernel model combination over the globe, other model combinations may better represent BRDF features in some area and in some times. Selection for a best model combination is an expensive computing process because of matrix computation for each model combination. It is, however, pretty straightforward once a selection criterion is determined, as will be described shortly in section 3.3.2.1.4. Computing expenses are less significant since new generation computers are more powerful and less expensive, so computational expense is a less important consideration. Given the worst case, if the computation time should be a problem, the selectable model combination algorithm can easily degenerate to a fixed model combination algorithm.

3.3.2.1.3 Full Inversion Process

It is very clear that determination of the kernel model parameters using Equation. (3.7) is the core part of black-sky and white-sky albedo computation. For VIIRS, this is set up as a least-squares fit problem.

Assuming that there are n surface reflectance observations in the 1-km grid cell, the BRDF kernel model of Equation.(3.7) can be rewritten in matrix expression as

$$R = K \cdot F \tag{3.8}$$

where R is a column vector of the reflectance measurements \square

$$R = \begin{pmatrix} \rho(\theta_1, \vartheta_1, \phi_1) \\ \rho(\theta_2, \vartheta_2, \phi_2) \\ \dots \\ \dots \\ \rho(\theta_n, \vartheta_n, \phi_n) \end{pmatrix}, \tag{3.9}$$

K is a matrix of the kernels

$$K = \begin{pmatrix} 1 & K_{vol}(\theta_1, \mathcal{G}_1, \phi_1) & K_{geo}(\theta_1, \mathcal{G}_1, \phi_1) \\ 1 & K_{vol}(\theta_2, \mathcal{G}_2, \phi_2) & K_{geo}(\theta_2, \mathcal{G}_2, \phi_2) \\ \dots & \dots & \dots \\ \dots & \dots & \dots \\ 1 & K_{vol}(\theta_n, \mathcal{G}_n, \phi_n) & K_{geo}(\theta_n, \mathcal{G}_n, \phi_n) \end{pmatrix}, \quad (3.10)$$

and F is a column vector of the model parameters

$$F = \begin{pmatrix} f_{iso} \\ f_{vol} \\ f_{geo} \end{pmatrix} \quad (3.11)$$

Solving (3.8) is a typical linear algebraic problem: determining three parameters from n linear equations. There are several numerical algorithms available to solve such a problem. In VIIRS, we adapted the Singular Value Decomposition (SVD) algorithm for a solution. The SVD method is not only a powerful technique for solving most linear least squares problems, it is also a good choice of technique for dealing with sets of equations or matrices that are either singular or else numerically very close to singular. In our case, 16-day gridded surface reflectance data collection is used to build the knowing equations. Because of the NPOESS satellite orbit and viewing geometry, the qualified surface reflectance data (e.g. cloud free) may be limited both in number and in geometric distribution. The SVD algorithm is therefore a good choice. In addition, the SVD method makes covariance analysis available with just a little extra computation, which will be used in model selection shortly.

So, using SVD method, the kernel function matrix K is decomposed, as

$$K = U \cdot W \cdot V^T \quad (3.12)$$

where U and V are orthogonal matrices, i.e.. $U^T U = V^T V = I$, and W is a diagonal matrix. The model parameter vector F is solved by

$$F = V \cdot W^{-1} \cdot U^T \cdot R \quad (3.13)$$

It is a common practice that weighting parameters are added in the least-square fit processing. In SVD method, this is done by replacing R and K matrices, in Equation (3.8), using weighted R and K matrices. The weight parameters are determined based on quality control flags that are associated with the individual surface reflectance observations.

3.3.2.1.4 Model Selection

As presented before, there are twelve kernel model combinations from our two volumetric scattering kernel functions and six geometric scattering kernel functions (see Table 3.6).

Selection must be made for the one best presenting the real BRDF. There are three possible criteria to make the selection.

3.3.2.1.4.1 Select by RMSE

This criterion is based on absolute errors between the observations and model derivation (Strahler *et al.*, 1996). Consider that the residual matrix of the above inversion process being defined as

$$E = R - K \cdot F \quad (3.14)$$

i.e., the difference between the real observations and the derived measurements using the solved model parameters. The root mean square error (RMSE) is therefore determined through the following equation

$$RMSE = \frac{\|E\|}{\sqrt{v}} \quad \text{where} \quad \|E\| = \sqrt{\sum_k E_k E_k} \quad (3.15)$$

with the degree of freedom $v=n-3$. The total absolute inversion error of all bands for a given kernel model combination is given by

$$\delta = \sqrt{\frac{1}{N_b} \sum_b RMSE_b^2} \quad (3.16)$$

where the index b represents all the moderate resolution VIIRS bands and N_b is the number of bands (N_b is 9 in our case). The RMSE criterion is to select the kernel model combinations that has minimum δ .

3.3.2.1.4.2 Select by Model Parameter Variance

Instead of comparing the model derived values and the observations, we can also compare the variance of the estimated parameters F . The SVD algorithm provides a variance estimation of the inversed parameters (Press *et al.*, 1986), under assumption that noise covariance matrix of the measurements is unity. It is given by

$$\sigma^2(f_j) = \sum_i \left(\frac{V_{ji}}{w_i} \right)^2, \quad (3.17)$$

where j and i take values of 1, 2 and 3 for *iso*, *vol*, and *geo* terms, respectively. The corresponding covariance matrix of the parameters vector F can be written as

$$F_{\text{cov}} = VW^{-1}(W^{-1})^T V^T \quad (3.18)$$

The variance of all the parameters of a model combination is therefore

$$\sigma^2 = \sum_j \sigma^2(f_j) \quad (3.19)$$

The criterion of model parameters variance is to select the kernel model so that the overall variance σ is minimized.

It is very interesting to see that, the variance estimated by (3.18) is only dependent to the observation geometry, and is independent to the reflectance measurement itself. In other words, the variance is wavelength independent. This is because variation of the kernels determines the variance of model parameters, and the kernels are only observation geometry dependent. This feature significantly reduces the computation time of the comparison, compared to the RMSE criterion.

Note that the above description is under the assumption that the observation uncertainty has a Gaussian distribution, and its standard deviation is the same for all the bands.

3.3.2.1.4.3 Select by White-Sky Albedo Variance

The least-variance method described above can also be applied to the white-sky albedo comparison, as was introduced by Gao *et al.* (2001). Since kernels yielding the least variance of white-sky albedo will have the least sensitivity to noise from measurements, using variance of white-sky albedo is more reliable.

For doing so we first need to build up a vector that contains all the kernel white-sky albedos of a kernel combination model. The spectral white-sky albedo is defined as in (3.6). Its vector form is

$$a_{\text{ws}} = H \cdot F \quad (3.20)$$

where F is the model parameters vector as defined in (3.11), and H is the kernel white-sky albedo vector

$$H = (H_{\text{iso}} \quad H_{\text{vol}} \quad H_{\text{geo}}) \quad (3.21)$$

Variance of the spectral white-sky albedo can be calculated by

$$\sigma_{a_{\text{ws}}}^2 = H \cdot F_{\text{cov}} \cdot H^T \quad (3.22)$$

where F_{cov} , the covariance matrix of F , is estimated in the SVD process in (3.18).

The criterion is therefore to select such a model combination that the sum of the a_{ws} variance is minimized. Since F_{cov} and H are all band independent, this criterion is also band-independent.

Like the criterion of model parameters variance, the above description is under assumption that the observation uncertainty has a Gaussian distribution, and its standard deviation is the same for all the bands.

3.3.2.1.5 Physics Constraint

Theoretically, as long as the number of observations is larger than or equals to the number of model parameters, three in our case, the SVD algorithm always gives result. However, care must be taken to ensure a qualified inversion results.

First, each inversed model parameter should be positive since the kernel function describes positive hemisphere bi-directional reflectance and the scattering kernels should be semi-orthogonal (Lucht *et al.*, 2000). The above inversion algorithm, however, will possibly produce negative model parameter values. This is because the SVD algorithm gives solution even when the input data are singular values, or very close to singular values. This is usually far from the “correct” solution. Also, bad inversion results may occur if the input data are poorly sampled, e.g. there is not enough data and/or the data distribution in geometry is not good. In such circumstances, the next valid value for this model parameter is zero, and the remaining kernel parameters should be re-derived (Lewis, 1995; Lucht *et al.*, 2000). In other words, the three-term kernel model may turn to be a two-term model.

It is worth to note that there is debate among the BRDF and albedo research community if the negative model parameters should be constrained. (Feng Gao, personal communication, 2004). Positive reflectance should be the constraint, rather than the coefficients of the kernel (Shunlin Liang, personal communication, 2004). This is true since kernels may allow negative values in their statistical interpretation of the two-stream approximation. In practice, however, implementation for testing positive reflectance over all the solar-view geometry distribution is redundant.

The next concern is that, although the model parameters are all positive values but the number of observations is too small, the inverted result may not be reliable. In MODIS practice, the minimum number of observations for full inversion process is seven. We also use this number as the minimum threshold since VIIRS is very similar to MODIS in orbit mechanics and scanning features. It is also worth to point out that solar-view geometric distribution of observations is more important to the observation numbers for a better inversion. The threshold of observation numbers does not count the geometry distribution, but is more implementable.

Finally, if the RMSE, model parameter variance, or white-sky albedo variance of the selected kernel model is larger than a maximum threshold value, the inverted result is

considered as bad. Large RMSE or variance may occur when the observation is too noisy or the geometric distribution is too bad. In such cases, the full inversion process may fail.

3.3.2.1.6 Magnitude Inversion Process

Magnitude inversion is a backup process that is performed in cases where the full inversion process failed or the number of observations is less than the minimum threshold. The magnitude inversion process relies on historical BRDF kernel model parameters, the archetypal shapes. In principle, the archetypal shape is accepted as a retrieved BRDF but its magnitude is adjusted using the observations.

Assume that there are n observations in a gridded 1-km cell, and the historical model parameters are f_i^{his} with $i=1,2$ or 3 for *iso*, *vol* and *geo* terms of the kernels, respectively, surface reflectance retrieved using the historical kernel parameters can be written as

$$\rho_l^{his} = \sum_i f_i^{his} K_i(\theta_l, \vartheta_l, \phi_l) \quad (3.23)$$

where l indicates the l -th observation. We define two parameters

$$sum_1 = \sum_{l=1}^n \rho_l^{obs} \cdot \rho_l^{his} \cdot w_l, \quad (3.24)$$

and

$$sum_2 = \sum_{l=1}^n \rho_l^{his} \cdot \rho_l^{his} \cdot w_l, \quad (3.25)$$

where ρ_l^{obs} is the l -th observed surface reflectance, and w_l the weight of the measurement. The kernel model parameters can be modified, as

$$f_i^{new} = \frac{sum_1}{sum_2} \cdot f_i^{his} \quad (3.26)$$

This magnitude inversion process is inherited from MODIS surface albedo retrieval algorithm.

3.3.2.1.7 BRDF Layers

In the use of the BRDF archetypal shape one must keep in mind that surface reflectance properties over a certain geographic location may have significant differences between different vegetation growth phases during the year. Ideally, the historical BRDF shape data set gives detailed information about seasonal changes of the vegetation growth as well. In practice, however, only limited seasonal change information may be available due to observation limitations and computation time.

In this algorithm, we decide to use a three-layer BRDF shape structure for the BRDF inversion: the vegetated surface BRDF, the dormant surface BRDF and the snow cover surface BRDF. Before running inversion process, the 16-day surface reflectance data is classified into snow and non-snow data clusters using the snow cover flag read from the Snow and Ice EDR. The non-snow data is further flagged as vegetated or dormant surface data. This is done by computing mean Normalized Difference Vegetation Index (NDVI) over the non-snow cover data and comparing the mean NDVI to a predetermined NDVI threshold value (0.15, in our case). All the non-snow reflectance data are considered as vegetated surface data if the mean NDVI is larger than the threshold value, or otherwise they are the dormant surface data.

Corresponding layers of the BRDF archetypal data are updated after the inversion process if a full inversion BRDF data, with good quality, is obtained. There is a time stamp for each BRDF layer, each pixel, indicating when the latest update of the BRDF information occurred. This leaves flexibility that user decide whether the historical BRDF should be used if the time stamp is really an old one.

3.3.2.1.8 Nadir BRDF-Adjusted Reflectance

Once the inversion process is completed (either full inversion or magnitude inversion), computation of NBAR is straight forward using the inverted BRDF. Mean solar zenith angle of the observations is used for this computation. The NBAR product is not a requirement of Surface Albedo IP, but is useful in computation of surface type classification. Readers are directed to the VIIRS Surface Type EDR ATBD [Y2402] for more details.

3.3.2.1.9 Narrowband to Broadband Conversion

Once the surface BRDF is determined as Equation (3.2), the spectral dark pixel surface albedo can be estimated through Equations (3.1), (3.5) and (3.6). The broadband shortwave albedo, $A(\lambda)$, covering the radiative spectrum from 0.4 to 4.0 μm can be estimated using a linear regression equation developed by Liang *et al.* (2004):

$$\begin{aligned} A(\theta) = & 0.0948a_{M1}(\theta) + 0.2294a_{M2}(\theta) - 0.2323a_{M3}(\theta) \\ & + 0.2785a_{M4}(\theta) + 0.1580a_{M5}(\theta) + 0.2775a_{M7}(\theta) \\ & + 0.0945a_{M8}(\theta) + 0.0939a_{M10}(\theta) + 0.0239a_{M11}(\theta) \end{aligned} \quad (3.27)$$

where $a_{Mi}(\theta)$ is the spectral albedo at the narrowband Mi ($i=1,2,3,4,5,7,8,10,11$). Appendix A.1 gives the details about this conversion formula.

3.3.2.1.10 Bright Pixel Sub-Algorithm (BPSA): Regression Approach

The use of the DPSA for albedo retrievals hinges upon one key assumption: the availability of accurate aerosol optical thickness estimation. If this assumption does not hold, the propagation of the resulting errors through the retrieval of surface reflectance, diffuse

skylight fraction, atmospheric state, and the various subsets of albedo itself will endanger the ability of the VIIRS system to meet the specifications for the Surface Albedo EDR. For bright surfaces, such as snow and desert, where the broadband albedo significantly exceeds 0.3, the VIIRS system specification for aerosol optical thickness quality suggests absolute errors in surface reflectance that are too high to allow the meeting of the Surface Albedo EDR requirements. This does not even take into account other factors, such as the computation of diffuse skylight fraction. Consequently, in order to reduce risk for retrieval of Surface Albedo over bright surfaces, we have implemented a regression solution that works directly from current measurements of TOA reflectance.

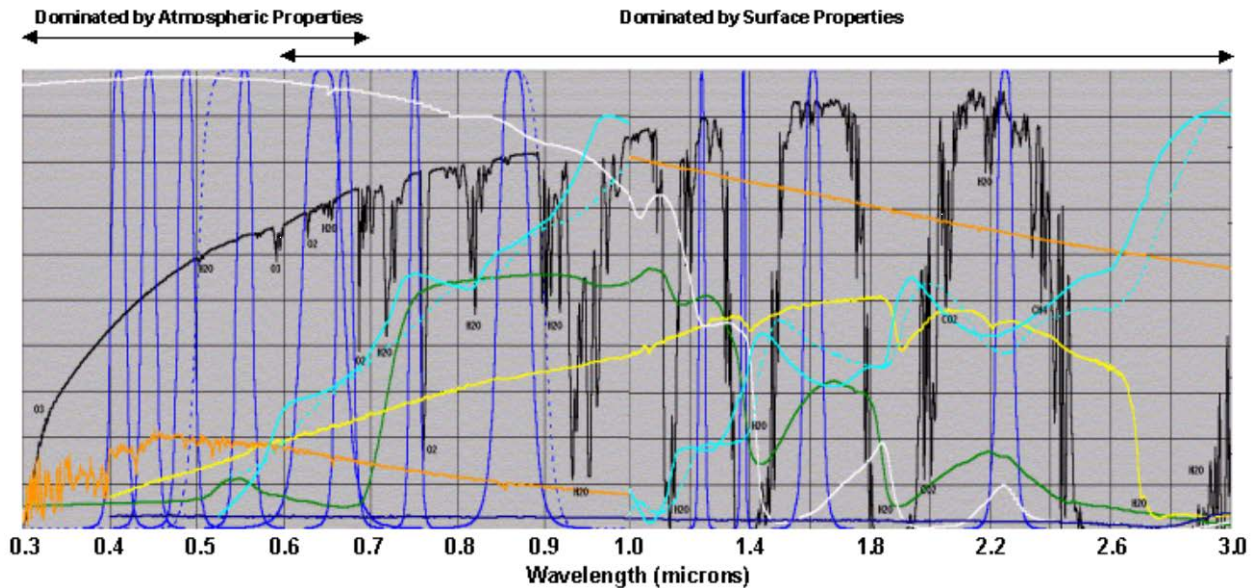


Figure 3.3 Spectral decoupling of atmospheric and surface properties for derivation of broadband albedo.

A number of earlier studies, such as Chen and Ohring (1984), Pinker (1985), Koepke and Kriebel (1987), and Li and Garand (1994), have linearly related TOA spectral albedo to surface broadband albedo. In the past, however, such methods have been limited by the lack of spectral information at the global scale. Until the launch of the Terra spacecraft in late 1999, the only consistent source of visible, near infrared (NIR), and short wave infrared (SWIR) information at high spectral resolution was the Landsat Thematic Mapper (TM). AVHRR, throughout most of its history, only contained red and Near Infrared (NIR) information. Relating TOA reflectance to surface albedo requires the addition of shorter wavelengths for characterization of the atmosphere and longer wavelengths for subtle distinctions between snow, soil and vegetation, as shown in Figure 3.3, Liang *et al.* (1999) demonstrated through simulations that the kind of spectral information available on a global scale from MODIS would lend itself to a truly robust application of this technique. A neural network, which is essentially a form of nonlinear regression, was employed toward that end. Additional testing has proven this approach to be effective with real MODIS data, and linear regression has been found sufficient to preclude the need for a neural network (Liang, 2003).

The VIIRS algorithm in this revision therefore consists of a linear regression equation using the TOA reflectance values in several bands as input, as well as the angles describing the solar and viewing geometry. These latter inputs provide an accounting for variations in the BRDF. The following paragraphs give a brief description of the BPSA linear regression equation. More details about how the equation is derived and how the coefficients are computed can be found in Appendix A.2.

In this algorithm, the BPSA is expressed by

$$A(\theta) = f(\rho_1(\theta, \vartheta, \phi), \rho_2(\theta, \vartheta, \phi), \dots, \rho_n(\theta, \vartheta, \phi)) \tag{3.28}$$

where f represents a linear regression equation, and n indicates 9 VIIRS bands for M1-M5, M7-M8, and M10-11. ρ is the TOA reflectance ρ^{TOA} corrected for total column water vapor and ozone absorptions, that is

$$\rho_n(\theta, \vartheta, \phi) = \rho_n^{TOA}(\theta, \vartheta, \phi) / (T_w T_{oz}) \tag{3.29}$$

T_w and T_{oz} are the transmittances of the water vapor and the ozone in both the solar incident and viewing paths.

Simulation study in Appendix A.2 shows that the regression coefficients should vary with satellite solar-view geometry, and coefficient set should be given for each gridded angular bin. Table 3.8 gives the angular grid of solar zenith, view-zenith and solar-view relative azimuth.

Table 3.8. Solar-view geometry grid for BPSA coefficients.

Angle	Grid
Solar Zenith	0, 5, 10, 15, 20, 25, 30, 35, 40, 45, 50, 55, 60, 65, 70, 75, 80, 85
View Zenith	0, 5, 10, 15, 20, 25, 30, 35, 40, 45, 50, 55, 60, 65, 70, 75, 80, 85
Relative Azimuth	0, 5, 10, 15, 20, 30, 40, 50, 60, 70, 80, 90, 100, 110, 120, 130, 140, 150, 160, 165, 170, 175, 180

In the table, the angles are divided into 18, 18, and 23 intervals for solar zenith, view zenith and relative azimuth, respectively. The total number of regression coefficients set needed for the above angular intervals is 1992. Interpolation is performed for calculating the coefficients set between the gridded solar-view geometry.

Furthermore, the simulation study indicates that, if aerosol model information is applied in deriving the regression coefficient sets, the resulting accuracy of BPSA is improved.

3.3.2.1.11 Bright Pixel Sub-Algorithm (BPSA): Application to Sea Ice pixels

For sea ice pixels since the BRDF information is not available we extend the BPSA algorithm to pixels identified by the sea ice concentration IP as 100% sea ice. Details on the simulations approach and regression coefficient is given in the Appendix A.3.

3.4 ALGORITHM SENSITIVITY STUDIES

3.4.1 EDR Requirements

Table 3.9 lists the requirements from the VIIRS SRD for the Surface Albedo EDR, alongside the VIIRS system specification.

Table 3.9 VIIRS SRD prescribed requirements for the Surface Albedo EDR.

Para. No.		Thresholds	Objectives	Specification
	a. Horizontal Cell Size (HCS)			
V40.5.2-10	1. Moderate, worst case	4 km	0.5 km	1.6 km
V40.5.2-11	2. Fine, at nadir	1 km	0.5 km	0.75 km
V40.5.2-2	b. Horizontal Reporting Interval			HCS
V40.5.2-3	c. Horizontal Coverage	Global	Global	Global
V40.5.2-4	d. Measurement Range	0 - 1.0	0 - 1.0	0 – 1.0
V40.5.2-5	e. Measurement Accuracy (moderate HCS product)	0.05	0.0125	0.025
V40.5.2-6	f. Measurement Precision (moderate HCS product)	0.02	0.01	0.02
V40.5.2-12	i. Measurement Uncertainty (fine HCS product)	0.03		0.03
V40.5.2-7	g. Long-term Stability	0.02	0.01	0.01
V40.5.2-9	k. Minimum Swath Width (All other EDR thresholds met)	3000 km		3000 km

The requirements in Table 3.9 were used as guidance for the derivation of the algorithm. These numbers may not reflect the latest NPOESS system specifications requirements for this product. Reference should be made to the latest version of the system specification document for up to date information.

The specifications set the limits for an error budget in the Surface Albedo EDR. There are four crucial parameters in Table 3.9 that directly constrain the allowable errors in the Surface Albedo: accuracy, precision, uncertainty, and long-term stability. Appendix A of the VIIRS SRD [PS154650] defines these primary metrics for assessment of EDR algorithm performance.

Note that there are really two products required by the SRD: a moderate resolution Surface Albedo driven by edge-of-scan performance, and a fine resolution Surface Albedo driven by nadir performance. Our solution for this EDR produces a single Surface Albedo product to satisfy the moderate and fine requirements, with a nadir resolution of 750 m, growing to a resolution of 1600 m at the edge of the scan.

Note also that Horizontal Coverage is global implying land and ocean surfaces. However, it is well known that albedo retrieval methods for land surface and for ocean surface are significantly different. The algorithm described by this document is for land surface only.

3.4.2 Performance Metrics

Consider a single true value T of an EDR product at the HCS. A satellite-borne sensor will produce data which can be transformed through a retrieval algorithm into an estimate X_i of T , where the index i indicates that any arbitrary number N of such estimates can be made. Various error sources along the pipeline between the true value T and the measured value X_i will cause X_i to deviate from T . The accuracy A_{SRD} is defined in the VIIRS SRD as:

$$A_{SRD} = |\mu - T| \quad (3.30)$$

where μ is the average of all the measured values X_i corresponding to a single true value T :

$$\mu = \frac{1}{N} \sum_{i=1}^N X_i \quad (3.31)$$

The accuracy can therefore also be termed as a bias, and is a direct comparison between the measurements X_i and the true value T .

The precision P_{SRD} is defined in the SRD as the standard deviation of the measurements:

$$P_{SRD} = \left(\frac{1}{N-1} \sum_{i=1}^N (X_i - \mu)^2 \right)^{1/2} \quad (3.32)$$

Thus, the actual calculation of the precision as defined in the SRD is completely independent of the true value T , however it is important to keep in mind that the precision is still defined only for measurements corresponding to a single value of T . Were this not so, P_{SRD} would describe only the natural variability of the parameter being measured, and this would preclude its use as a measure of algorithm performance.

The uncertainty U is defined as:

$$U_{SRD} = \left(\frac{1}{N} \sum_{i=1}^N (X_i - T)^2 \right)^{1/2} \quad (3.33)$$

The uncertainty is therefore alternatively known as the root mean square (RMS) error between the measurements X_i and the true value T .

As mentioned in the SRD, the definitions of accuracy, precision, and uncertainty given in Equations (3.30), (3.32), and (3.33), respectively, are idealized, because they assume a single value of T . In reality, this cannot be implemented, because there are an infinite number of possible values for T , each possible value is likely to be manifested as truth only once, and we cannot hope to pinpoint T to arbitrary accuracy. The practical implementation of the SRD definitions is to bin the possible values of T into small ranges that are large enough to provide a statistically significant number of test points but small enough to ensure

the metrics are not dominated by natural variability. The simplest result would be a modification of equations (3.30), (3.32), and (3.33) into the following:

$$A = |\mu - \mu_T| \quad (3.34)$$

$$P' = \left(\frac{1}{N-1} \sum_{i=1}^N (X_i - \mu)^2 \right)^{1/2} \quad (3.35)$$

$$U = \left(\frac{1}{N} \sum_{i=1}^N (X_i - T_i)^2 \right)^{1/2} \quad (3.36)$$

Thus, precision P' would be equivalent to P_{SRD} , only it is understood that P' now corresponds to some small range of true values T_i , instead of one true value T . The single value of T in the accuracy definition is now changed to the mean of the true values T_i within some small range, and the single value of T in the uncertainty definition is now changed to the particular true value T_i corresponding to the measurement X_i .

Equations (3.34), (3.35), and (3.36) now exactly correspond to the bias, standard deviation of the measurements, and RMS error, respectively. These are all quite common statistical measures. The accuracy A will give a clear indication of any biases in the processing pipeline for a given EDR, and the uncertainty U will provide a good measure of overall error. A problem arises, however, in using P' as a metric for evaluating retrieval errors. Since P' corresponds to a small range of true values T_i , but it does not explicitly account for the variations in T_i , it now includes the natural variability of the parameter being measured. In fact, without incorporating the true values T_i into the equation, P' becomes ambiguous.

Consider, as an example, the effects of band-to-band misregistration on the Surface Albedo EDR. The following would apply for some small range of true values, say from 0.40 to 0.42. "Truth" would be an albedo value within this range for a horizontal cell in which the input bands are completely overlapping. An ensemble of true values T_i could then be created using a two dimensional Landsat TM scene. For each of these horizontal cells, the near infrared band could then be shifted 30 meters to the right with respect to the other bands, and new "measured" values X_i of the albedo could be obtained to match up with the true values T_i . These measured values X_i could be plugged into Equation (3.35) to obtain an estimate of the precision for 30-m misregistration. The process could then be repeated for 60-m misregistration.

But note that nowhere do the true values T_i enter into Equation (3.35). The result is that the precision for the 60-m misregistration scenario is likely to be almost exactly the same as the precision for the 30-m misregistration scenario, because it is only a measure of the variability within the scene. Additionally, precision as defined by P' is a strong function of bin

size. If the albedo is binned into ranges that are 0.1 albedo units wide, the precision for each bin will become much higher, because the truth varies over a broader range.

P_{SRD} is a very useful metric for data points which correspond to a single value of truth T , such as in simulations conducted for sensor signal to noise ratio (SNR). But for spatial and temporal fields of truth T_i which must be binned into small ranges, P' fails as an extension of P_{SRD} . It is therefore recommended in these special situations that the precision definition P' be replaced by a system-level expression that ensures uncertainty is the root sum square of accuracy and precision:

$$P = (U^2 - A^2)^{1/2} \quad (3.37)$$

In other words, precision P now corresponds to the bias-adjusted RMS error for situations with variable truth. This provides a metric that captures the spread of the measurements about the truth, with the bias associated with the accuracy metric removed to distinguish it from the total error given by the uncertainty. Further, P is not a strong function of bin size; P for a large range of albedo values is roughly equivalent to the average of P for several smaller ranges within the large range. Finally, Equation (3.37) is explicitly called out in the SRD as a limiting relationship for A , P , and U when the number of observations in a given bin becomes very large.

3.4.3 Individual Error Sources

The following sections discuss the major error sources for the Surface Albedo EDR.

3.4.3.1 Past Sensor Error Evaluations

Previous activities included a necessary look at the flow down of EDR requirements to algorithm data definitions (ADDs) for the output of the sensor. These included dynamic range, radiometric calibration and sensitivity, spatial resolution, polarization characteristics, and so forth. Because of the demanding requirements for other products, such as Ocean Color, Sea Surface Temperature, and Imagery, Surface Albedo was not the single driver for any of these parameters. The major sensor error sources will now be discussed in brief, however, to provide further context for the error budget. The following discussion focuses primarily on the algorithms developed under the previous version of Y2398 trade studies; sensor impacts on the adapted MODIS approach (the DPSA) are discussed in Lucht *et al.* (2000).

3.4.3.1.1 Sensor Noise

A real sensor, even if perfectly calibrated, will convert a true top-of-atmosphere (TOA) radiance to a corresponding measured radiance that departs from the truth by some random amount, leading to noise in an ensemble of measurements. The major contributors to sensor noise are: photon or "shot" noise, caused by natural variations in the number of photons striking the instrument; detector and electronics noise, typically constant for a given detector; and quantization noise, caused by the conversion of continuous radiance into a finite number of bits. On the whole, sensor noise can be treated with good fidelity as Gaussian.

This assumption breaks down at the limits of the sensor's dynamic range, however it was sufficiently accurate for flow down of sensor noise requirements at specified radiances. The reader is directed to Hucks (1998) for a more detailed description of the sensor noise modeling process. It is only briefly summarized here. The VIIRS radiometric performance model describes the sensor noise as a function of TOA band radiance, N_{TOA} as,

$$\sigma = \sqrt{\alpha N_{TOA} + \beta} \quad (3.38)$$

where N_{TOA} , a band radiance in units of $\text{Wm}^{-2}\text{sr}^{-1}$, is chosen as a naming convention to differentiate it from L_{TOA} , the spectral radiance in $\text{Wm}^{-2}\text{sr}^{-1}\mu\text{m}^{-1}$. The quantity σ is the standard deviation of the signal caused by sensor noise, assuming a Gaussian distribution.

The values α and

associated with sensor noise, including measured detector characterizations, integration time, instantaneous field of view (IFOV), optical throughput, and so forth. These constants as supplied by SBRS for the specified level of sensor noise in the appropriate bands, resulted in negligible errors for the Surface Reflectance IP, as they were typically on the order of 0.005 reflectance units or less.

□ are tw

When the DPSA was adopted as the baseline algorithm for the Surface Albedo EDR, the sensor noise error term was folded into the TOA reflectance error, discussed shortly in Section 3.4.3.5. These results confirmed that sensor noise has negligible effects on the Surface Albedo EDR, due to the very low-noise performance of the VIIRS driven by other EDRs. A similar situation exists for MODIS, so that radiometric calibration is considered the only significant sensor error source for the MODIS albedo algorithm. Early results from MODIS (e.g., Schaaf et al, 2002) indicate that the MODIS instrument performs sufficiently well to deliver a reliable albedo product. The analyses already conducted for the Surface Reflectance IP [Y2411] suggested that the DPSA will be insensitive to sensor noise errors from the VIIRS.

The BPSA is directly calculated from the TOA reflectance data using a linear regression equation (Equation 3.28). Theoretically, the error transferred from TOA reflectance into the BPSA is a weighted sum of the TOA reflectance along the bands from M1 to M11 except M6 and M9. The regression coefficients, which are all less than one, are the weight values. Sections 3.4.3.5 shows that TOA reflectance errors on these bands are negligible, therefore their weighted sum is also negligible.

3.4.3.1.2 Radiometric Calibration

The VIIRS Sensor Specification [PS154650] for the upper bound on radiometric calibration accuracy is 2% in the reflective bands. This was largely driven by ocean and aerosol requirements. The absolute nature of the Surface Albedo EDR requirements, however, allows significantly more room for relative error than is the case for ocean and aerosol products. In fact, from the standpoint of meeting the EDR requirements, the most significant impacts of sensor calibration errors for Surface Albedo occur for the brightest surfaces, especially snow. For these surfaces, the BPSA is employed to retrieve the Surface Albedo EDR to specification quality, and so calibration errors are folded into TOA reflectance error, which is discussed in Section 3.4.3.5. It is expected that both MODIS and VIIRS possess

sufficiently tight specifications on radiometric accuracy that the performance of albedo retrieval algorithms over dark surfaces will be sufficient to meet the product-level requirements. Early results from MODIS (e.g., Schaaf *et al.*, 2002) seem to verify this.

3.4.3.1.3 MTF Effects

The most likely scientific interpretation of a “perfect” pixel would be one that perfectly represented the averaged radiance over some square region on the Earth’s surface. The average should be equally weighted across the entire square, with no contributions from outside the borders. In reality, of course, this is not achieved. A pixel will instead be the result of several convolutions, due to scattered and stray light, diffraction, blurring, the finite nature of the detector, and so forth. This will have the effects of varying the weighting within the target region on the surface and incorporating photons which came from outside this region, either from surrounding regions on the surface or from entirely different sources such as clouds. The ultimate effect of all these convolutions can be represented as the sensor point spread function (PSF), which typically has some central peak near the center of the target region, around which the radiances contributed from surrounding areas of the Earth’s surface drop off in a typically exponential manner. The Modulation Transfer Function (MTF) is defined as the magnitude of the Fourier transform of the PSF.

There is some debate as to whether the deviation of a real sensor PSF from a "boxcar" idealized pixel is a real error. For verification purposes, the issue is moot, since ground measurements will not match the sensor PSF or the boxcar. Previous studies have included a look at MTF errors for a simplified, Lambertian-based, linear regression approach to albedo retrievals, and the EDR was found not to be the most significant driver. In fact, Vegetation Index [Y2400] was a much stronger driver.

3.4.3.1.4 Band to Band Registration

Any two given bands on the VIIRS instrument would ideally project to perfectly aligned pixels at the same spot on the ground. In reality, any two given bands will be offset in an arbitrary direction from one another, causing errors in VIIRS EDR retrieval algorithms.

As with MTF errors, this issue was considered early in the development for Surface Albedo, and does not contribute significantly to the total error budget for Surface Albedo.

3.4.3.2 Atmospheric Correction Errors

There are four major sources of atmospheric noise in the reflective portion of the spectrum: water vapor absorption, ozone absorption, Rayleigh scattering, and aerosol extinction. For the reflective bandwidths on VIIRS, ozone and water vapor absorption sensitivity is minimal, as gaseous absorption features have been avoided, and the available ancillary data are sufficiently accurate to robustly remove the effects on TOA radiance. Rayleigh scattering and aerosol effects are typically on the same order, and both decrease in importance moving toward longer wavelengths. Because of their variability, aerosols are the dominant error source for the Surface Reflectance IP. The Surface Reflectance algorithm internal to the VIIRS pipeline is based upon the MODIS atmospheric correction product (Vermote and

Vermeulen, 1999). In both products, all four of the above sources of atmospheric noise are handled. Additionally, BRDF/atmospheric coupling effects are taken into account, and a placeholder exists for the eventual handling of adjacency effects. For details on sources and magnitudes of errors in the Surface Reflectance IP, and for a summary of overall performance, the reader is directed to [Y2411]. The flow down of these errors into the DPSA are discussed in some detail in Lucht *et al.* (2000), including the errors involved in the diffuse skylight computation. Lewis and Barnsley (1994) found this approximation to be on the order of only a few percent even for low solar zenith angles, where the direct beam is most dominant. Since MODIS and VIIRS are spectrally and radiometrically similar, the differences are expected to be minimal.

3.4.3.3 BRDF Effects

The magnitude of the errors associated with BRDF approximation for the DPSA are described in the context of MODIS retrievals by Lucht *et al.* (2000). Assessment of the BRDF modeling performance for VIIRS will leverage the validation efforts for MODIS.

In this algorithm, field data sets listed in Table 3.10, are used to test the kernel model BRDF inversion algorithm. The data are collected from NASA's First ISLSCP (International Satellite Land Surface Climatology Project) Field Experiment (FIFE) and Boreal Ecosystem/Atmosphere Study (BOREAS) experiment, via Portable Apparatus for Rapid Acquisition of Bidirectional Observations of Land and Atmosphere (PARABOLA) and Modular Multiband Radiometer (MMR) instruments. Information about the FIFE and BOREAS data may be found through the web sites, http://www-eosdis.ornl.gov/FIFE/FIFE_Home.html and http://www-eosdis.ornl.gov/BOREAS/bhs/BOREAS_home.html, respectively. The experimental results to date indicate that the described VIIRS BRDF algorithm performs very well. Figure 3.4 shows an example, where the three bands are from visible to near-infrared channel and the *comb* represents the model combination number listed in Table 3.7 of Section 3.3.2.1.2.2.

Table 3.10 Field data sets from NASA's FIFE and BOREAS experiment

Data set	Surface Type	Date	values
ssa-9oa	Aspen Tree	07/21/94	546
ssa-ojp	old jack pine	07/14/94	540
ssa-obs	old black spruce	06/07/94	432
72272655	grassland	08/15/87	546
92162133	grassland	08/04/89	312

The best model inverted for the data is Ross-thick and Li-Sparse, with RMSE error less than 0.02.

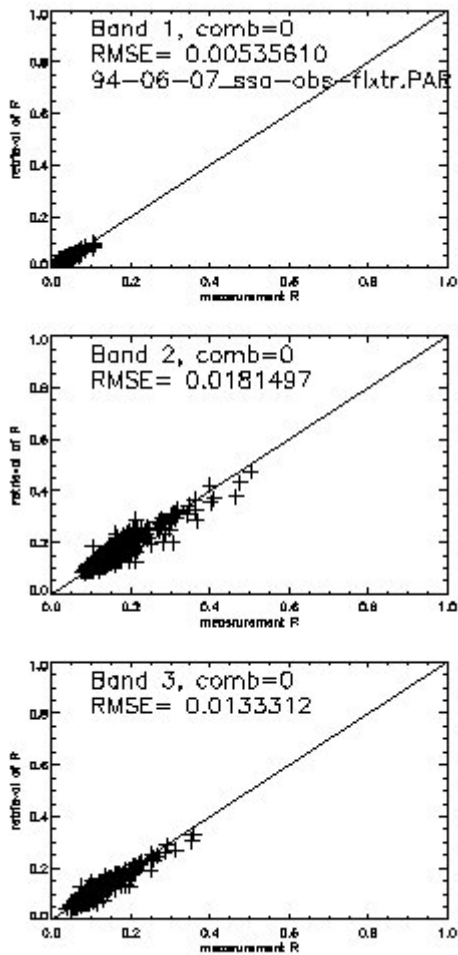


Figure 3.4 Plots of retrieved reflectance vs. measurement reflectance of data set ssa-obs.

The Different crown relative height and shape values (see Table 3.6 of Section 3.3.2.1.2.2) are tested to see how changes of these ratios may affect the BRDF shape. Table 3.11 presents an example of this test result, using field data ssa-obs from FIFE program.

Table 3.11. Height (h/b) /Shape (b/r) sensitivity

Co mb #	RMSE vs Height/Shape					
	1.0/1.0	1.0/2.5	1.0/4.0	2.0/1.0	2.0/2.5	2.0/4.0
0	0.0141	0.0143	0.0145	0.0138	0.0143	0.0145
1	0.0187	0.0199	0.0203	0.0187	0.0202	0.0206
2	0.0144	0.0184	0.0199	0.0143	0.0188	0.0201
3	0.0193	0.0221	0.0230	0.0192	0.0226	0.0232
4	0.0162	0.0173	0.018	0.0166	0.0180	0.0187
5	0.0199	0.0204	0.0210	0.0206	0.0213	0.0218
6	0.0123	0.0135	0.0140	0.0132	0.0147	0.0149

7	0.0146	0.0150	...	0.0157	0.0164	...
8	0.0167	0.0173	0.018	0.0167	0.0180	0.0187
9	0.0210	0.0204	0.0210	0.0207	0.0213	0.0218
10	0.0248	0.0256	0.0258	0.0248	0.0256	0.0258
11	0.0313	0.0320	0.0322	0.0313	0.0320	0.0322

The BRDF retrieval algorithm is also tested using simulation data. To do so the Ross-thick Roujean's BRDF model (model 10 of Table 3.6) is used to generate surface reflectance data. The inversion process is then applied on the simulation data to retrieve the BRDF shape using all the model combination except the Ross-thick Roujean's BRDF model. A Gaussian distributed noise is then added to the simulation data to test if the algorithm still works in certain noise levels. Surprisingly, the algorithm filters out the noise and retrieved the original data very well if the noise is under certain level. The filtering feature is displayed in Figure 3.5. In the figure frame, the left figures show (from top to bottom) actual data with no noise, with noise level 0.05, and with noise level 0.1. While the right figures show the corresponding retrieved reflectance. This time, the best combination number of the kernel models is 6, the Ross-thick and non-reciprocal Li-Dense model. It is interesting to see that even when the noise (up to 10%) is added to the input reflectance data, the retrieved BRDF shape is still close enough to the original data.

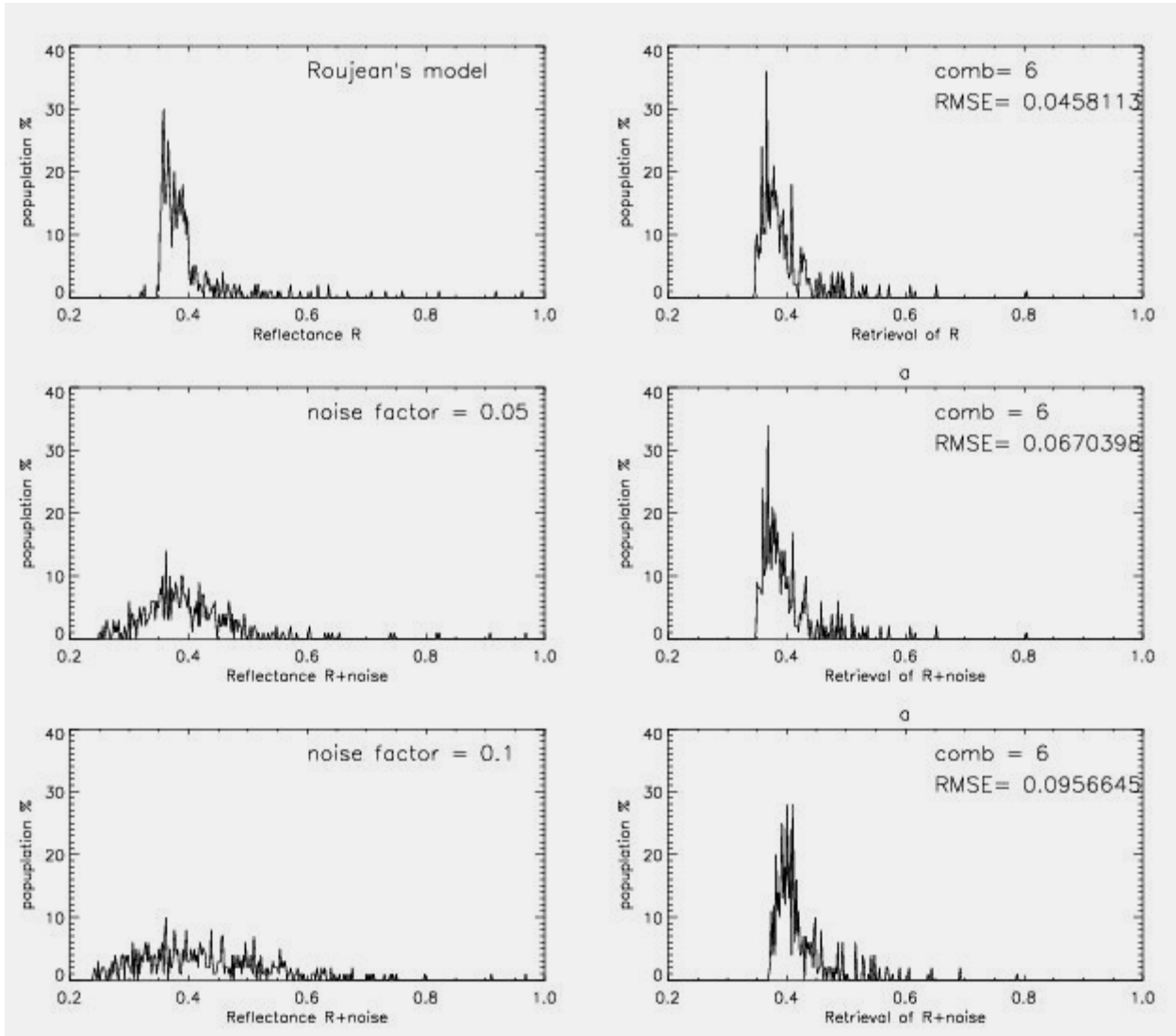


Figure 3.5. Histogram of the actual and retrieved reflectance using simulation data.

3.4.3.4 Narrow to Broadband Conversion

The conversion from spectral to broadband albedo depends on several factors. These include: the atmospheric state; the underlying surface type; the number of chosen spectral bands; the band specifications (bandcenter, bandwidth); and the chosen associated weights or coefficients for the conversion. The narrow to broadband conversion issue was investigated for a simplified, Lambertian-based, linear regression approach to albedo retrievals. In order to evaluate the performance of the Lambertian-based algorithm, several surface types—vegetation, soil, snow and water—were simulated using data from the ASTER Spectral Library (<http://speclib.jpl.nasa.gov>). All atmospheric simulations were performed using the 6S radiative transfer code (Vermote *et al.*, 1997). The US Standard atmosphere was employed for all the simulations. The investigated combinations of VIIRS, MODIS, and AVHRR bands are listed in Table 3.12. Also investigated were bands M6 (746

nm, used for atmospheric correction over oceans), M9 (1.38 μm , used for cirrus and stratospheric aerosol retrievals), MODIS band 6 (1.64 μm), and AVHRR bands 1 and 2.

Table 3.12. Indexed combinations of channels considered for conversion from narrow to broadband albedo for previous evaluation of the Lambertian-based regression algorithm.

Combination	Set of Bands Used
1	M1, M2, M3, M4, I1, M6, I2, M8, M9, I3, M11
2	Same as 1, but without M9 (1.38 μm)
3	Same as 1, but without M6 (746 nm)
4	Same as 1, but without M6 or M9
5	M3, M4, I1, I2, M8, I3, M11
6	M3, M4, I1, I2, I3, M11
7	M3, M4, I1, I2, MODIS band 6 (1.628-1.652 μm), M11
8	M3, M4, I1, I2, MODIS band 6 (1.628-1.652 μm), M8, M11
9	AVHRR bands 1 (572-703 nm) and 2 (720-1000 nm)
10	M4, I1, I2, MODIS band 6 (1.628-1.652 μm), M11
11	I1, I2, MODIS band 6 (1.628-1.652 μm), M11
12	M4, I2, MODIS band 6 (1.628-1.652 μm), M11
13	I1, I2, M11
14	I1, I2, MODIS band 6 (1.628-1.652 μm)
15	I1, I2, I3

Figure 3.6 illustrates the errors using the various combinations of spectral bands. A number of observations can be made. First, the minimum error is obtained using combination 5, which corresponds roughly to the Landsat Thematic Mapper (TM) bandset. The BPSA baseline for VIIRS uses these bands plus M1 and M2 to increase information about atmospheric scattering. For the purpose of data continuity, a comparison between VIIRS and AVHRR derived albedo is also of interest. The narrow to broadband conversion using only the red and near infrared bands (combination 9) shows reasonable results for all surface types but snow, where the VIIRS performs considerably better than the AVHRR. The most recent heritage for AVHRR includes a switchable band at 1.61 μm —the same wavelength as for VIIRS band I3—that should improve performance. In fact, combination 15—the three imagery-resolution reflective bands for VIIRS—yields reasonable results for all surface types. This suggests most of the important spectral information characterizing the surface can be found in these three bands.

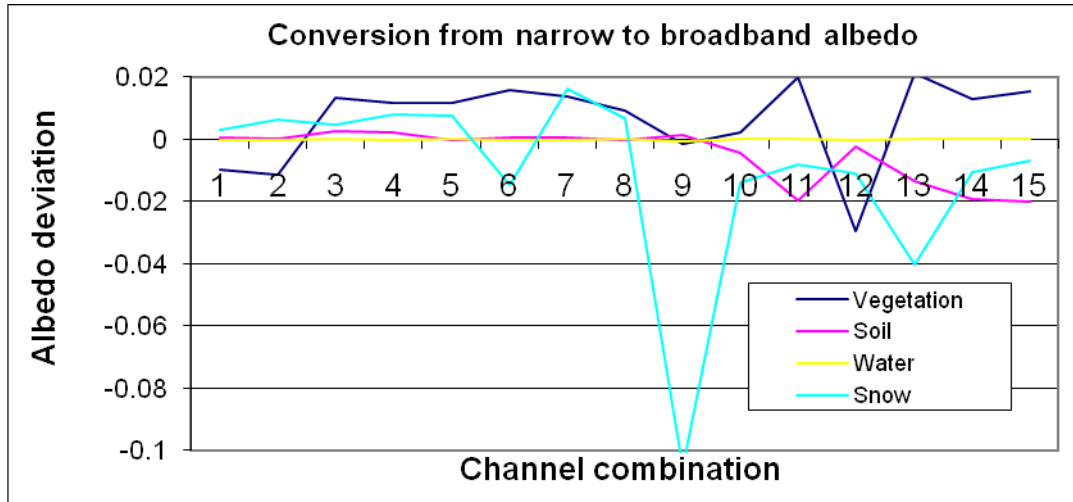


Figure 3.6. Narrow to broadband albedo conversion errors from previous evaluation of a Lambertian-based linear regression algorithm, using the combinations of channels listed in Table 9 for four different backgrounds.

In this algorithm, the DPSA narrow to broadband conversion is accomplished using the coefficients based on extensive radiative transfer simulation and multivariate regression analysis. The BPSA includes narrow to broadband conversion implicitly in the regression equation, and so this term is embedded in the algorithmic error.

3.4.3.5 TOA Reflectance Errors

The primary input to the BPSA is TOA reflectance. Consequently, the stratified performance for TOA reflectance in the relevant bands was investigated using a large ensemble of “stick model” simulations – successive single-point executions of MODTRAN 3.7 (MODerate resolution TRANsmission model) using various viewing and solar geometries, aerosol properties, and surface types. The dimensions of this data set are summarized in Table 3.13.

Table 3.13. Summary of dimensions for the TOA Reflectance and BPSA stick modeling data set.

Parameter	# Different Values	Range
Surface Type	10	Coniferous forest, deciduous forest, shrub, grass, crops, urban, snow, bare soil, desert sand, water
Solar Zenith	8	0-70 degrees
Scan Angle	7	0-60 degrees
Relative Azimuth	5	0-180 degrees
Aerosol Type	4	Urban, rural, desert, LOWTRAN maritime
Aerosol Optical Thickness	5	0.1-0.5

All forward modeling was conducted using MODTRAN 3.7, with a mid-latitude summer profile. It was not deemed necessary to vary the profile, as water vapor, temperature, and ozone effects are much smaller than the effects of aerosols in the VIIRS bands used for reflectance-based land EDRs. The output of each stick model simulation consisted of a true broadband surface albedo, true TOA reflectance values in the nine spectral bands from Table 2.1, and true surface reflectance values in these same bands. Sensor noise for the VIIRS sensor was simulated using the methodology briefly described in Section 3.4.3.1.1. The constants α and β were set corresponding roughly to the sensor specification for the various bands required by the Surface Albedo EDR. These were combined with a simulated value of 2% reflectance calibration accuracy across all bands to give the performance results plotted in Figure 3.7 through Figure 3.15. For each of these plots, the accuracy originates with the calibration errors, and the precision originates with sensor noise. It is clear from these plots that sensor noise is negligible for the purposes of the BPSA, and that calibration errors are minor except for bright surfaces, primarily snow and desert. As shall be seen in Section 3.4.3.6, even with the specified calibration errors over snow and desert, the BPSA appears to meet the threshold accuracy requirement of 0.05 for all conditions.

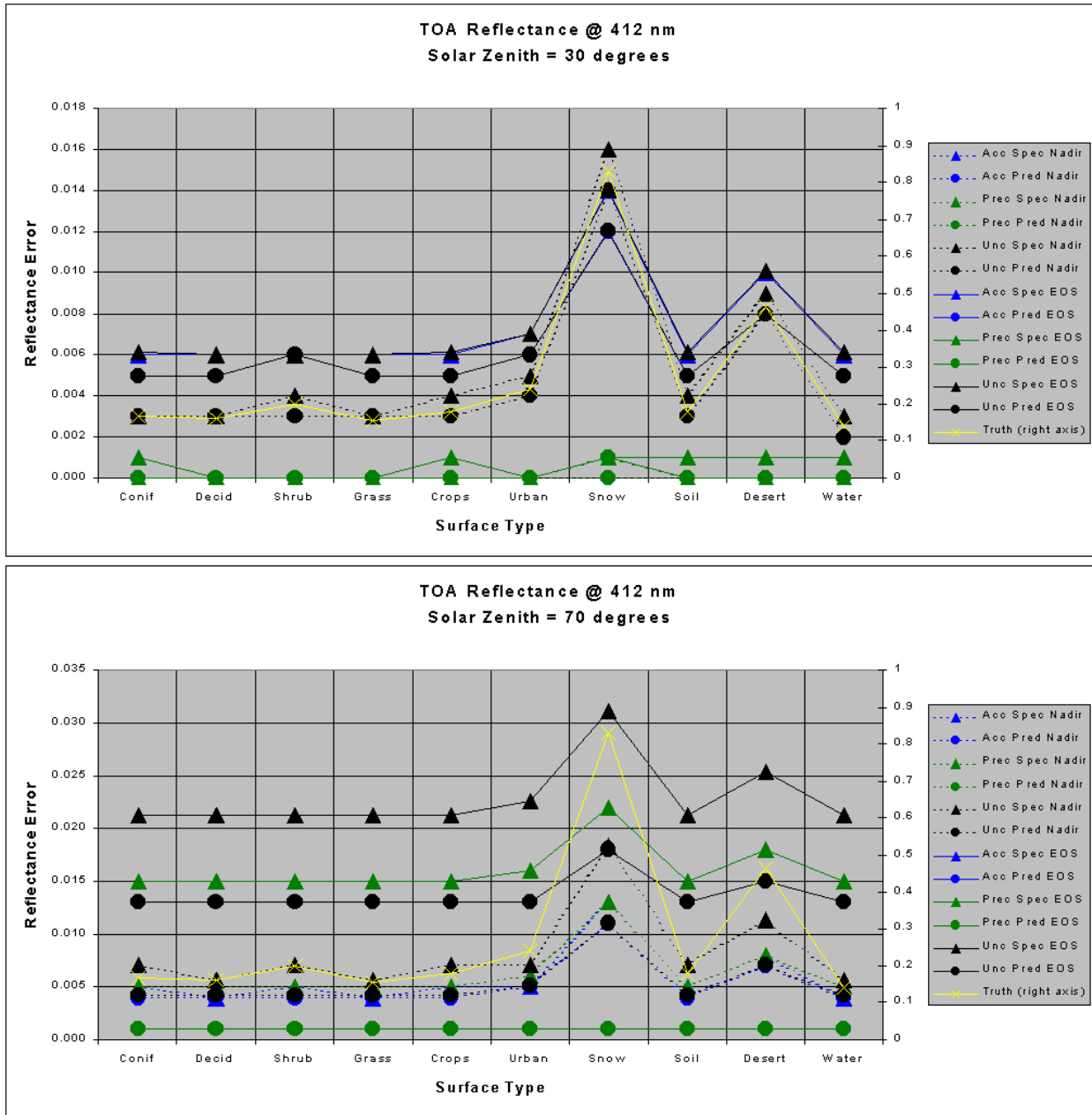


Figure 3.7 TOA reflectance errors at 412 nm, for nadir and edge of scan, at solar zenith of 30 degrees (top) and 70 degrees (bottom), using both specified and predicted sensor performance as input.

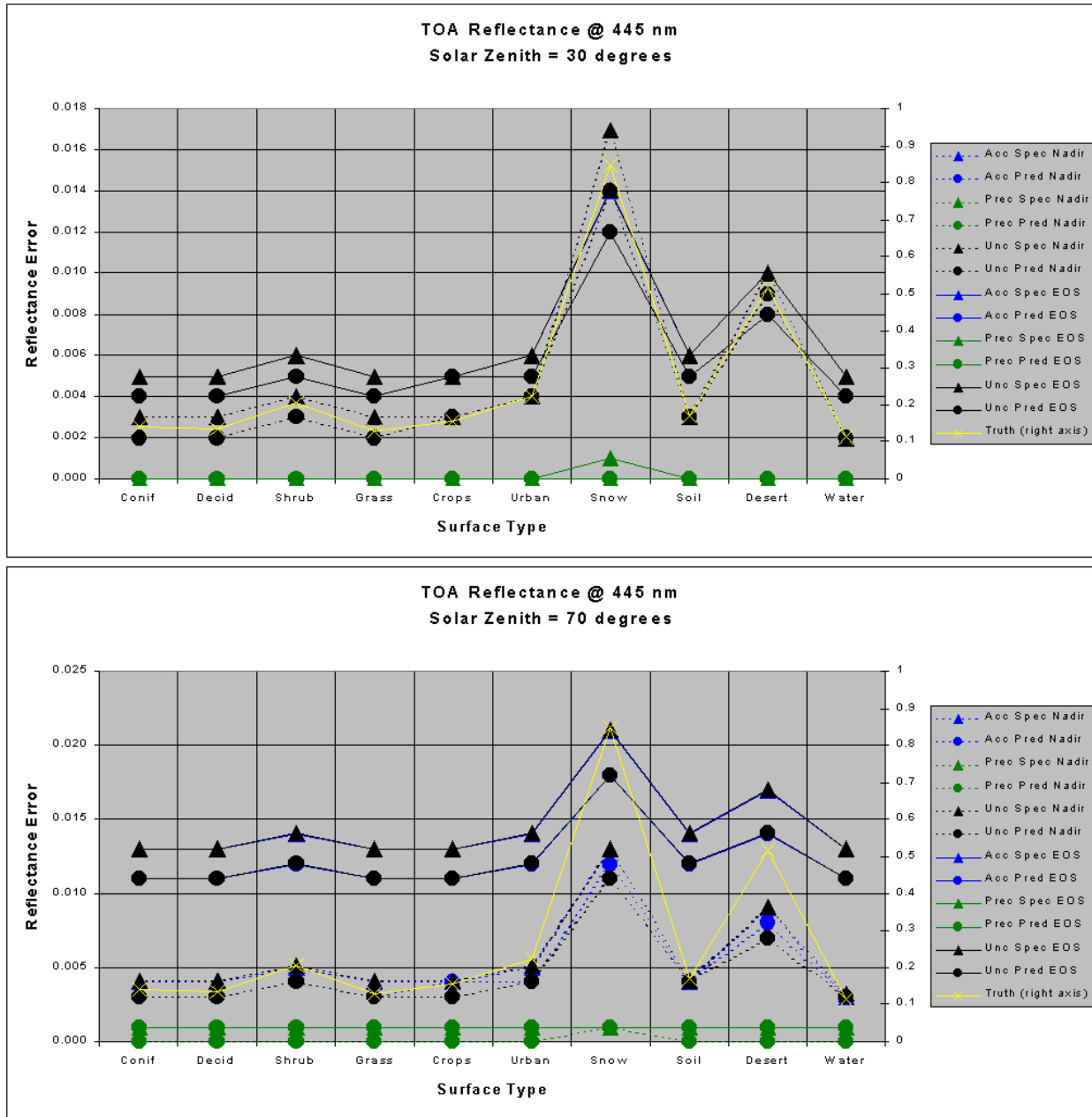


Figure 3.8 TOA reflectance errors at 445 nm, for nadir and edge of scan, at solar zenith of 30 degrees (top) and 70 degrees (bottom), using both specified and predicted sensor performance as input.

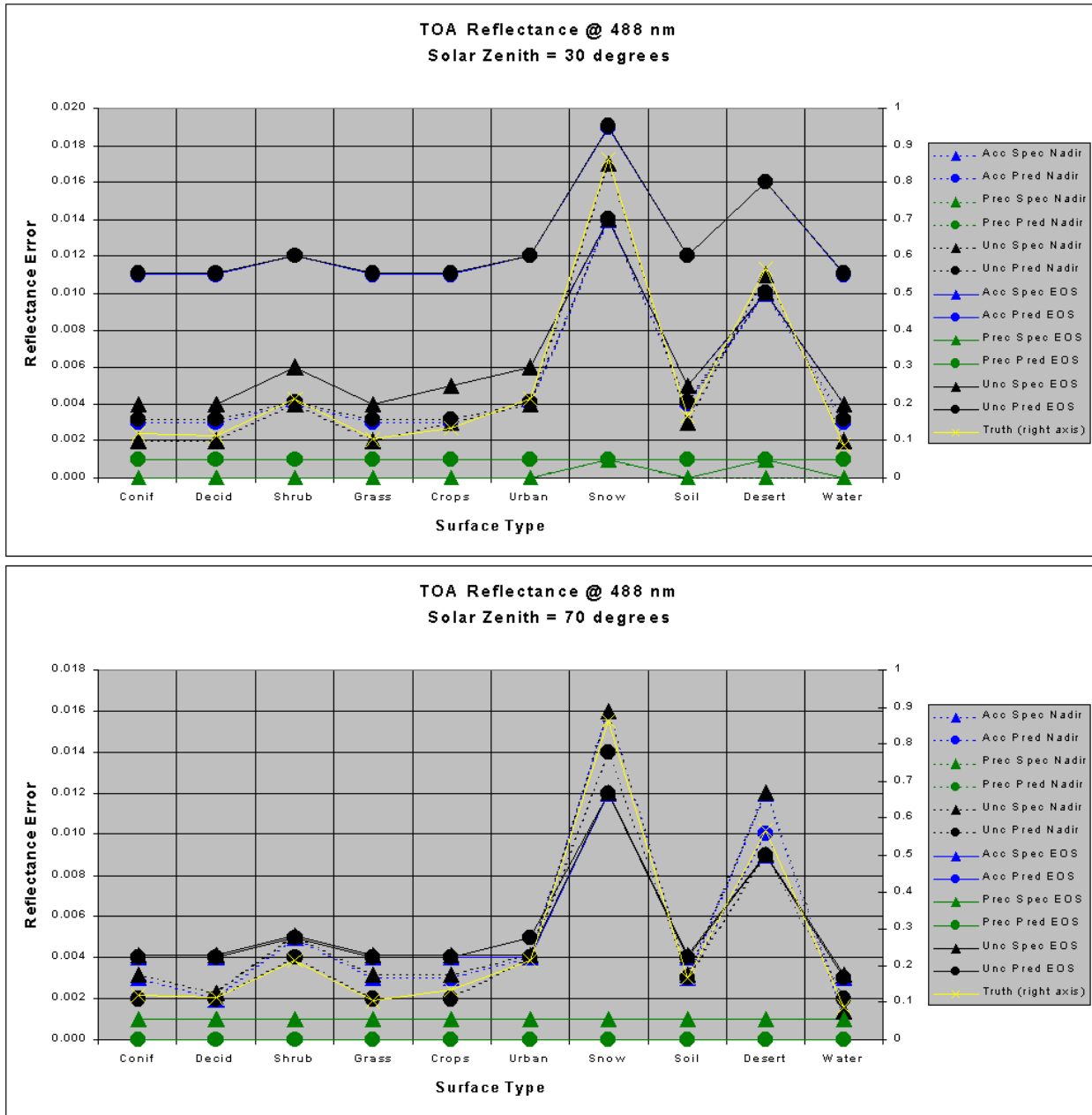


Figure 3.9 TOA reflectance errors at 488 nm, for nadir and edge of scan, at solar zenith of 30 degrees (top) and 70 degrees (bottom), using both specified and predicted sensor performance as input.

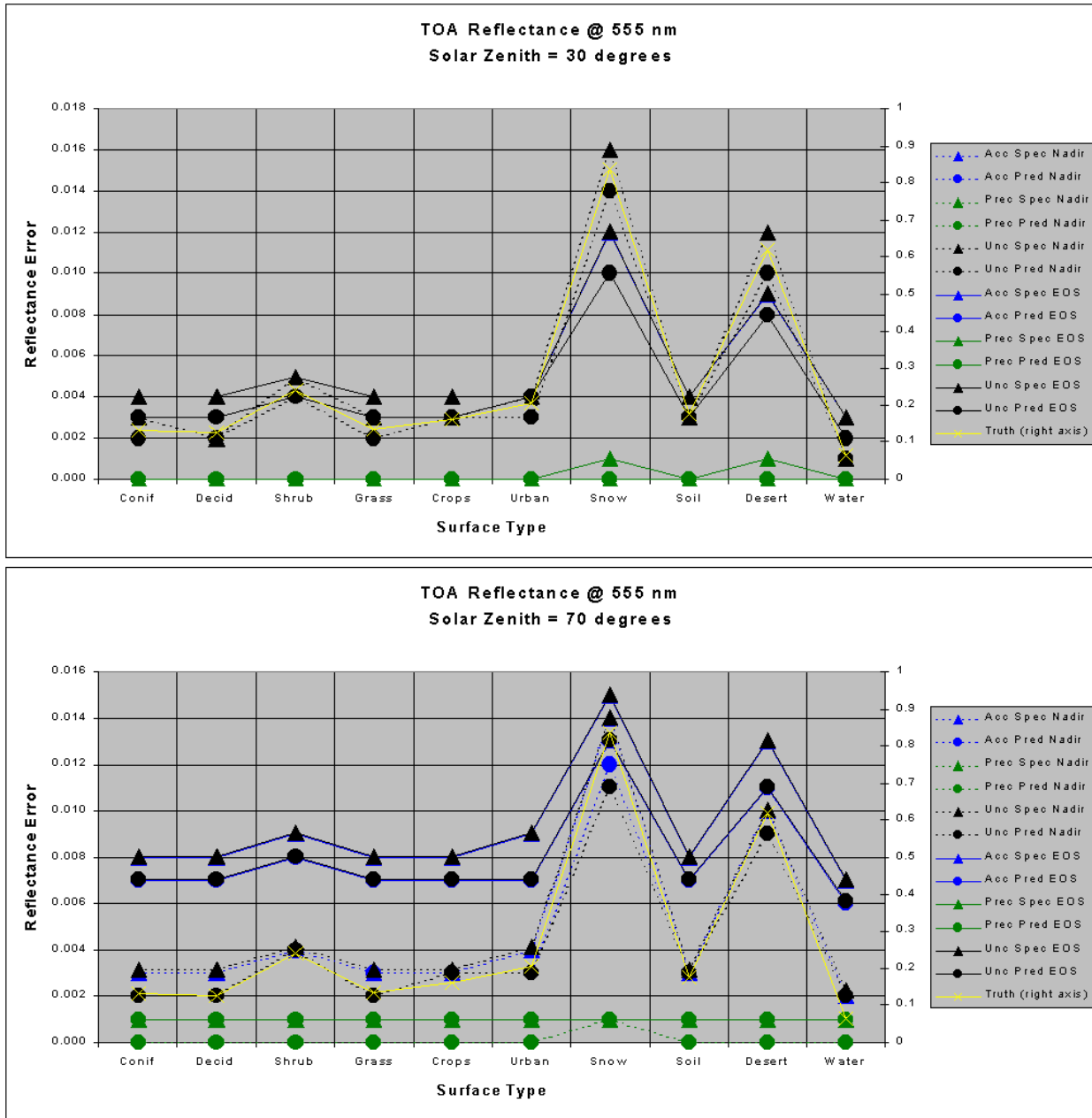


Figure 3.10 TOA reflectance errors at 555 nm, for nadir and edge of scan, at solar zenith of 30 degrees (top) and 70 degrees (bottom), using both specified and predicted sensor performance as input.

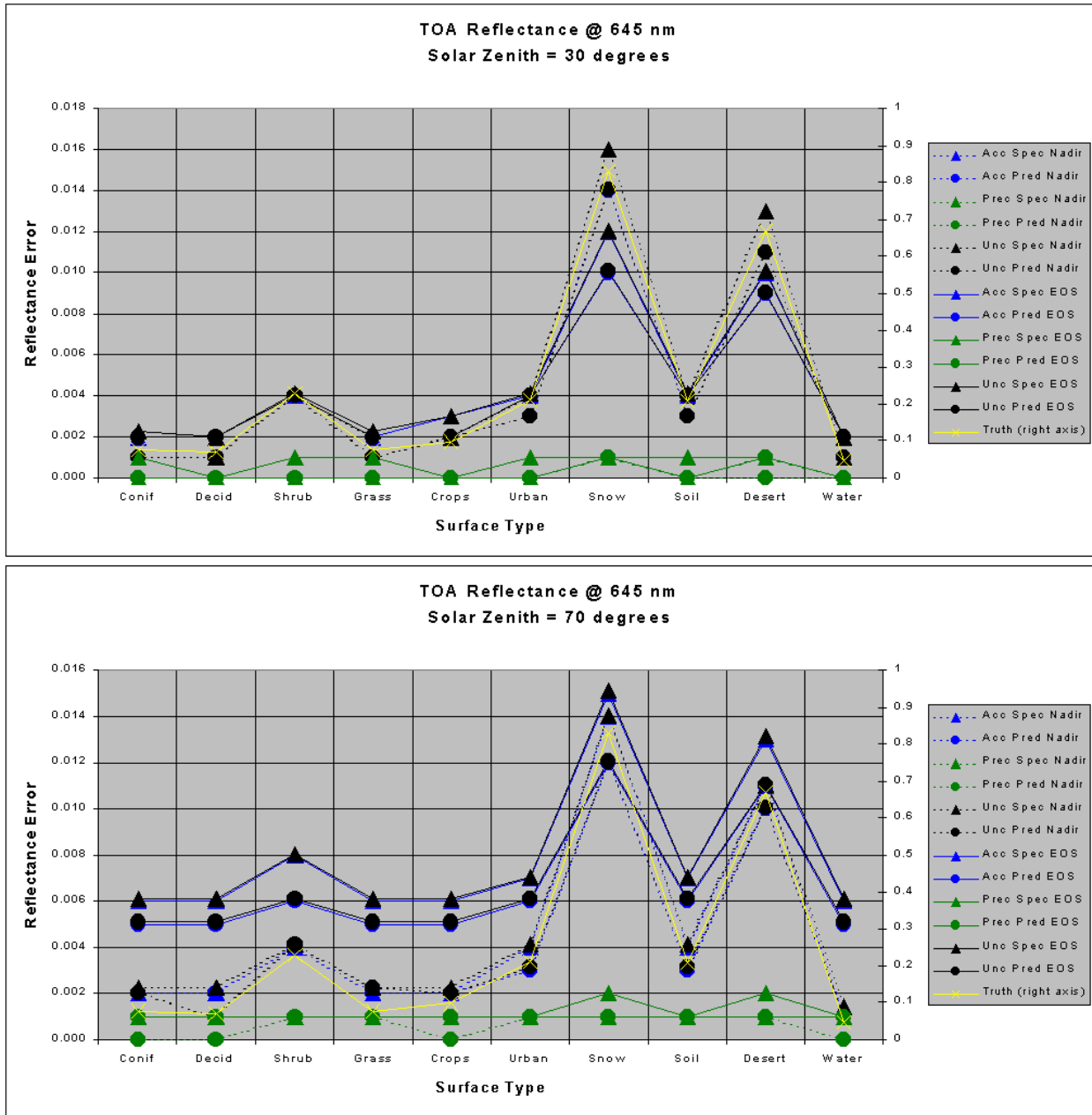


Figure 3.11 TOA reflectance errors at 645 nm, for nadir and edge of scan, at solar zenith of 30 degrees (top) and 70 degrees (bottom), using both specified and predicted sensor performance as input.

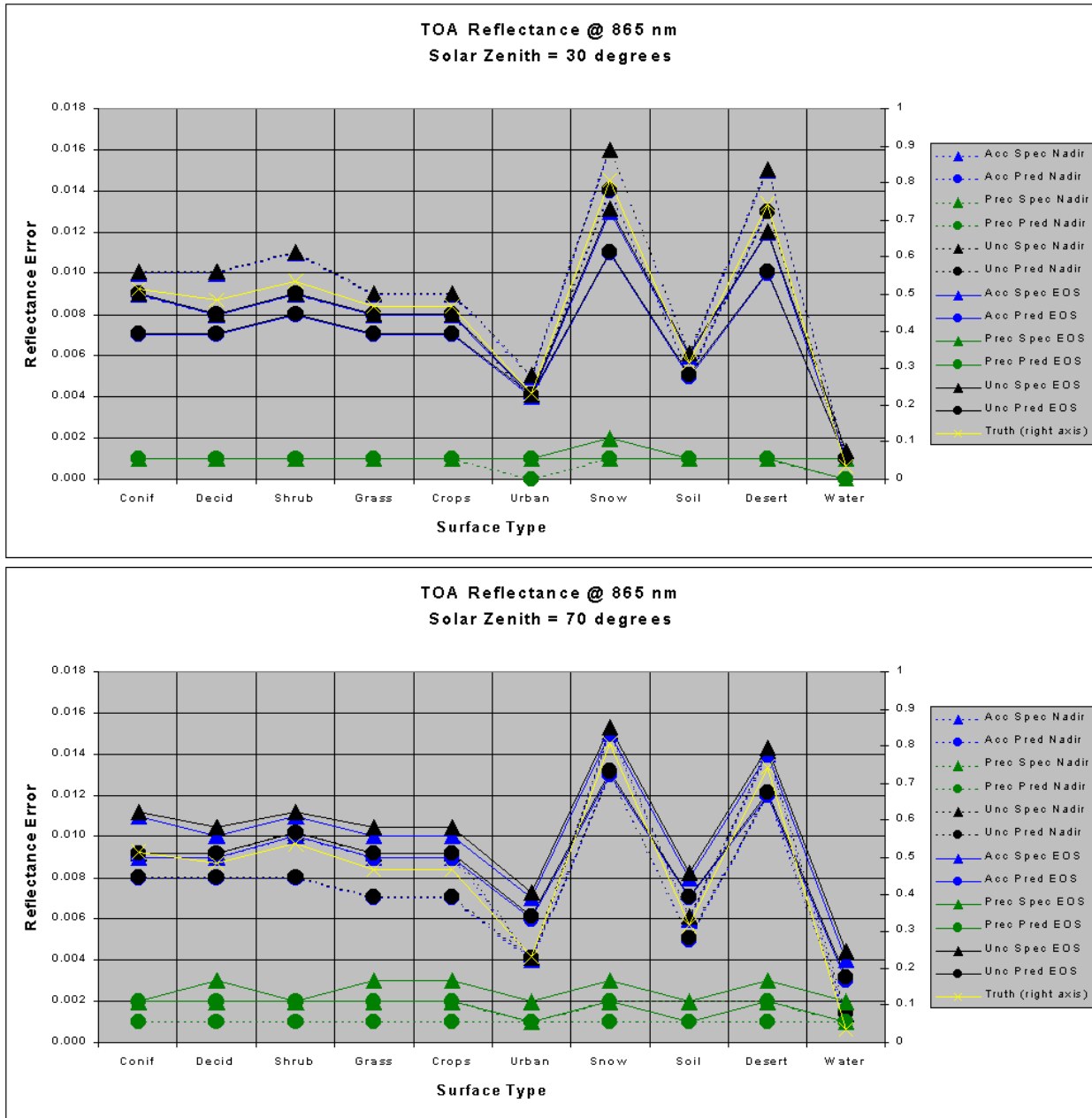


Figure 3.12 TOA reflectance errors at 865 nm, for nadir and edge of scan, at solar zenith of 30 degrees (top) and 70 degrees (bottom), using both specified and predicted sensor performance as input.

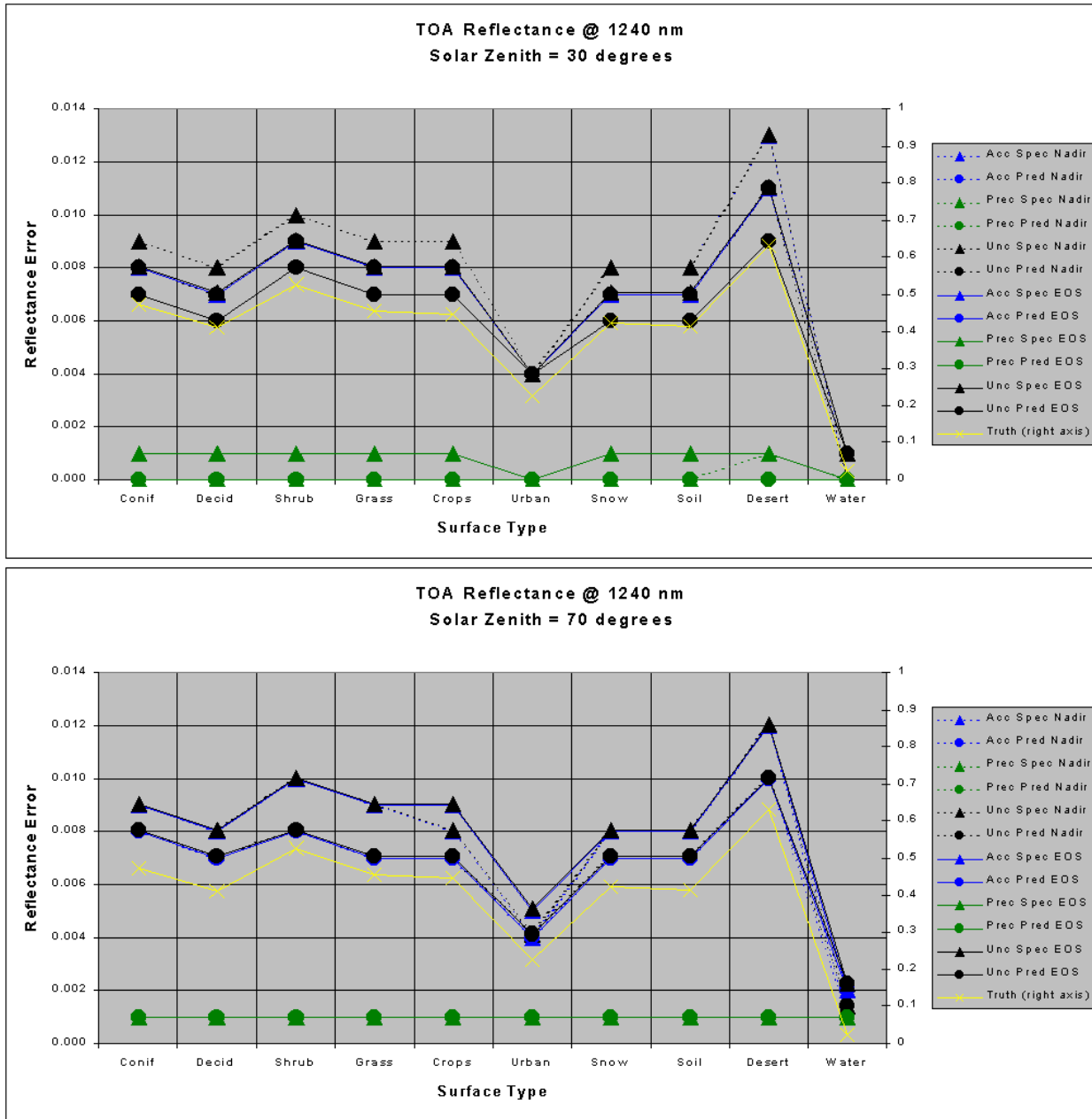


Figure 3.13 TOA reflectance errors at 1240 nm, for nadir and edge of scan, at solar zenith of 30 degrees (top) and 70 degrees (bottom), using both specified and predicted sensor performance as input.

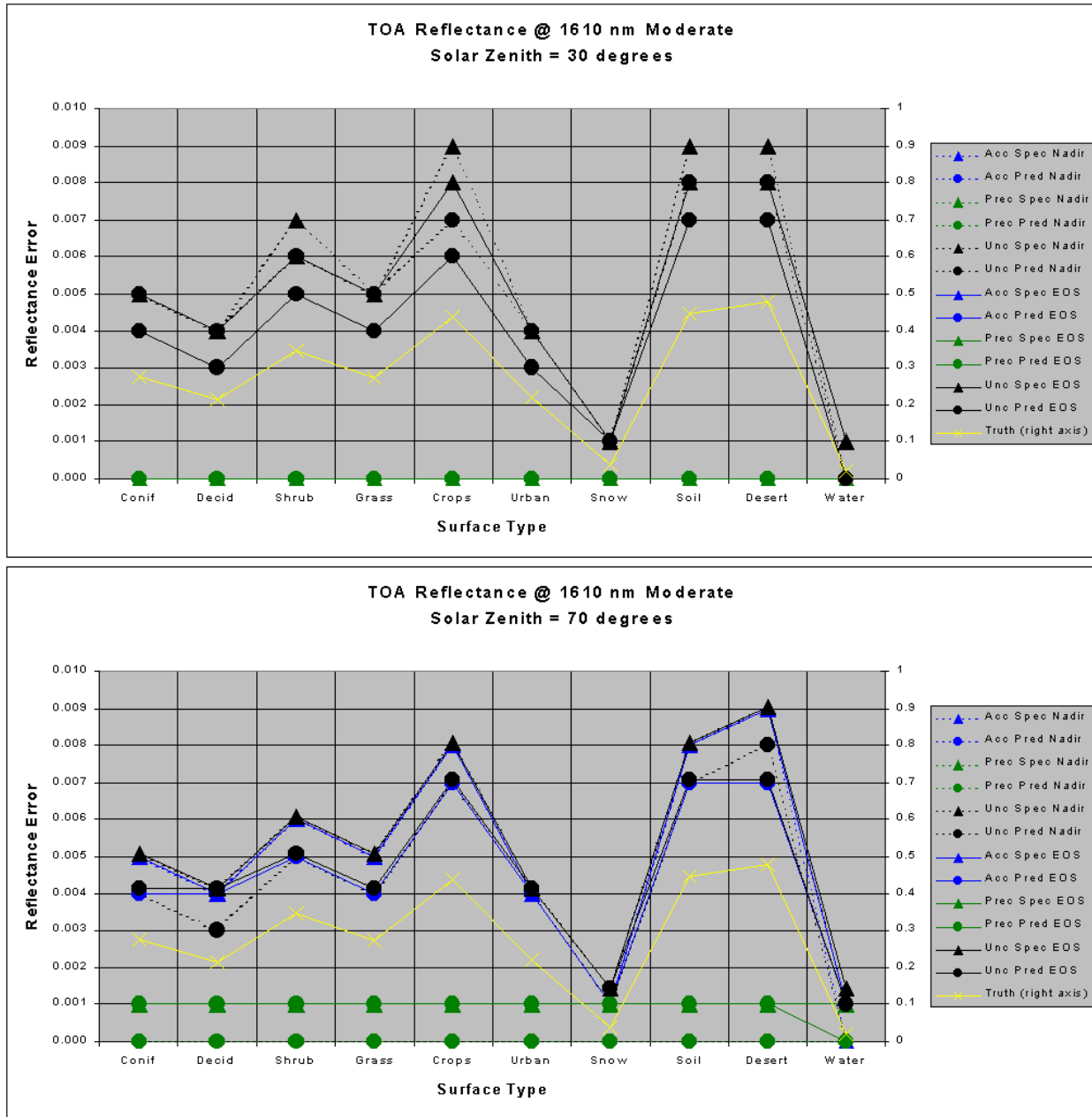


Figure 3.14 TOA reflectance errors at 1610 nm, for nadir and edge of scan, at solar zenith of 30 degrees (top) and 70 degrees (bottom), using both specified and predicted sensor performance as input.

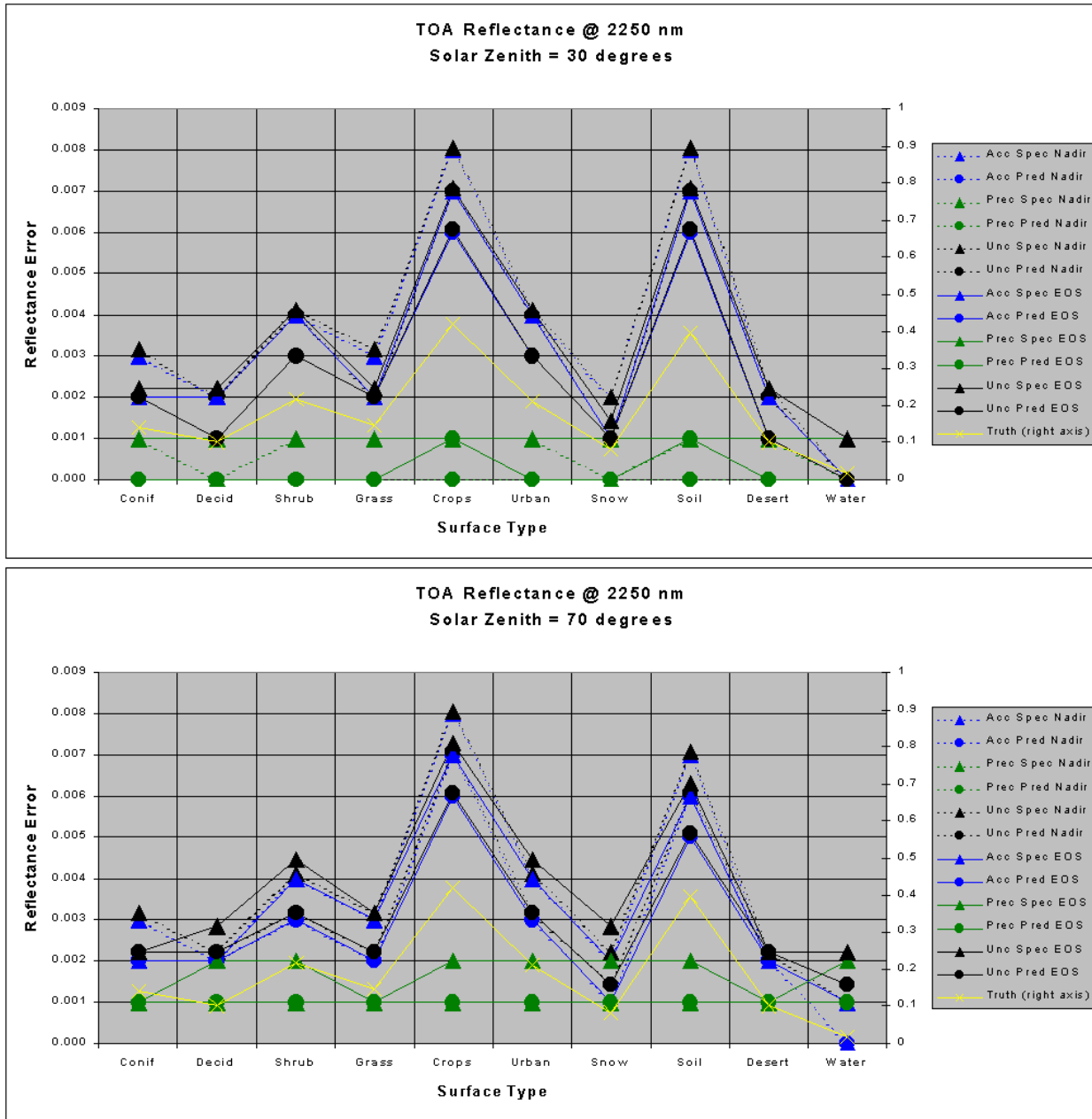


Figure 3.15 TOA reflectance errors at 2250 nm, for nadir and edge of scan, at solar zenith of 30 degrees (top) and 70 degrees (bottom), using both specified and predicted sensor performance as input.

3.4.3.6 BPSA Intrinsic Errors

The BPSA intrinsic error, which could also be called algorithmic or regression error, contains the effects of several items:

- 1) Atmospheric variability, including variations in aerosol type and optical thickness

- 2) Narrow to broadband conversion, including variations between surface types
- 3) Angular variability—variations in solar zenith, viewing zenith, and relative azimuth—including BRDF and atmospheric effects
- 4) Training error, or the inability of the algorithm to achieve perfect performance within its training data set
- 5) Non-uniqueness, or the difficulty in completely decoupling atmospheric and surface effects when a TOA reflectance field has multiple possible surface solutions

Of these errors, the fifth could semantically be absorbed into the first three for simplicity, the route chosen here. Training error can be brought to lower level by careful selection of a wide-ranging set of training data points. The training strategy for the BPSA will begin with comprehensive radiative transfer simulations, and that these will be phased out in favor of real measurements from MODIS, and eventually from VIIRS.

Simulations for snow at the edge of the VIIRS scan indicate that even under extreme geometry, the BPSA is still fairly faithful to its training set, as shown in Table 3.14. The uncertainty specification is exceeded slightly, as the algorithm is primarily targeting the center of the range of true albedos; this can be mitigated in the future with different approaches to training. For example, more training data can be generated for the edge bins to reduce the dominance of the center bin. Again, these simulations do not include realistic simulations of surface BRDF, however the training set does include a range of aerosol optical thickness from 0.1 to 0.3, in addition to four separate aerosol types (urban, rural, desert, and maritime), with solar zenith ranging over ten degrees and view zenith also ranging over ten degrees (extending, in fact, to slightly beyond the actual limit of the VIIRS scan angle). Forward scattering from 0 out to 45 degrees in relative azimuth was also implemented here.

Table 3.14. Results for the BPSA over snow, at the edge of the VIIRS scan.

Albedo Range	# Samples	Accuracy	Precision	Uncertainty
0.55-0.60	603	0.037	0.017	0.041
0.60-0.65	1175	0.001	0.018	0.018
0.65-0.70	870	0.035	0.016	0.038

The stick modeling data set presented in Section 3.4.3.5 was used to conduct an end-to-end, stratified performance summary for the BPSA, for both dark and bright surface types. The results are shown in Figure 3.16 and Figure 3.17, for accuracy and uncertainty, respectively. Accuracy is generally within the threshold requirement, and the fine HCS uncertainty requirement at nadir is also achievable for all surface types.

For an assessment of the overall performance of the MODIS approach, the reader is directed to Lucht *et al.* (2000). The initial results suggest this algorithm can meet the VIIRS specifications for dark surfaces.

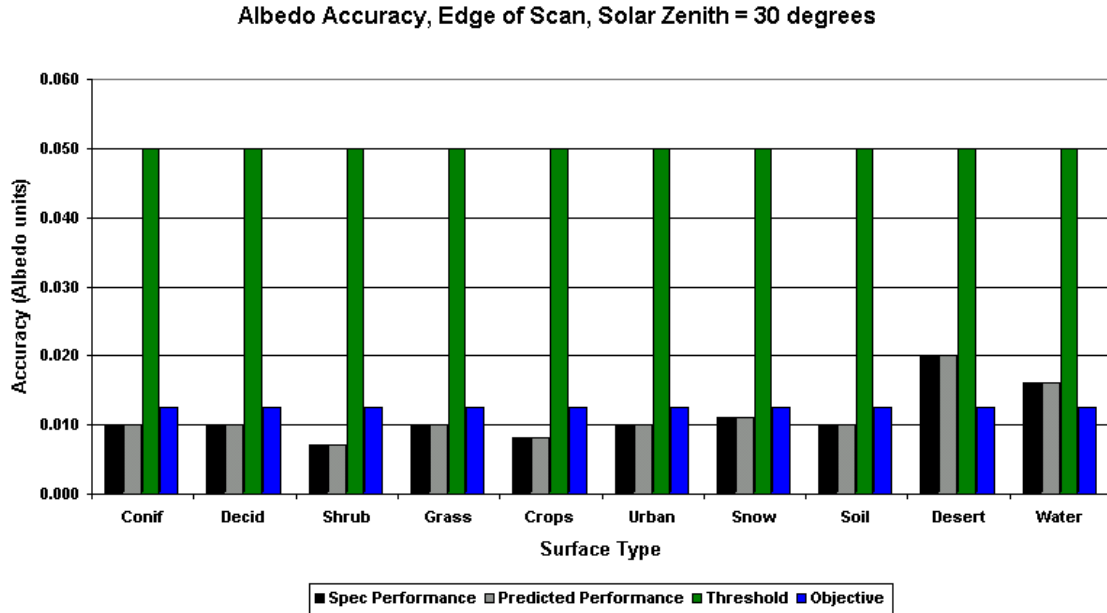


Figure 3.16 Albedo accuracy performance for the BPSA, spec and predicted, at edge of scan for a solar zenith of 30 degrees. Note negligible difference between spec and predicted sensor performance for calibration, assuming the algorithm is trained post-launch with real VIIRS data.

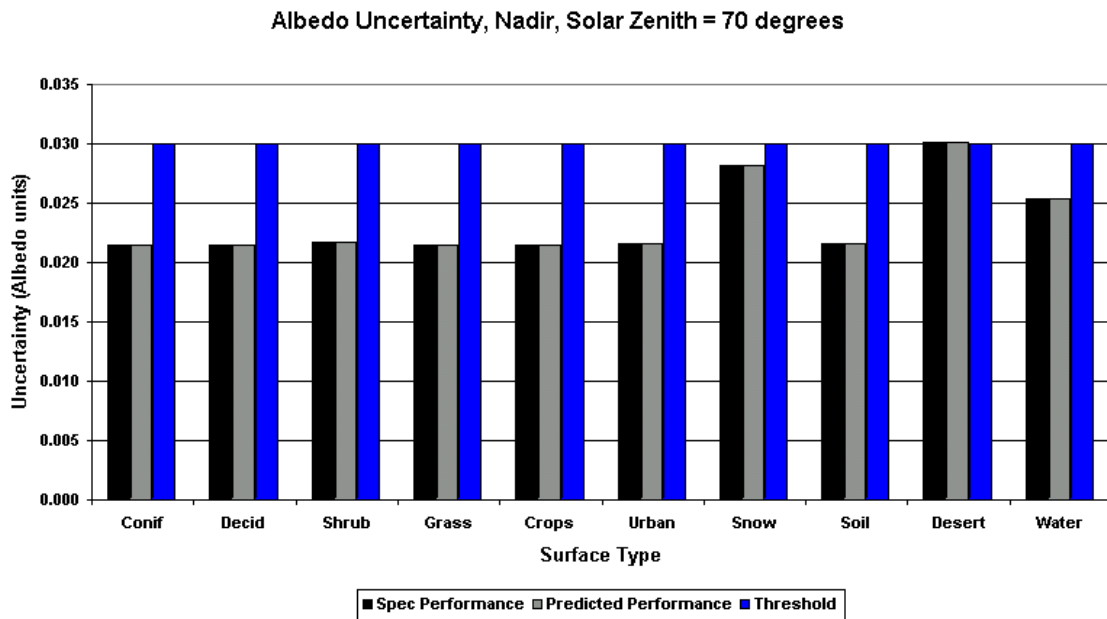


Figure 3.17 Albedo uncertainty performance for the BPSA, spec and predicted, at nadir for a solar zenith of 70 degrees. Nadir uncertainty requirement (fine product) is 0.03 threshold.

3.5. PRACTICAL CONSIDERATIONS

3.5.1. Numerical Computation Considerations

The VIIRS SRD (NPOESS IPO, 1998) states the following (Paragraph SRDV 3.2.1.5.4-1):

The scientific SDR and EDR algorithms delivered by the VIIRS contractor shall be convertible into operational code that is compatible with a 20 minute maximum processing time at either the DoD Centrals or DoD field terminals for the conversion of all pertinent RDRs into all required EDRs for the site or terminal, including those based wholly or in part on data from other sensor suites.

RDR here stands for Raw Data Record. This essentially means that any and all EDRs must be completely processed from VIIRS raw data, which include calibration and georeferencing information, within 20 minutes from the time the raw data are available. This requirement is a strong reminder that VIIRS is an operational instrument.

For the BPSA, the challenges posed by the SRD time requirement are minimal. The regression approach is merely a single equation at run time. Training is conducted offline. For the DPSA, our approach shifts most of the computational burden offline as well; the inversion procedure takes place once per day to generate the Gridded Surface Albedo IP. All that is required in real-time is a simple interpolation routine to bring the black sky and white sky albedo to the pixel level, followed by the application of simple empirically based formulae.

3.5.2. Programming and Procedural Considerations

Numerical computation load and complexity of operational code are typically rather well correlated. More intensive algorithms will generally be manifested in larger and more intricate source code. The code itself can have a significant impact on numerical computation load if it is not developed efficiently. The albedo algorithm is not expected to cause many problems in this regard. The simplicity of the real-time portion of the BPSA translates into only moderate amounts of code using basic mathematical routines. Storage of the regression coefficients should not present a problem; the Phase I version contained approximately 100 per angular bin, and the ability to replace the neural network with a simpler regression approach will reduce the required number of stored coefficients to a much smaller number that will apply to all cases. These numbers are small compared to the various lookup tables existing within the VIIRS system.

VIIRS Phase II efforts are largely software-focused, and the methodology for this development work is based on sound and proven principles, as discussed in the VIIRS Algorithm Software Development Plan [Y6635]. The present maturity of the VIIRS software is detailed in the VIIRS Algorithm Software Maturity Assessment document [Y6661]. The software designs relevant to Surface Albedo are summarized in the VIIRS Context Level Software Architecture [Y2469], Land Module Level Software Architecture [Y2474], Land Module Level Detailed Design [Y2483], and Surface Albedo Unit Level Detailed Design

[Y2483]. These designs will be tested at the system level as described in the most recent versions of the VIIRS Software Integration and Test Plan [Y3236], Algorithm Verification and Validation Plan [Y3237], and System Verification and Validation Plan [Y3270]. A summary of the ultimate strategy for operational application of the system of VIIRS algorithms is provided in the VIIRS Operations Concept document [Y2468]. The VIIRS Interface Control Document (ICD [Y2470]) provides more detail on the specifics of ancillary data requirements for Surface Albedo and other VIIRS products.

3.5.3. Configuration of Retrievals

The primary adjustable parameters for the retrieval of the albedo product are those that govern the overall stratification with respect to the expected quality of the output. These parameters have been merged into the generalized Land Quality Flag (LQF) structure, which is appended to the output of the Surface Reflectance IP. For more detail on the LQF output, the reader is directed to [Y2411].

3.5.4. Quality Assessment and Diagnostics

Again, the reader is directed to [Y2411] for a discussion of quality assessment regarding the LQF output. Some additional diagnostics will be required for the BPSA, to ensure the regression functions well over time. In fact, these analyses will provide an excellent means of monitoring the long-term stability of the sensor in the nine relevant bands listed in Table 2.1.

3.5.5. Exception Handling

The algorithm performance will be guaranteed to meet the system specifications [SS154650] only if the assumptions listed in Section 4.1 are valid and the limitations listed in Section 4.2 are not encountered. Missing data can be interpolated or assigned the most recently obtained value, however this is not currently planned for the VIIRS processing system. The LQF will specify whether a given pixel should be expected to meet the specifications for Surface Albedo.

3.6. RETRIEVAL SAMPLES

The algorithm described above has been tested using MODIS data. First, a set of 16-day MODIS daily gridded surface reflectance data is generated using the MODIS gridded Surface Reflectance data, the MODAGAGG data. This is done through regression equations that convert the MODIS reflectance bands (7 bands in total) into VIIRS bands (9 bands in total). Also, the MODIS MOD43B1 data are used to generate a VIIRS BRDF Archetypal data file. The same regression coefficients are used for converting the 7-band MODIS BRDF parameters into 9-band VIIRS BRDF parameters. The VIIRS BRDF data are then generated using the code that implements the algorithm described through sections from 3.3.2.1.1 to 3.2.2.1.7.

3.6.1. BRDF Retrieval

Figures 3.18 and 3.19 show the test results of VIIRS BRDF computation (using RMSE criterion) for the BRDF layer 1, the vegetated surface. The image area is in California, as is named the MODIS tile h08v05, in January 2004. Figure 3.18 gives quality control flags that indicate the area where full inversion (green and yellow), magnitude (red) inversion or historical BRDF (white) is resulted. In the figure, percentages for the area of full inversion, magnitude inversion and the historical BRDF data are very close. There are a few yellow-colored areas where the RMSE values defined in Equation (3.16) are higher than the threshold value (0.3).

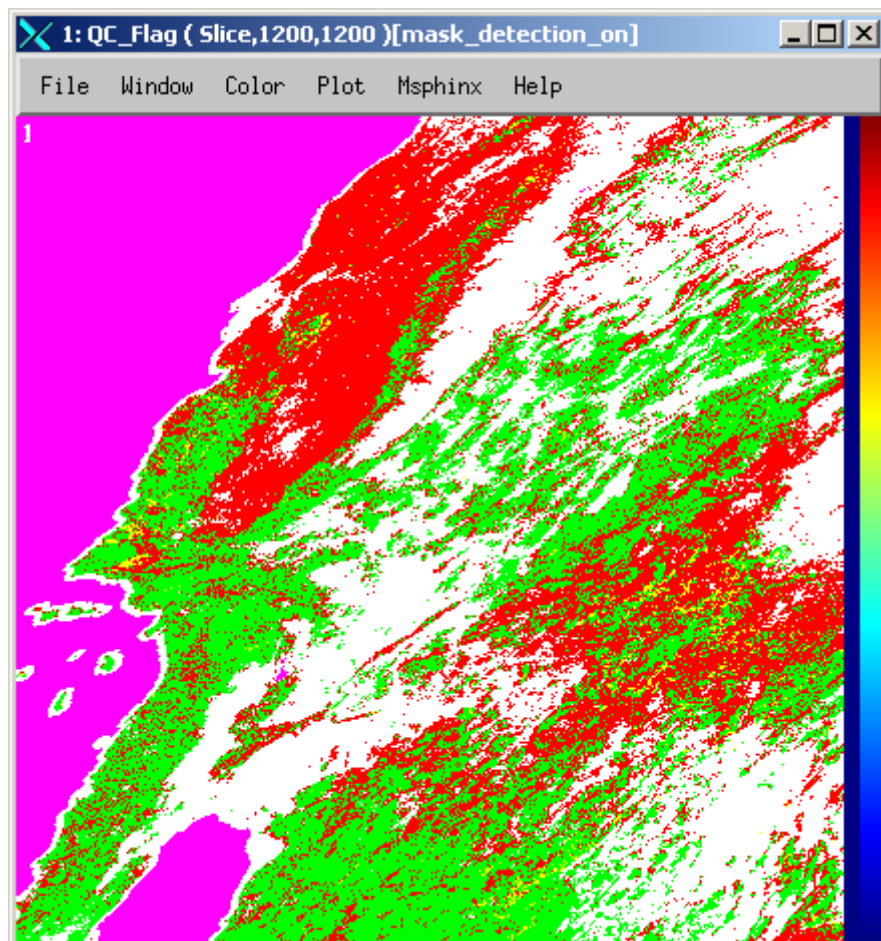


Figure 3.18 BRDF inversion results over the MODIS tile h08v05 for VIIRS DPSA (full inversion = green and yellow, magnitude inversion = red, history = white, fill value = magenta).

Figure 3.19 gives the model parameter patterns of f_0 for all the VIIRS 9 reflectance bands. It is expected that the patterns in all the 9 bands are almost the same since the same kernels are applied across the bands.

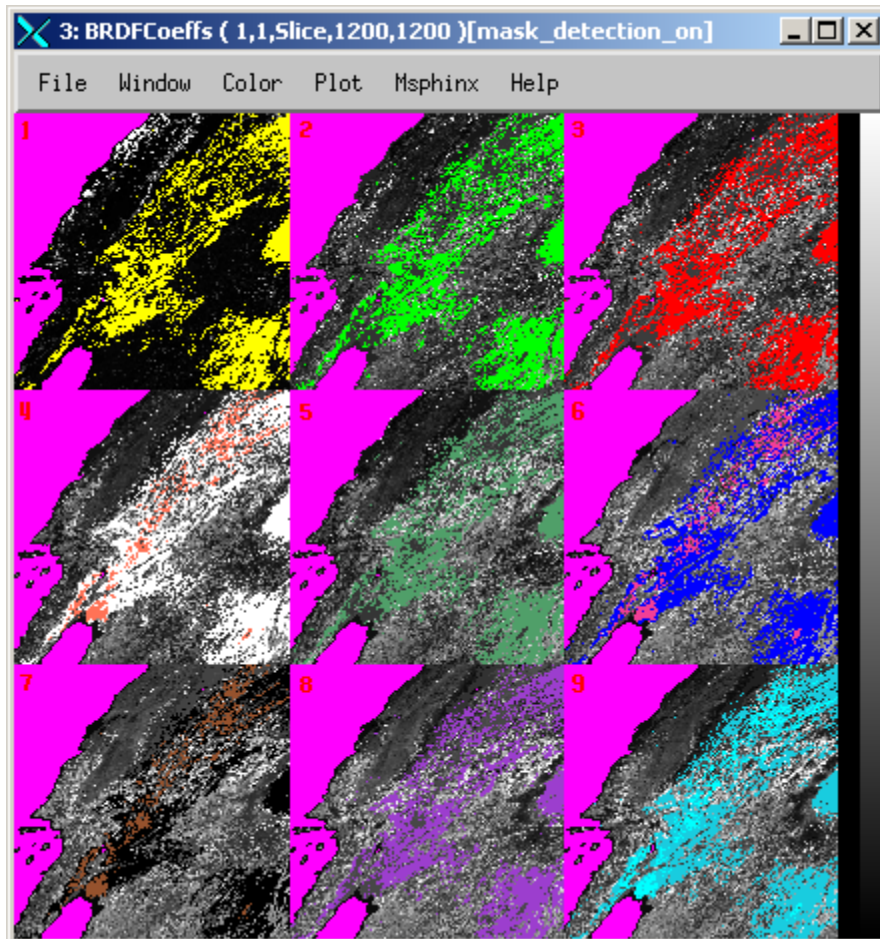


Figure 3.19 BRDF model parameter f0 over the MODIS tile h08v05 for VIIRS DPSA

3.6.2. Albedo Retrieval

Figure 3.20 gives the VIIRS DPSA retrieval results for a swath over Arizona. A test data set of the VIIRS input data and NCEP data (as listed in Tables 3.1) are used for the computation. At the time of writing this ATBD, no tools were available to convert Gridded BRDF data into Swath BRDF data. We have to use an artificially generated swath level BRDF data set for the test. It contains two sets of model parameter values. As a result, the DPSA histogram in Figure 3.21 has two sub-histogram structures, each representing one model parameters set. The dark green pattern at the bottom of the figure is because of the noise in the Aerosol Optical Thickness data. The exact same pattern is also seen in the AOT data (not shown here).

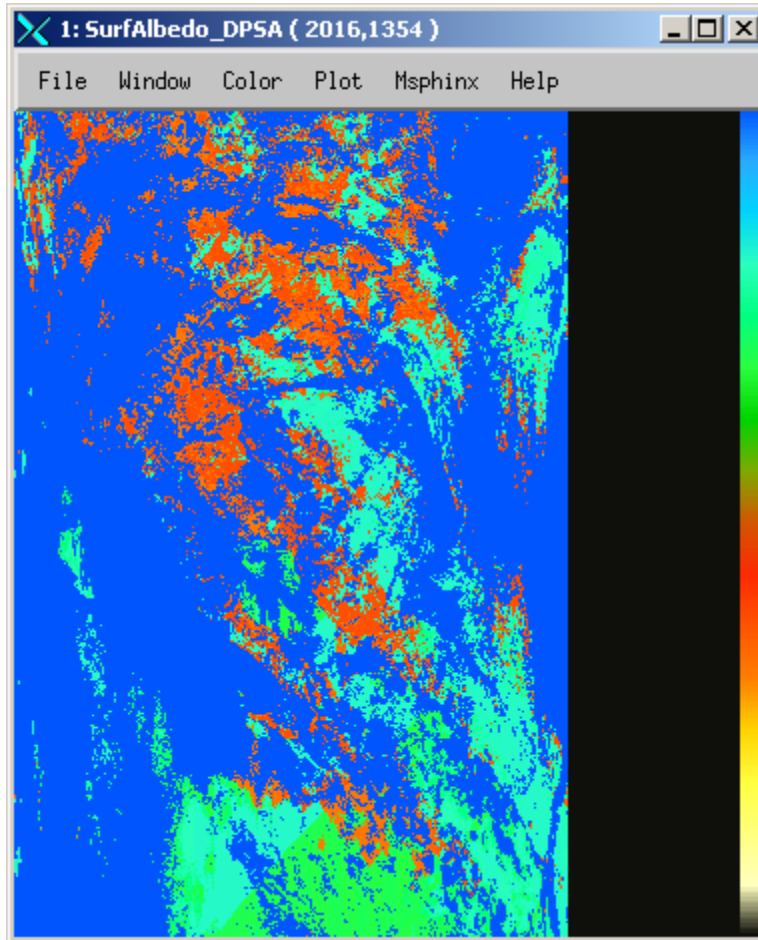


Figure 3.20 VIIRS DPSA retrieved using the test VIIRS input data and artificial BRDF data.

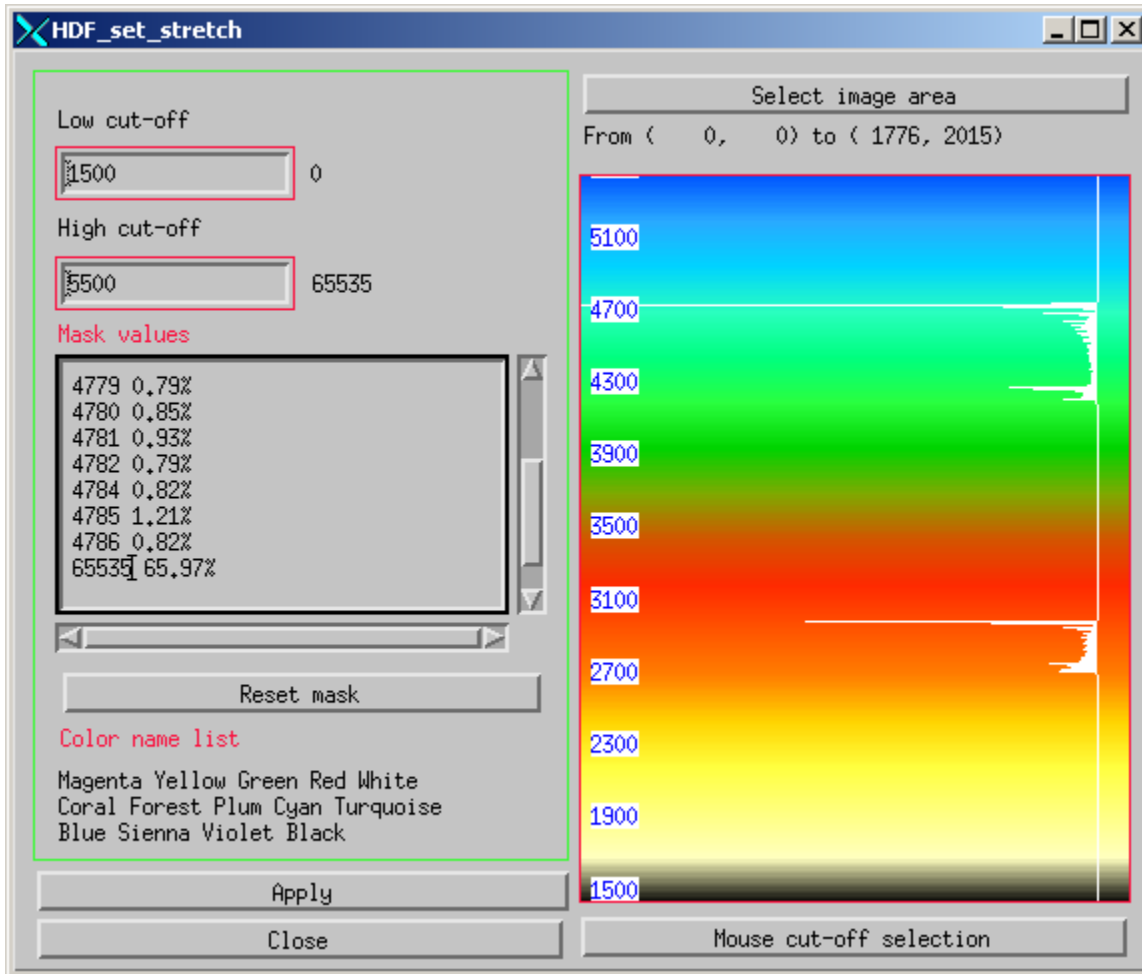


Figure 3.21 VIIRS DPSA histogram. The values are scaled by 10000.

Figure 3.22 gives the VIIRS BPSA retrieval results for the same swath (over Arizona). Again the test data set are used. Red area in the figure is the fill value area, meaning no Top Of Atmosphere (TOA) reflectance data available for those pixels or they are cloudy. Figure 3.23 gives the BPSA histogram. If the swath BRDF data are real and matched with all other VIIRS input data and NCEP data, we would expect comparable histogram distributions between the DPSA and BPSA. There should be at least an overlap in both the distributions since the BPSA in many areas should be close enough to the DPSA. It is very unfortunate that we are not able to have an “all matched input data set” for the test.

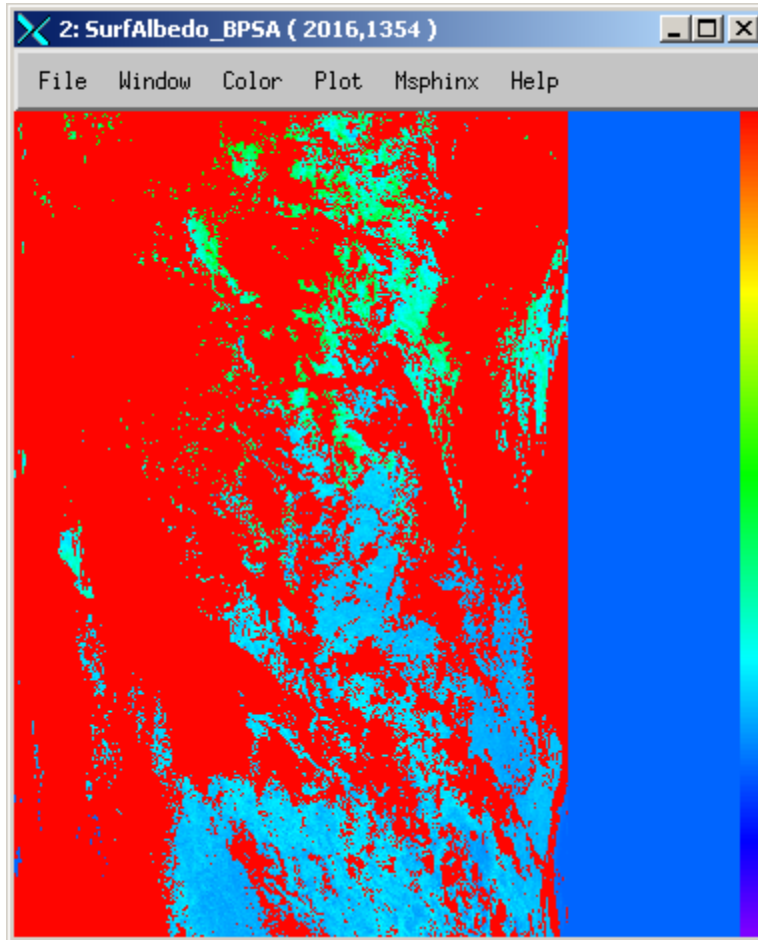


Figure 3.22 VIIRS BPSA retrieved using the test VIIRS input data

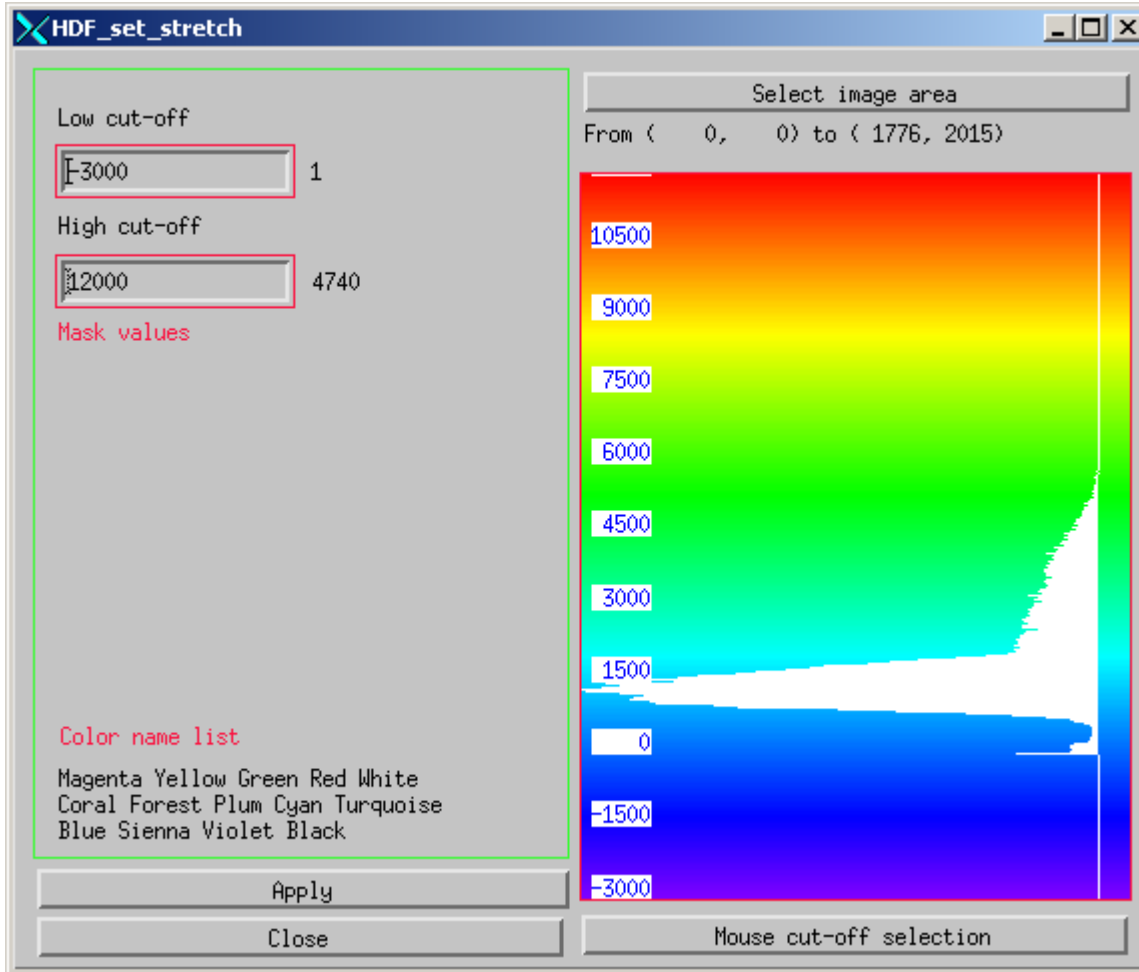


Figure 3.23 VIIRS BPSA histogram. The values are scaled by 10000.

3.6.3. Albedo Sensitivity

The algorithm sensitivities to aerosol optical thickness (AOT) and to the TOA reflectance are also tested. This is done by comparing new generated DPSA and BPSA, with changes of the input AOT and TOA reflectance values, to the original DPSA and BPSA. The increase in AOT value is 0.1 over all the pixels, while it is 2 percent in TOA reflectance values.

Figure 3.24 gives the histogram statistics of the DPSA difference. It is interesting to see that the histogram has two peaks at 0.3 and 1.6, respectively, corresponding to the two sub-histogram structures of the DPSA in Figure 3.21. Recall that the input BRDF data set results the DPSA histogram structure, the DPSA difference in Figure 3.24 is dominated by the BRDF structure rather than by the AOT uncertainty. The maximum difference in this case is less than 2.5 %. Since 0.1 uncertainty in AOT value is a requirement for the NPOESS aerosol algorithm, the 2.5% difference in DPSA resulting from the AOT uncertainty leaves little, if any, margin for other error sources in terms of accuracy. Therefore the accuracy requirement will possibly not be met operationally.

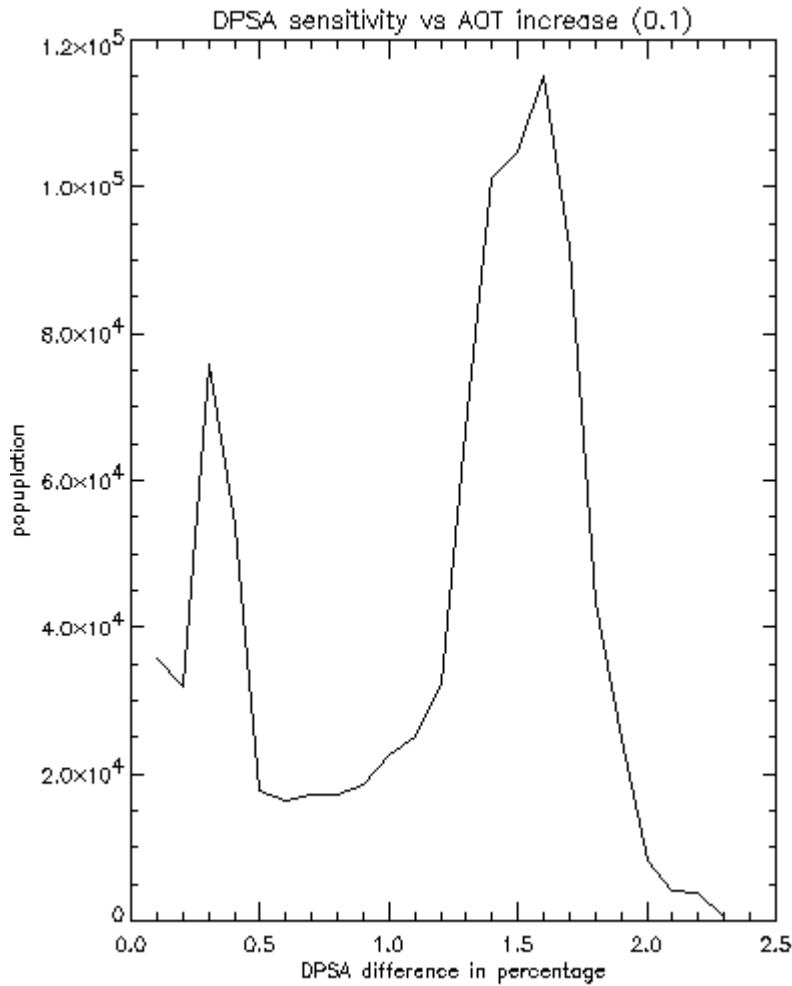


Figure 3.24 Histogram of the DPSA difference if AOT increases 0.1

In Figure 3.25 the histogram statistics of the BPSA difference is displayed. It shows that the BPSA uncertainty is between 2% and 4% when the TOA reflectance uncertainty is 2%. The 2 - 4% uncertainty in BPSA resulting when the TOA reflectance uncertainty exceeds its required accuracy leaves little, if any, margin for other error sources in terms of accuracy. Therefore the Surface Albedo accuracy requirement will possibly not be met operationally.

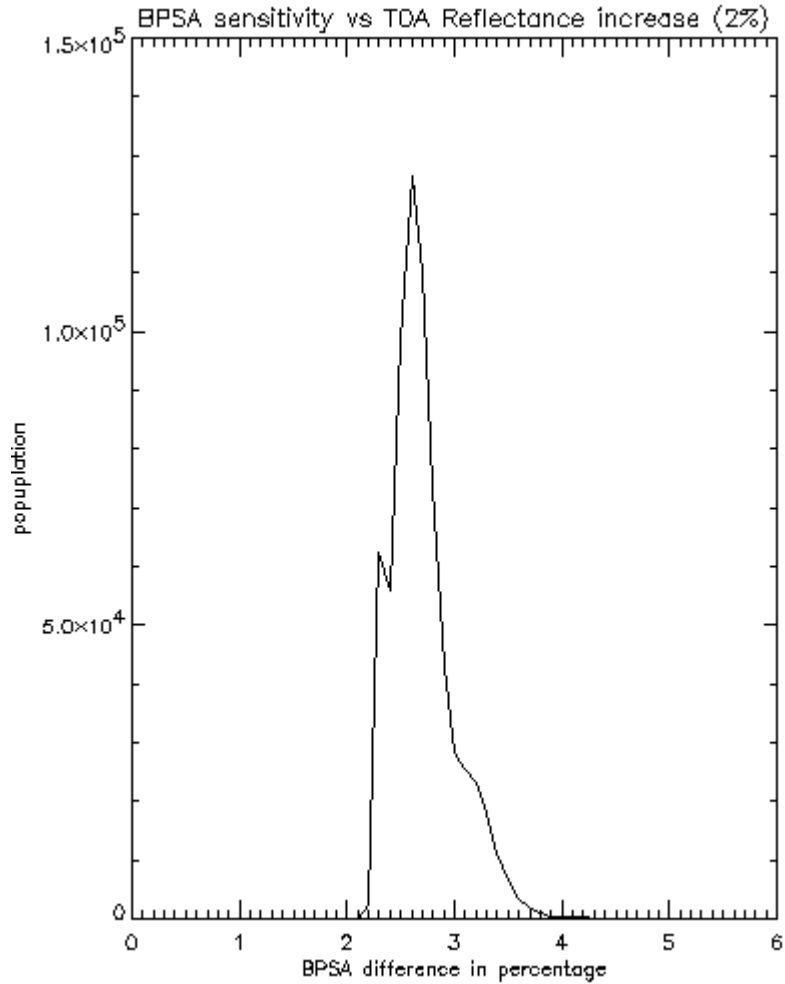


Figure 3.25 Histogram of the BPSA difference if TOA reflectance increases 2%.

The above BPSA data is derived assuming a Tropospheric aerosol model. Remember that the regression coefficients for the BPSA algorithm are aerosol model dependent it is worth to check how much the error would be if the aerosol model information is incorrect. Figure 3.26 shows the histogram of the BPSA difference if the aerosol model information is changed from the Tropospheric model to the Rural model. It shows that, in this particular case, the difference is little bit less than the difference due to the TOA uncertainty.

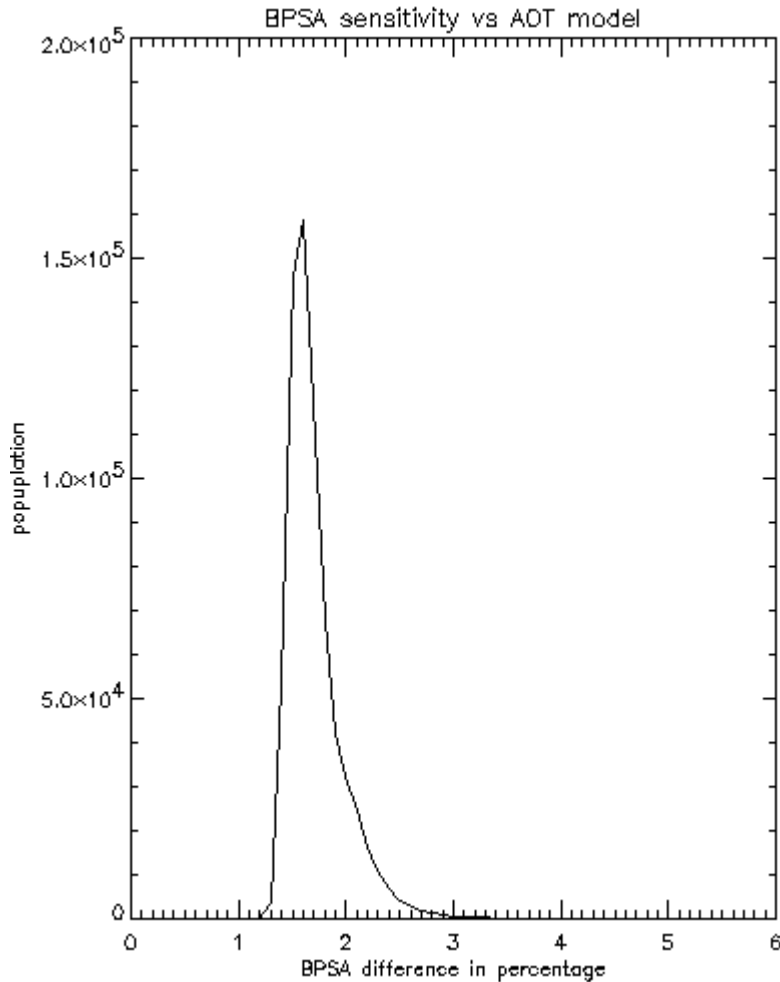


Figure 3.26 Histogram of the BPSA difference due to AOT model information error.

3.7. VALIDATION

The following provides a synopsis of the Surface Albedo algorithm validation plan, which is detailed in VIIRS document Y3237. For any EDR, we define the following terms.

Definition: *Product validation* constitutes a comparison between:

- (a) Geophysical products retrieved by applying VIIRS-EDR algorithms to surface or tropospheric-leaving radiances measured by a VIIRS simulator instrument, or top-of-atmosphere (TOA) radiances measured by VIIRS, with
- (b) Geophysical products retrieved from downwelling sky and solar radiation measured at the surface, together with conventional retrieval algorithms based on such

measurements. Analysis of systematic and random errors in each pathway (e.g., downward-looking and upward-looking) is included.

Definition: A *field experiment* is a comparison of two geophysical parameter retrievals based on independent measurements.

Definition: A *field campaign* is an activity that involves conducting one or more field experiments.

The AVP describes how, in the pre-launch period, an output is generated that accurately represents (in a scientific sense) what it claims. Secondly, the plan describes how each data product, in the post-launch period, can be shown to accurately represent the corresponding radiometric or environmental (“geophysical”) parameters. The plan contains the following elements:

- Description of validation objectives.
- Specification of VIIRS products that can be validated by simple ground-based or aircraft-based procedures.
- Specification of conventional methods for measuring each product from a ground perspective.
- Definition of algorithm development needs, beyond that existing and available.
- Definition of instrumentation needs, uses, calibration, and intercomparison procedures, including:
 - Ground-based for applicable atmosphere, surface, and TOA/cloud retrievals
 - Aircraft VIIRS simulator and supporting instruments (e.g., aircraft sunphotometry)
 - Aircraft measurements (e.g., in-situ aerosol sampling)
 - Spacecraft candidates with view capabilities that bear upon comparisons with VIIRS.
- Specification of test sites for both algorithm validation (pre-launch) and product verification (post-launch).
- Description of the nature of field experiments to achieve simultaneous ground-based and aircraft simulator (pre-launch) or VIIRS (post-launch) observations, including required experimental conditions, deployment of ground-based resources, aircraft flight line configurations, and timing of overpasses to simulate VIIRS observing conditions.
- Description of post-experiment data reduction and error analysis procedures.
- Plans for archival and publication of validation/verification results.

The AVP is designed to accomplish the following objectives in the pre-launch and post-launch time frames.

AVP pre-launch objectives:

- Validate the DPSA and BPSA using simulated data
- Procure and adapt/modify essential field instruments for solar, sky and ground-reflected radiation measurements to implement retrieval algorithms
- Organize field campaigns at selected test sites, encompassing essential parts of the different surface conditions on global scale
- Demonstrate the ability to make field measurements of radiometric quantities
- Demonstrate the ability to derive both the spectral and the broadband albedo from ground measurements
- Specifically evaluate the sensitivity of VIIRS airborne simulator and field instruments to validate VIIRS EDR retrieval algorithms
- Develop new software to analyze data for VIIRS needs (e.g., software for PARABOLA or any other ground-based instrument-measured data)
- Cooperate and discuss with the calibration team the results of the measurements/simulations/calibrations found for the VIIRS simulator instruments as well as the VIIRS sensor.

AVP post-launch objectives:

- Validate the DPSA and BPSA using satellite-derived data
- Continue to validate the DPSA and BPSA as needed
- Discuss the measurements delivered by the VIIRS sensor with the calibration team
- Calibrate the VIIRS simulator instruments in constant time intervals to uncover instrument degradation and to keep track of possible changes in performance of the VIIRS sensor
- Conduct field experiments on the designated test sites coordinated with underflights of airborne instruments and a VIIRS overpass
- Compare/analyze of VIIRS-derived albedo and the albedo derived from other satellite systems.

The following guidelines have been applied for the selection of the NPOESS VIIRS test beds:

- Co-locate algorithm and product validation experiments (where possible) with other major surface and/or atmospheric experiments, to take advantage of resources and infrastructure present, and make the sharing of scientific data possible.

- Logistic convenience for surface and aircraft observations, to minimize field access problems, as well as aircraft flight hour costs. Sites may be occupied several times over a period of years. Sites in North America and the continental United States (plus adjacent ocean waters) have thus been favored whenever possible, except where significant advantages may be obtained by joining forces with other groups elsewhere.
- Availability of records of seasonal conditions to optimize chances for choices of clear sky opportunities for aerosol and surface reflectance studies.

4.0 ASSUMPTIONS AND LIMITATIONS

4.1 ASSUMPTIONS

The following assumptions apply to the albedo retrieval algorithms described in this document:

1. Specifications on sensor performance as described in [PS154650].
2. The existence of an at-launch database for generating the Gridded Surface Albedo IP and the Gridded Daily Surface Reflectance IP, until these VIIRS products have phased completely in.
3. National and international validation networks that can be tapped for the testing of both the DPSA and BPSA before the launch of NPP, and again before the first launch of NPOESS.

4.2 LIMITATIONS

The following limitations apply to the albedo retrieval algorithm described in this document:

1. The assumption of a plan-parallel scattering medium must be valid for the BPSA. Thus, the solar and observer zenith angles are constrained to values less than 70° for specification quality (retrievals conducted out to 85°). Similar angular limits apply to the DPSA.
2. The algorithm is not applicable to ocean surface.
3. Retrievals will be questionable in regions with very heavy aerosol loading, such as associated with local volcanic eruptions, fires, or sandstorms.

5.0 REFERENCES

- Andrieu, B., F. Baret, S. Jacquemoud, T. Malthus, and M. Steven (1997). Evaluation of an Improved Version of SAIL Model for Simulating Bidirectional Reflectance of Sugar Beet Canopies. *Rem. Sens. Env.*, 60:247-257.
- Bicheron, P., and M. Leroy (2000). Bidirectional reflectance distribution function signatures of major biomes observed from space. *J. Geophys. Res.*, D105, 26669-26681.
- Charney, J., W.J. Quirk, S. Chow, and J. Kornfield (1977). A comparative study of the effects of albedo change on droughts in Semi-arid regions, *J. Atmos. Sci.*, 34, 1366.
- Chase, T.N., R.A. Pielke, T.G.F. Kittel, R. Nemani, S.R. Running (1996). Sensitivity of a GCM to global changes in LAI. *J. Geophys. Research-Atmospheres*, 101 (D3), 7393-7408.
- Chen, T., and G. Ohring (1984). On the relationship between clear-sky planetary and surface albedos. *J. Atmos. Sci.*, 41, 156-158.
- Culf, A.D., G. Fisch, and M. G. Hodnett, (1995). The albedo of Amazonian forest and ranchland. *J. Climate*, 8 (6), 1544-54.
- Dickinson, R.E. (1983). Land surface processes and climate-surface albedos and energy. *Adv. Geophys.*, 25:305-353.
- Dickinson, R.E. (1995). Land processes in climate models, *Remote Sens. Environ.*, 51, 27--38.
- Gao, F, Li X., Strahler A.H. and Schaaf C.B. (2000), Comparison and validation of the new Li-Transit kernel, *Remote Sensing Review*, Vol 19, pp 205-224.
- Gao F., Schaaf C. B., Strahler A.H. and Lucht W., (2001), *Using a multi-kernel least variance approach to retrieve and evaluate albedo from limited bi-directional measurements*, *Remote sensing of Environment*, Vol 76, pp 57-66.
- Garrat, J.R. (1993). Sensitivity of climate simulations to land surface and atmospheric boundary layer treatments – a review. *J. Climate*, 6, 419-449.
- Gordon, H. R., D. K. Clark, J. W. Brown, O. B. Brown, R. H. Evans, W. W. Broenkow, (1983). Phytoplankton pigment concentration in the Middle Atlantic Bight: Comparison of ship determinations and Coastal Zone Color Scanner measurements. *Appl. Opt.*, 22, pp. 3929.
- Graedel, T.E. and P.J. Crutzen (1994). *Chemie der Atmosphäre*, Spektrum Akademischer Verlag GmbH, Heidelberg, Berlin, Oxford, ISBN 3-86025-204-6.

- Han, W. (1996). Remote Sensing of Surface Albedo and Cloud Properties in the Arctic from AVHRR Measurements, Ph.D. Thesis, Geophysical Institute, University of Alaska, Fairbanks, Alaska 99775.
- Henderson-Sellers, A. and Pitman, A.J. (1992). Land-surface schemes for future climate models: Specification, aggregation, and heterogeneity. *J. Geophys. Res.*, 97:2687-2696.
- Henderson-Sellers, A., Z.-L. Zhang, and R. E. Dickinson (1993). The project for intercomparison of land-surface parameterization schemes, *Bull. Am. Meteorol. Soc.*, 74, 1335-1349.
- Hucks, J.C. (1998). VIIRS Testbed Sensor Modeling Efforts, Phase I. Raytheon Systems Company Internal Memorandum Y1629.
- Jupp, D.L.B., and A.H. Strahler (1991). A hotspot model for leaf canopies. *Rem. Sens. Environ.*, 38:193-210.
- Kimes, D.S., and P.J. Sellers (1985). Inferring hemispherical reflectance of the Earth's surface for global energy budgets from remotely sensed nadir or directional radiance values. *Rem. Sens. Environ.*, 18, pp 205.
- Koepke, P, and K.T. Kriebel (1987). Improvements in the shortwave cloud-free radiation budget accuracy, Part I: Numerical study including surface anisotropy. *J. Clim. Appl. Meteorol.*, 26, 374-395.
- Larsen, N. Personal communication, August 1997.
- Lean, J., and P.R. Rowntree (1993). A GCM simulation of the impact of Amazonia deforestation on climate using an improved canopy representation. *Quart. J. Roy. Meteor. Soc.*, 119, 509-530.
- Lee, T.Y., and Y.J. Kaufman (1986). Non-Lambertian Effects on Remote Sensing of Surface Reflectance and Vegetation Index. *IEEE Trans. Geosci. Rem. Sens.*, GE-24, 699-708.
- Leroy, M., J. L. Deuze, F. M. Breon, O. Hautecoeur, M. Herman, J. C. Buriez, D. Tanre, S. Bouffies, P. Chazette, and J.-L. Roujean (1997). Retrieval of atmospheric properties and surface bidirectional reflectances over land from POLDER/ADEOS, *J. Geophys. Res.*, 102, 17023-17037.
- Lewis, P., (1995), The utility of kernel-driven BRDF models in global BRDF and albedo studies, in Proc. Int. Geosci. Rem. Sens. Symp. '95, Florence, Italy, pp. 1186-1187.
- Lewis, P., and M. J. Barnsley (1994). Influence of the sky radiance distribution on various formulations of the earth surface albedo, Proc. Conf. Phys. Meas. Sign. Remote Sens., Val d'Isere, France, 707-715.

- Li, Z, and L. Garand (1994). Estimation of surface albedo from space: A parameterization for global application. *J. Geophys. Res.*, 99, 8335-8350.
- Li, X. , and A. H. Strahler (1986), Geometrical-optical reflectance modeling of a conifer forest canopy, *IEEE Trans. Geosc. Rem. Sens.*, 24, 906-919.
- Li, X., and A. H. Strahler (1992). Geometric-optical bi-directional reflectance modeling of the discrete crown vegetation canopy: Effect of crown shape and mutual shadowing, *IEEE Trans. Geosci. Remote Sens.*, 30, 276-292.
- Liang, S., and A.H. Strahler (1993). Calculation of the Angular Radiance Distribution for a Coupled Atmosphere and Canopy. *IEEE Trans. Geosci. Rem. Sens.*, GE-31, 491-502.
- Liang, S., A.H. Strahler, and C. Walthall (1999). Retrieval of land surface albedo from satellite observations: a simulation study. *Journal of Applied Meteorology*, **38**, 712-725.
- Liang, S. (2003). A direct algorithm for estimating land surface broadband albedos from MODIS imagery. *IEEE Transactions on Geosciences and Remote Sensing*, **41**, 136-145.
- Lofgren, B. M. (1995). Surface albedo-climate feedback simulated using two-way coupling, *J. Climate*, 8, 2543-2562.
- Lucht, W., C.B. Schaaf, and A.H. Strahler (2000). An Algorithm for the retrieval of albedo from space using semi empirical BRDF models, *IEEE Trans. Geosci., Remote Sens.*, **38**, 977-998.
- Lucht, W., and J. -L., Roujean, (2000), Considerations in the parametric modeling of BRDF and albedo from multiangle satellite sensor observations, *Rem. Sens. Rev.*, **18**, 343-380.
- Martonchik, J.V., and D.J. Diner (1992). Retrieval of aerosol optical properties from multi-angle satellite imagery. *IEEE Trans. Geosci. Rem. Sens.*, **GE-30**, pp. 223.
- Matthews, E. (1983). Global vegetation and land use: New high resolution data bases for climate studies. *J. Clim. Appl. Meteorol.*, **22**, 474-487.
- Mintz, Y. (1984). *The sensitivity of numerically simulated climates to land-surface conditions*, The Global Climate, edited by J. Houghton, pp. 79-105, Cambridge University Press, New York.
- Nemani, R.R. ., S. W. Running, R. A. Pielke, T. N. Chase, (1996). Global vegetation cover changes from coarse resolution satellite data. *J. Geophys. Research-Atmospheres*, **101 (D3)**, 7157-7162.

- Nilson, T., and A. Kuusk (1989). A Reflectance Model for the Homogeneous Plant Canopy and Its Inversion. *Rem. Sens. Env.*, **27**,157-167.
- NPOESS IPO (1998). Visible/Infrared Imager/Radiometer Suite (VIIRS) Sensor Requirements Document (SRD). Prepared by Associate Directorate for Acquisition, NPOESS Integrated Program Office, Revision 1.
- Pinker, R.T. (1985). Determination of surface albedo from satellite. *Adv. Space Res.*, 5, 333-343.
- Pinty, B., and M.M. Verstraete (1991). Extracting information on surface properties from bidirectional reflectance measurements. *J. Geophys. Res.*, **96**, pp. 2865.
- Planet, W.G. (ed.), (1988). Data extraction and calibration of TIROS-N/NOAA radiometers. NOAA Technical Memorandum NESS 107 – Rev. 1, Oct. 1988. 130 pp.
- Press, W.H., Flannery B.P., Teukolsky S.A., Vetterling W.T., (1986), Numerical Recipes in C The art of Scientific Computing, Cambridge Press, New York.
- Qi, J., M.S. Moran, F. Cabot, and G. Dedieu (1995). Normalization of Sun/View Angle Effects Using Spectral Albedo-Based Vegetation Indices. *Rem. Sens. Env.*, **52**,207-217.
- Ross, J. K. (1981). *The Radiation Regime and Architecture of Plant Stands*, Dr. W. Junk, Norwell, Mass., 392 pp.
- Ross, J., and A. Marshak (1989). The Influence of Leaf Orientation and the Specular Component of Leaf Reflectance on the Canopy Bidirectional Reflectance. *Rem. Sens. Env.*, **27**, 251-260.
- Roujean, J.-L. M. Leroy, and P. Y. Deschamps (1992). A bi-directional reflectance model of the Earth's surface for the correction of remote sensing data, *J. Geophys. Res.*, **97**, 20455-20468.
- Roujean, J. –L., M. Leroy, and P. –Y. Deschamps, (1992), A bidirectional reflectance model of the Earth's surface for the correction of remote sensing data, *J. Geophys. Res.*, **97(D18)**, 20,445-20,468.
- Running, S. (1990). Estimating terrestrial primary productivity by combining remote sensing and ecosystem simulation, Remote sensing of Biosphere Functioning, edited by R. Hobbs and H. Mooney (New York: Springer-Verlag), pp.65-86.
- Running, S. W., C. O. Justice, V. Salomonson, D. Hall, J. Barker, Y. J. Kaufman, A. H. Strahler, A. R. Huete, J. –P. Muller, V.Vanderbilt, Z. –M. Wan, P. Teillet, D. Carnegie, (1994). Terrestrial remote sensing science and algorithms planned for EOS/MODIS. *Int. J. Rem. Sens.*, **15(17)**, 3587-3620.

- Saunders, R.W , (1990). The determination of broadband surface albedo from AVHRR visible and near-infrared radiances. *Int. J. Remote Sensing*, **11(1)**, 49-67.
- Schaaf, C.B., and A.H. Strahler (1993). Solar Zenith Angle Effects on Forest Canopy Hemispherical Reflectances Calculated with a Geometric-Optical Bidirectional Reflectance Model. *IEEE Trans. Geosci. Rem. Sens.*, **GE-31**, 921-927.
- Schaaf, C. B., F. Gao, A.H Strahler, W. Lucht, X. Li, T. Tsang, N. Strugnell, X. Zhang, Y. Jin, J.-P. Muller, P. Lewis, M. Barnsley, P. Hobson, M. Disney, G. Roberts, M. Dunderdale, C. Doll, R. d'Entremont, B. Hu, S. Liang, and J. Privette (2002). First Operational BRDF, Albedo, and Nadir Reflectance Products from MODIS, *Rem. Sens. Environ.* , **83**, pp.135-148.
- Strahler A.H., Lucht W., Schaaf C.B., Tsang T., Gao F., Li X., Muller J.P., Lewis P. and Barnsley M.J.,(1996), MODIS BRDF/Albedo Product: Algorithm Theoretical Basis Document Version 5.0, available from http://modis.gsfc.nasa.gov/data/atbd/atbd_mod09.pdf
- Sellers, P.J., S.O. Los, C.J. Tucker, C.O. Justice, D.A. Dazlich, G.J. Collatz, and D.A. Randall , (1994). A global 1 by 1 NDVI data set for climate studies. Part 2: The generation of global fields of terrestrial biophysical parameters from the NDVI. *Int. J. Rem. Sens.*, **15 (17)**, 3319-46.
- Sellers, P.J., D.R. Randall, G.J. Collatz, J.A. Berry, C.B. Field, D.A. Dazlich, and G.D. Collelo , (1996). A Revised Land Surface Parameterization (SiB2) for Atmospheric GCMs. Part I: Model Formulation. *J. Climate*, **9**,676-705.
- Vermote, E. F., D. Tanre, J. L. Deuze, M. Herman, and J. J. Morcrett, (1997), Second simulation of the satellite signal in the solar spectrum (6S): an overview, *IEEE Trans. Geosc. Rem. Sens.*, **35**, 675-686.
- Vermote, E., and A. Vermeulen (1999). MODIS Spectral Reflectances ATBD (ATBD-MOD-09), <http://eospso.gsfc.nasa.gov/atbd/modistables.html>.
- Vogt, P. (1997). Retrieval of the LAI and the FAPAR from bidirectional reflectance factors at the top of the canopy (in German), Ph.D.-thesis, ISSN 0939-2963, ISRN DLR-FB--97-25.
- Wanner, W., X. Li, and A. H. Strahler (1995). On the derivation of kernels for kernel-driven models of bidirectional reflectance, *J. Geophys. Res.*, **100**, 21077-21090.
- Wanner, W., A. H. Strahler, B. Hu, P. Lewis, J.-P. Muller, X. Li, C. L. Barker Schaaf, and M. J. Barnsley (1997). Global retrieval of bidirectional reflectance and albedo over land from EOS MODIS and MISR data: theory and algorithm, *J. Geophys. Res.*, **102**, 17143-17162.
- Wilson, M.F., and A. Henderson-Sellers (1985). A Global Archive of Land Cover and Soil Data for Use in General Circulation Models. *J. Climatology*, **5**, 119-143.

APPENDIX A

VIIRS NARROWBAND TO BROADBAND LAND SURFACE ALBEDO CONVERSION

Converting narrowband albedos to broadband albedo has been a research issue in remote sensing for a long time, since most sensors suitable for albedo mapping are outfitted with narrow spectral bands (Liang, 2001; 2003a). The broadband albedo mainly depends on surface reflectance spectra, but is also affected by the atmospheric conditions. The main objective of this study is to predict average surface shortwave broadband albedo, under general atmospheric conditions, using VIIRS narrowband albedos.

All previous studies on developing conversion formulas were based on either field measurements of certain surface types or model simulations. It is impossible to develop a universal formula only based on ground measurements because it is so expensive to collect field data sets extensively over different atmospheric and surface conditions. Model simulation is a better approach to develop universal conversion formulae, and ground measurements are certainly valuable for validation. The earlier studies using model simulations consider only a small set of atmosphere and surface conditions. Liang (Liang, 2001) extended it by taking into account comprehensive conditions for a variety of sensors, and the validation results using ground measurements verified that the resulting formulae are very accurate (Liang *et al.*, 2003b). The same algorithm is employed in this study, which is briefly described in the section 3. Section 2 discusses the characterization of VIIRS sensor. The resulting formulae and validation results are presented in Section 4. A short summary is presented in the last section.

The conversion has two steps. The first step is to conduct extensive radiative transfer simulations using the Santa Barbara DIScrete-Ordinate-method Radiative Transfer (DISORT) Atmospheric Radiative Transfer (SBDART) code (Ricchiuzzi *et al.* 1998). The second step is to perform multivariate regression analysis.

SBDART, a free software, has a nice user interface. The key element of the radiative transfer simulation is the inclusion of representative surface reflectance spectra. We employed 279 surface reflectance spectra in this study, including soil (43), vegetation canopy (115), water (13), wetland and beach sand (4), snow and frost (50), urban (26), road (15), rock (4), and other cover types (9). Each has different wavelength dependences and magnitudes, from coastal water (low albedos) to snow and frost (high visible albedos). Eleven atmospheric visibility values (2, 5, 10, 15, 20, 25, 30, 50, 70, 100, and 150km) were used for different aerosol loadings, and five atmospheric profiles of MODTRAN defaults (tropical, mid-latitude winter, sub-arctic summer, sub-arctic winter and US62) that also represent different water vapor and other gaseous amounts and profiles were utilized. A range of 9 solar zenith angles was simulated from 0° to 80° at 10° increments. SBDART was

run at 231 spectral ranges with the increased wavelength increment from 0.0025 μm at the shortest to 0.025 μm at the longest.

In the second step, a linear regression analysis is used to provide the conversion formula. The simulation outputs include total short-wave albedo and spectral albedos that are calculated by incorporating the sensor spectral response functions. The procedure is straightforward. Although we explored nonlinear regression analysis, linear regression seems sufficient.

Two indices were used to measure the goodness of fit from any standard multiple regression analysis: a multiple R^2 value indicating the correlation between the predicted and the measured broadband albedos and Residual Standard Error (RSE) indicates the deviation of the points from the regression line.

The linear equation for converting the VIIRS narrowband albedos ρ_i to broadband total short albedo ρ is:

$$\begin{aligned} \rho = & 0.0004 + 0.1722\rho_{M1} + 0.2008\rho_{M2} - 0.2297\rho_{M3} + 0.2630\rho_{M4} \\ & + 0.1524\rho_{M5} + 0.2579\rho_{M7} + 0.0886\rho_{M8} + 0.0866\rho_{M10} + 0.0222\rho_{M11} \end{aligned} \quad (\text{A1})$$

The fit with the simulation results is very good (see Fig. A1).

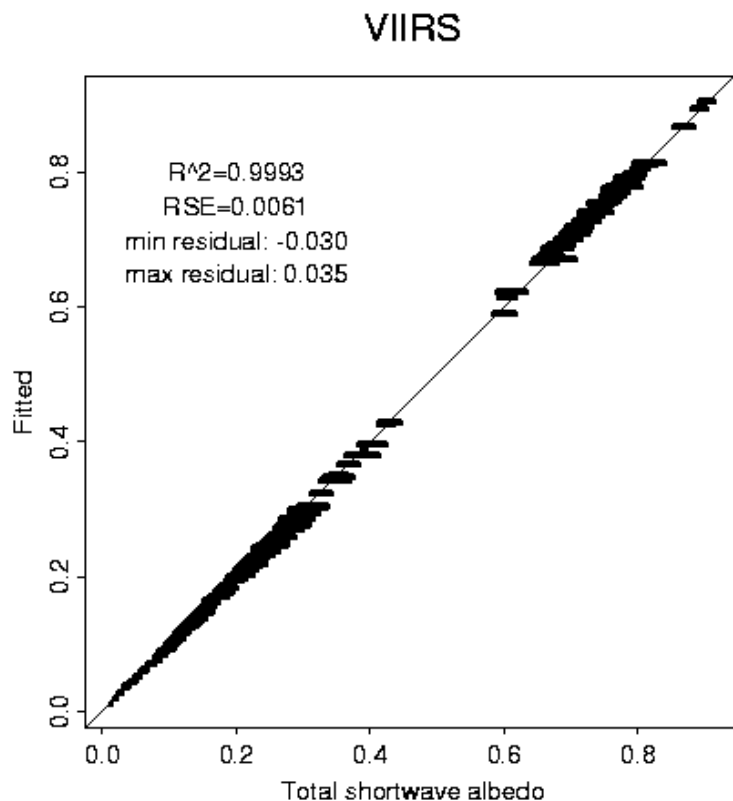


Figure A1 Fit using a linear regression Equation (A1).

Considering that VIIRS bands M1 – M3 correspond to MODIS ocean color bands, it is possible that they might be saturated over the land for some surface types. As an exercise, we fitted the simulation data using only 6 bands, and the resulting equation is:

$$\rho = -0.0012 + 0.4268\rho_{M4} + 0.1334\rho_{M5} + 0.2305\rho_{M7} + 0.1436\rho_{M8} - 0.0131\rho_{M10} + 0.0453\rho_{M11} \quad (A2)$$

Its fitting result is shown in Fig. A2, which is slightly worse than Equation (A1) but not significant statistically.

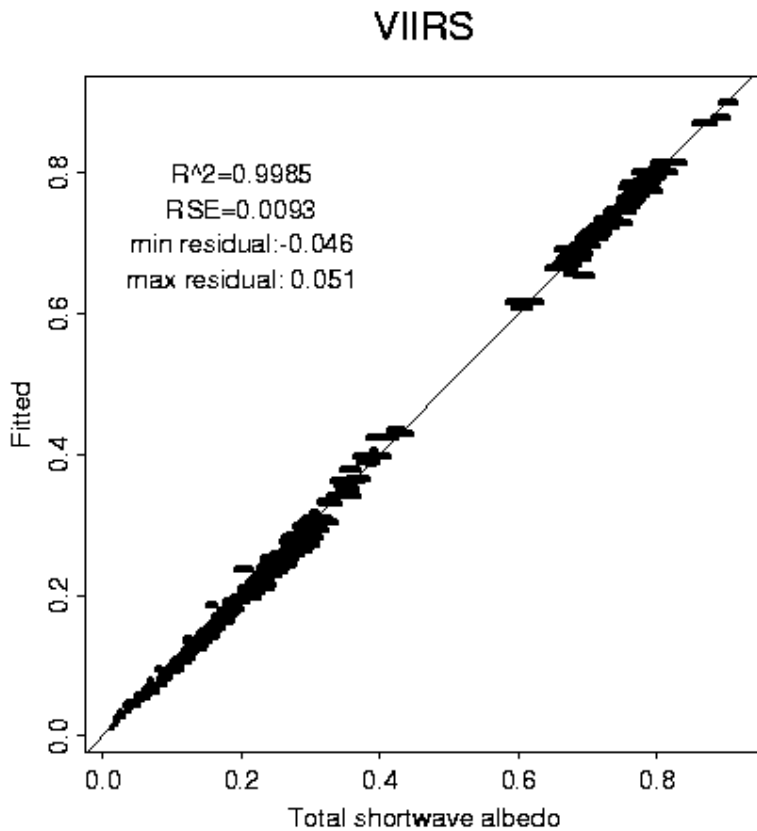


Figure A2 Fit using Equation (A2)

It is evident from figures 1 and 2 that the linear regression equations of (1) and (2) can summarize the simulated data extremely well. However, it does not mean these formulae are perfect for actual applications. Theoretical simulation may not represent the reality very well. Validation using independent ground measurements is critically needed (Liang et al., 2002a; Liang et al., 2003a; Lucht et al., 2000).

References

- Liang, S., 2001, Narrowband to broadband conversions of land surface albedo. *Remote Sensing of Environment*, **76**, 213-238.
- , 2003a, *Quantitative Remote Sensing of Land Surfaces*. John Wiley & Sons, Inc., 534 pp.
- , 2003b, A direct algorithm for estimating land surface broadband albedos from MODIS imagery. *IEEE Transactions on Geosciences and Remote Sensing*, **41**, 136-145.
- Liang, S., Shuey, C., Fang, H., Russ, A., Chen, M., Walthall, C., Daughtry, C., and Hunt, R., 2003b, Narrowband to broadband conversions of land surface albedo: II. Validation,. *Remote Sensing of Environment*, **84**, 25-41.
- Liang, S., Fang, F., Chen, M., Shuey, C., Walthall, C., Daughtry, C., Morisette, J., Schaaf, C., and Strahler, A., 2002a, Validating MODIS land surface reflectance and albedo products: Methods and preliminary results. *Remote Sensing of Environment*, **83**, 149-162.
- Liang, S., Fang, H., Kaul, M., Van Niel, T. G., McVicar, T. R., Pearlman, J., Walthall, C. L., Daughtry, C., and Huemmrich, K. F., 2003a, Estimation of land surface broadband albedos and leaf area index from EO-1 ALI data and validation. *IEEE Transactions on Geoscience and Remote Sensing*, **41**, 1260-1268.
- Lucht, W., Schaaf, C. B., and Strahler, A. H., 2000, An algorithm for the retrieval of albedo from space using semi empirical BRDF models. *IEEE Transactions on Geoscience and Remote Sensing*, **38**, 977-998.
- Ricchiazzi, P., Yang, S., Gautier, C., and Sowle, D., 1998, SBDART: A research and teaching software tool for plane-parallel radiative transfer in the earth's atmosphere. *Bull. Amer. Meteor. Soc.*, **79**, 2101-2114.

APPENDIX B

THE BPSA ALGORITHM FOR ESTIMATING LAND SURFACE BROADBAND SHORTWAVE ALBEDO FROM VIIRS

The VIIRS dark pixel sub-algorithm (DPSA) is largely built on the MODIS albedo algorithm (Lucht *et al.*, 2000; Schaaf *et al.*, 2002). It consists of a series of steps in the processing chain as illustrated in Figure B1: including atmospheric correction, angular modeling for calculating spectral (narrowband) albedos, and narrowband-to-broadband albedo conversions.

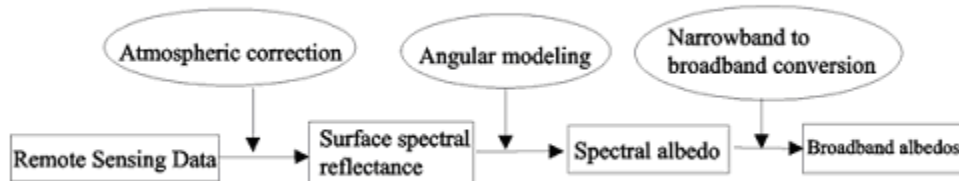


Figure B1 Illustration of the DPSA Algorithm

The bright pixel sub-algorithm (BPSA) evolved from previous studies (Liang *et al.*, 1999; Liang, 2003b; and Liang *et al.*, 2005) employing extensive radiative transfer simulations using SBDART radiative transfer code (Ricchiuzzi *et al.*, 1998), and secondly linking the simulated TOA reflectance with surface broadband albedo using multivariate regression analysis.

A. Radiative Transfer Simulations

For a given atmospheric and surface condition, we need to know the directional reflectance at the top of the atmosphere. Many radiative transfer packages are available right now for us to achieve that, such as MODTRAN, 6S, and SBDART. SBDART (Ricchiuzzi *et al.*, 1998) is used in this study.

A key element is to incorporate reflectance surface reflectance spectra as much as possible. In total, we employed 390 surface reflectance spectra of various surface cover types in this study, such as soil, vegetation canopy, water, wetland, beach sand, snow and ice, urban, road, and rock. They have different wavelength dependences and magnitudes, from coastal water (low albedos) to snow and frost (high visible albedos). It represents the most comprehensive surface reflectance spectra database we could assemble.

In the SBDART simulations, five atmospheric visibility values (10, 15, 20, 25, 30, 50km) were used for different aerosol loadings, four aerosol models (rural, urban, oceanic, and tropospheric) with the US62 atmospheric profile. The solar zenith angle varies at 17 discrete values, the viewing zenith angle at 16 values and the relative azimuth angle at 11 values.

For each surface and atmospheric condition, SBDART simulates the directional reflectance at the top of the atmosphere as well as the downward flux at the bottom of the atmosphere. The downward spectral fluxes are used to generate broadband albedo. Note that since we assume the surface is Lambertian, surface reflectance spectra are numerically equivalent to albedo spectra.

B. Multivariate regression analysis

As long as the database is created from the simulations described above, the next step is to link TOA reflectance to land surface broadband albedo. The sun-viewing geometry parameters are not variables and are provided with high accuracy through the geo-location process. For each solar and viewing angular bin, we can develop a linear regression formula.

The simulated TOA reflectance values were integrated with the sensor spectral response functions of 9 VIIRS bands (M1-M5, M7-M8, M10-11) that are used for predicting surface broadband albedo. Mathematically,

$$\alpha = f(\rho_1, \rho_2, \dots, \rho_n) \quad (B1)$$

where α is surface broadband short-wave albedo from 400nm to 4000nm, ρ_i is the TOA reflectance ρ_i^{TOA} corrected by water vapor and ozone absorption:

$$\rho_i = \rho_i^{TOA} / (T_w T_{oz}) \quad (B2)$$

T_w and T_{oz} are the transmittance of water vapor and ozone in both solar incident and viewing paths.

The sun-viewing geometry was divided into 1992 angular grids, corresponding to 17 solar zenith angle steps, 16 viewing zenith angle steps and 11 relative azimuth angle steps. For each angular grid, one set of coefficients is provided for the linear Equation (B1).

Extensive experiments were conducted to come out the best set of equations. Four scenarios are reported here. The first case applies to the situation that there are only TOA reflectance and sun-viewing geometry parameters. The second case applies when we know the aerosol models. The third case is similar to case one except that only non-vegetated surfaces are considered. The last case is similar to case three with the assumption that the aerosol model is known. We separated non-vegetated surface spectra using the threshold value that the surface NDVI < 0.23.

In the first case, all simulated broadband albedos and TOA reflectances at each angular bin are used for regression analysis. In the second case, regression analysis was conducted four times corresponding to four aerosol models. The last two cases are the similar to the first two cases but only considering non-vegetated surfaces.

Two measures are used to evaluate the fitness of the linear regression models: square value of the correlation coefficient (R^2) and standard deviation (σ) of the residuals that are defined as the difference between the simulated albedo and the fitted albedo. They are provided for each angular bin. The median values for these four cases are shown in the following table. It is not surprising to see that the measures in the second and the fourth cases are much better than the first and the third cases. In calculating these statistics, we have excluded values at two largest solar zenith angles and two largest viewing zenith angles.

Case	σ	R^2
1	0.0369	0.9925
2	0.0119	0.9992
3	0.0311	0.9923
4	0.0103	0.9992

The results are organized into 176 files in four directories respectively: Coeff.lvza.lraa, lvza=1,16, lraa=1,11. In each file, there are 12 lines, corresponding to 17 solar zenith angles (lsza=1,17). For each line, there are 12 elements. The first 10 elements are the coefficients of the linear regression equation with the first element as the intercept constant, the rest coefficients corresponding to 9 VIIRS bands: M1, M2, M3, M4, M5 M7, M8, M10 and M11. The 11th and 12th elements are σ and R^2 .

lvza represents 15 bins (16 steps) of viewing zenith angle:

- 1 0-5
- 2 5-10
- 3 10-15
- 4 15-20
- 5 20-25
- 6 25-30

7	30-35
8	35-40
9	40-45
10	45-50
11	50-55
12	55-60
13	60-65
14	65-70
15	70-75

Iraa represents 10 bins (11 steps) of relative azimuth angle:

1	0-5
2	5-15
3	15-30
4	30-60
5	60-90
6	90-120
7	120-150
8	150-165
9	165-175
10	175-180

The 16 solar zenith angle bins (17 steps) are:

1	0-5
2	5-10
3	10-15
4	15-20

5	20-25
6	25-30
7	30-35
8	35-40
9	40-45
10	45-50
11	50-55
12	55-60
13	60-65
14	65-70
15	70-75
16	75-80

References

- Liang, S., Yu, Y., DeFelice, T. P., 2005, VIIRS narrowband to broadband land surface albedo conversion: formula and validation, *Int. J. Remote Sens.*, vol. 26, no. 5, 1019-1025, 2005. DOI: 10.1080/01431160412331299235.
- Liang, S. (2003b). A direct algorithm for estimating land surface broadband albedos from MODIS imagery. *IEEE Transactions on Geosciences and Remote Sensing*, 41, 136-145.
- Liang, S., Strahler, A., and Walthall, C. (1999). Retrieval of land surface albedo from satellite observations: A simulation study. *J. Appl. Meteor.*, 38, 712-725.
- Lucht, W., Schaaf, C. B., and Strahler, A. H. (2000). An algorithm for the retrieval of albedo from space using semi empirical BRDF models. *IEEE Transactions on Geoscience and Remote Sensing*, 38, 977-998.
- Ricchiazzi, P., Yang, S., Gautier, C., and Sowle, D. (1998). Sbdart: A research and teaching software tool for plane-parallel radiative transfer in the earth's atmosphere. *Bull. Amer. Meteor. Soc.*, 79, 2101-2114.
- Schaaf, C., Gao, F., Strahler, A., Lucht, W., Li, X., Tsung, T., Strugll, N., Zhang, X., Jin, Y., Muller, P., Lewis, P., Barnsley, M., Hobson, P., Disney, M., Roberts, G., Dunderdale, M., Doll, C., d'Entremont, R., Hu, B., Liang, S., Privette, J., and Roy, D. (2002). First operational BRDF, albedo nadir reflectance products from MODIS. *Remote Sensing of Environment*, 83, 135-148.

APPENDIX C

THE BPSA ALGORITHM FOR ESTIMATING SEA ICE SURFACE BROADBAND SHORTWAVE ALBEDO FROM VIIRS

The extension of the BPSA algorithm to sea ice pixels simply requires the derivation of new regression coefficients for sea ice surfaces. These coefficients are derived from simulations of top of the atmosphere reflectances and broadband albedos that we now describe in detail.

Simulated TOA reflectances and broadband albedo values for snow covered sea ice surfaces are required for training the global surface albedo algorithm regression coefficients. Computation of Sea Ice surface BRDF values is complicated by the fact that sea ice is an absorbing and scattering medium which in most cases is covered by a snow layer. Standard Mie scattering computations do not apply in such absorbing media. Northrop Grumman has subcontracted Dr. Knut Stamnes (GEMINOR, Inc) to develop an Ice Snow BRDF (ISBRDF) generation radiative transfer tool for performing computations of BRDF for Snow covered Sea Ice surfaces.

ISBRDF computes bare sea ice BRDFs and performs coupling with snow BRDFs. ISBRDF utilizes tabulated Fourier components of radiation field components based on the Coupled Atmosphere-Sea Ice-Ocean Discrete Ordinance radiative transfer model (CASIO-DISORT). ISBRDF requires input inherent optical properties (IOPs) for both sea ice and snow. Sea ice parameterized IOPs for an absorbing ice medium are generated by the ISIOP (Ice Snow IOP routine; Knut Stamnes) generation software that utilizes as input sea ice physical parameters such as ice thickness, brine pocket size and air bubble size. Snow IOPs are generated by performing Mie computations (snow_mie_driver.pl) utilizing as input the physical parameters for clean and soot contaminated snow such as soot concentration, snow grain size and ice refractive indices. Physical properties for sea ice and snow are shown in tables C1-C2.

Snow and sea ice IOPs generated using MieFast and ISIOP are input to ISBRDF which is run on a LINUX cluster to compute BRDF tables for the wavelengths and geometries defined are shown in tables C5-C6. A flow chart of the process is shown in Figure C1. TOA reflectances and spectral albedo values are computed based on MODTRAN for a range of realistic geophysical surface types, atmospheric conditions, and viewing geometries. The ISBRDF computed BRDF tables are input to MODTRAN for a specified range of snow covered sea ice surface types. Selection and construction of the data fields and inputs required for TOA computation are generated using the Northrop Grumman EVEREST scene simulation software.

Processing Flow

The processing flow for computation of the IOPS, surface BRDFs, albedo and TOA Reflectances and Fluxes is shown in Figure C1. Physical parameters for sea ice and snow

are input to the ISIOP and Snow_mie_driver routines. IOPs generated are input to the ISBRDF routine and BRDF tables are generated as a function of specified wavelength, solar and view geometry for each snow/ice surface type.

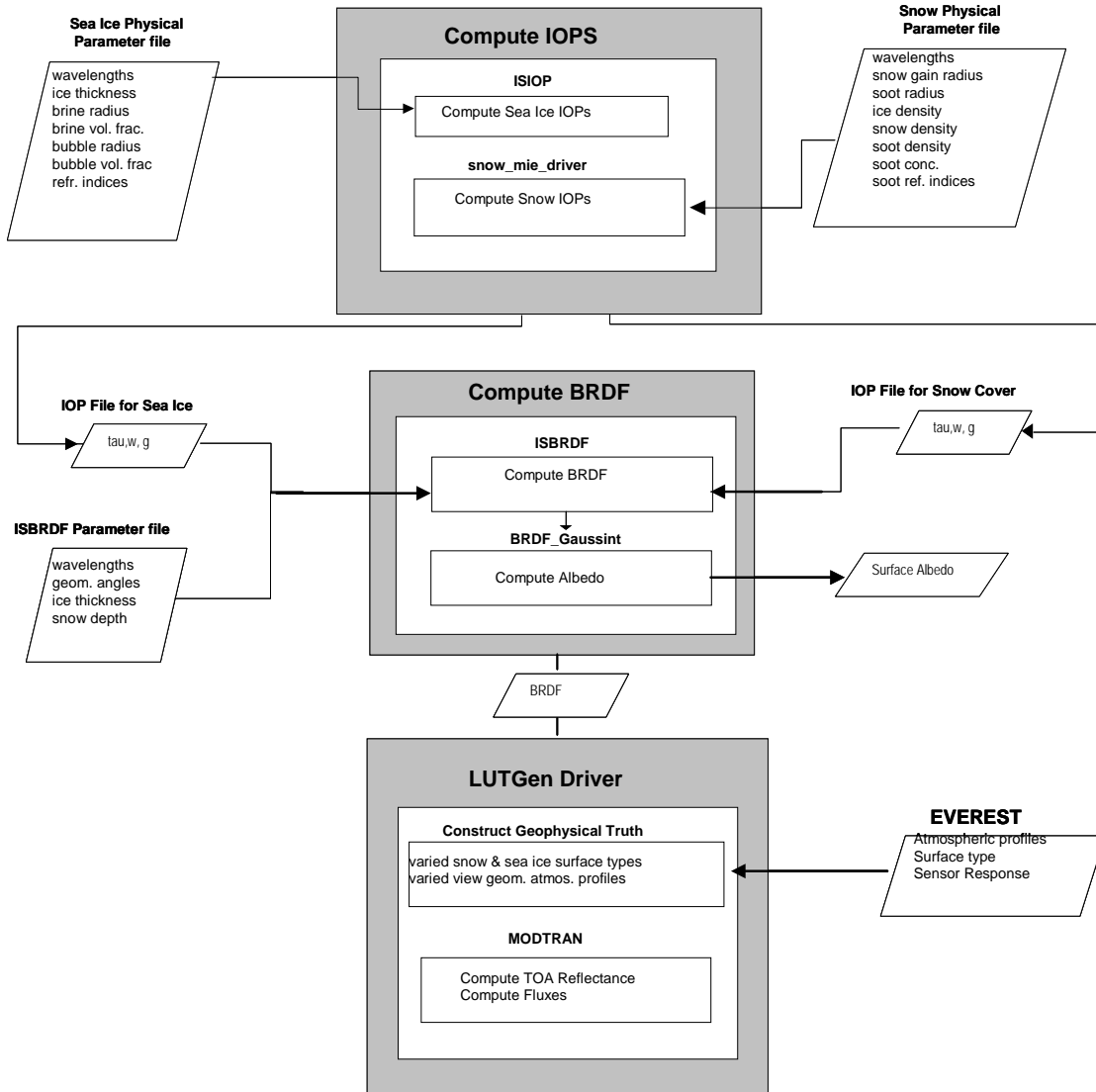


Figure C1. Processing Flow of Snow Covered Sea Ice BRDF and TOA Albedo Generation

Sea Ice Physical Properties

Physical properties representative of three ice thicknesses were defined and utilized to compute sea ice BRDFs (New Young 10 cm, First Year 50 cm, and 150 cm Multi-year ice). The sea ice physical properties listed in table C1 were input to the ISIOP sea ice IOP generation routine.

Table C1 Sea Ice Physical Properties for New Young, First Year and Multi-year ice

Ice Type	Thickness (cm)	Brine pocket vol. fraction	Air bubble vol. fraction	Brine pocket radius (mm)	Air bubble radius (mm)	Impurities vol. fraction	Impurities imaginary refractive index	Ice Temp (C)
MY	150	0.1	0.05	0.5	0.5	1E-06	1E-02	-10
FY	50	0.15	0.01	0.5	0.2	1E-06	1E-02	-5
NY	10	0.25	0.01	0.5	0.2	1E-06	1E-02	-2

The values of the sea ice physical properties listed in Table C1 have been derived from those listed in the report "Development of a Coupled Sea Ice/Atmosphere Radiative Transfer Model" Feb. 22, 2006 written by Dr. Knut Stamnes (GEMINOR Inc.). The ISIOP routine generates as output values of optical thickness, single scattering albedo and asymmetry parameter as a function of wavelength for a given ice type. The IOPs generated are based on parameterized computations performed by ISIOP.

Snow Physical Properties

A generic 250 um grain size snow was defined to characterize snow. Clean snow with no soot impurities was defined for the southern hemisphere. A soot contaminated snow was defined for the northern hemisphere. Table C2 lists the physical properties for snow utilized in the generation of truth albedo values for the global surface albedo algorithm training.

Table C2. Physical Properties of Snow for the Global Surface Albedo Product

Parameter	Value	Units
wavelengths	0.28 - 4.0	um
snow grain size	250	um
ice density	0.917	g/cm ³
snow density	0.3	g/cm ³
optical thickness	2000	Unitless
soot concentration	0.3 northern hemi. 0.0 southern hemi.	ppmw
soot grain size	0.1	um
soot particle density	2.05	g/cm ³
soot real refract. index	1.8	
soot imag. refract. index	0.5	

The routine snow_mie_driver.pl was used to generate the snow IOPs for 500 wavelengths between 0.28 and 4.0 um. The snow_mie_driver.pl routine invoked the routine "refdxice" to compute refractive indices of ice particles which were then input to the MieFast routine which computed the IOPs based on Mie calculations using the input refractive indices and snow grain size. Soot IOPs computations were also performed using MieFast. Dirty snow IOPs were computed as a weighted average of the IOPs for clean snow and soot with weighting based upon the cross-sectional area of the snow grain and soot effective particle radii.

Snow and Sea Ice Surface Type Properties

A range of typical sea ice and snow surface types was defined for performing BRDF computations and are shown in the table below. Sea ice scattering due to brine and air bubbles due to variation in optical properties as a function of ice age. Three sea ice age types are defined as New Young, First Year and Multi-year ice. The albedo of snow surfaces is affected by soot contamination. Northern hemisphere snow surfaces are characterized as soot contaminated snow. A range of snow depths and sea ice thickness has been defined corresponding to ranges of sensitivity.

Table C3. Snow and Sea Ice Surface Parameter Ranges

Ice Type	NY	FY	MY						
Ice Thickness (cm)	10	50	150						
Snow Depths (cm)	0	2.5	0.5	1.0	2.0	3.0	5.0	10	20
Soot Concentration (ppmw)	0.0	0.3							

Inherent Optical Property Computations

ISIOP performs computations of the Inherent Optical Properties (IOPs) for sea ice. ISIOP can also generate IOPs for snow however, the IOPs generated by the snow_mie_driver routine resulted in computed snow BRDF and albedo values that closely matched those published by Warren and Wiscombe. Therefore, ISIOP has been utilized to generate only the sea ice IOPs where a Mie based computed IOPs cannot be performed due to ice being an absorbing medium. The parameter files used for the ISIOP sea ice computations are listed below.

1. ice_ny_0.28-4um.prm

```
500 // Number of wavelengths to be calculated
0.28e-6 // Start wavelength (m)
4.0e-6 // Stop wavelength (m)
// INPUT FOR SNOW:
300 // Density of snow (kg/m3)
250e-6 // Effective radius of snow grains (m)
1.0 // Snow depth (m)
0.03 // Internal vol. frac. of liquid water in snow
1e-2 // lmag.ref.indx. at 0.4um of impurit. in snow
1e-6 // Internal vol. frac. of impurities in snow
// INPUT FOR ICE:
-2.0 // Mean temperature in ice (deg)
0.25 // Volume fraction of brine in ny ice
0.01 // Volume fraction of air in ice
0.5e-3 // Effective radius of brine pockets (m)
0.2e-3 // Effective radius of bubbles (m)
1.0 // Ice thickness (m)
1.0e-2 // lmag.ref.indx. at 0.4um of impurit. in ice
1.0e-6 // Internal volume fract. of impurities in ice
```

2. ice_fy_0.28-4um.prm

```
500 // Number of wavelengths to be calculated
0.28e-6 // Start wavelength (m)
4.0e-6 // Stop wavelength (m)
// INPUT FOR SNOW:
300 // Density of snow (kg/m3)
250e-6 // Effective radius of snow grains (m)
1.0 // Snow depth (m)
0.03 // Internal vol. frac. of liquid water in snow
1e-2 // lmag.ref.indx. at 0.4um of impurit. in snow
1e-6 // Internal vol. frac. of impurities in snow
```



```

// INPUT FOR ICE:
-5.0 // Mean temperature in ice (deg)
0.15 // Volume fraction of brine in fy ice
0.01 // Volume fraction of air in ice
0.5e-3 // Effective radius of brine pockets (m)
0.2e-3 // Effective radius of bubbles (m)
1.0 // Ice thickness (m)
1.0e-2 // Imag.ref.indx. at 0.4um of impurit. in ice
1.0e-6 // Internal volume fract. of impurities in ice

3. ice_my_0.28-4um.prm
500 // Number of wavelengths to be calculated
0.28e-6 // Start wavelength (m)
4.0e-6 // Stop wavelength (m)
// INPUT FOR SNOW:
300 // Density of snow (kg/m3)
250e-6 // Effective radius of snow grains (m)
1.0 // Snow depth (m)
0.03 // Internal vol. frac. of liquid water in snow
1e-2 // Imag.ref.indx. at 0.4um of impurit. in snow
1e-6 // Internal vol. frac. of impurities in snow
// INPUT FOR ICE:
-10.0 // Mean temperature in ice (deg)
0.10 // Volume fraction of brine in my ice
0.05 // Volume fraction of air in ice
0.5e-3 // Effective radius of brine pockets (m)
0.5e-3 // Effective radius of bubbles (m)
1.0 // Ice thickness (m)
1.0e-2 // Imag.ref.indx. at 0.4um of impurit. in ice
1.0e-6 // Internal volume fract. of impurities in ice

```

Note that the ice thicknesses are defined as 1 m (normalized) values. The actual ice thickness for the three ice types are latter assigned in the ISBRDF computation. Details of the parameterizations used for computing the sea ice IOPs are described in the reference "Development of a Coupled Sea Ice/Atmosphere Radiative Transfer Model" Feb. 22, 2006 written by Dr. Knut Stamnes (GEMINOR Inc.).

Snow IOP Computation

Snow IOPs are computed based on Mie computations using the input refractive indices and effective particle radius values for snow ice grains and soot particles. IOPs are generated using the snow_mie_driver.pl routine which drives the Mie computations for snow and soot particles, generates dirty snow IOPs as weighted averages of clean snow and soot IOPs. Snow_mie_driver.pl computes the refractive indices of ice by invoking the routine "refdxice". The refractive indices and the snow physical parameters are input to the MieFast routine to perform Mie computations. Both "refdxice" and "MieFast" are publicly available USCB IPW tool kit modules available from USCB (The Image Processing Workbench, A James Frew, Santa Barbara, CA, University of California, July 1990, Ph.D. dissertation, <http://www.crseo.ucsb.edu/~ipw2/ftp>).

The computations of IOPs for soot contaminated snow are performed according to weighting by the cross-sectional areas of snow grain size effective radius and soot particle effective radius. The computations are performed using the following basis. The masses of snow ice grains and soot particles are computed using effective particle radius values and the respective particle densities.

$$m_{ice} = \frac{4}{3} \pi \cdot r_{ice}^3 \cdot \rho_{ice} \quad \text{Mass of snow ice grain}$$

$$m_{soot} = \frac{4}{3} \pi \cdot r_{soot}^3 \cdot \rho_{soot} \quad \text{Mass of soot particle}$$

The numbers of snow ice grain and soot particles are computed. The soot concentration (f_{soot}) and the bulk density of snow (ρ_{snow}) are required.

$$n_{soot} = \frac{\rho_{soot} f_{soot}}{m_{soot}}$$

$$n_{ice} = \frac{\rho_{snow}}{m_{ice}}$$

Total cross sectional areas and weighting factors are computed for snow ice grains and soot particles.

$$\sigma_{ice} = n_{ice} \pi \cdot r_{ice}^2$$

$$\sigma_{soot} = n_{soot} \pi \cdot r_{soot}^2$$

$$wt_{ice} = \frac{\sigma_{ice}}{\sigma_{ice} + \sigma_{soot}}$$

$$wt_{soot} = \frac{\sigma_{soot}}{\sigma_{ice} + \sigma_{soot}}$$

Dirty snow single scattering albedo and asymmetry parameter values are computed as weighted averages.

$$\omega_{dirty snow} = wt_{soot} \omega_{soot} + wt_{ice} \omega_{cleansnow}$$

$$g_{dirty snow} = wt_{soot} g_{soot} + wt_{ice} g_{cleansnow}$$

Natural ranges for snow densities are between 0.1 for fine powder snow and 0.5 g/cm³ for old compacted snow. Realistic soot particle densities may actually be closer to 1.0 g/cm³. A footnote discussion with regards to the soot particle density is provided in Warren and Wiscombe reference. It should be noted that for the above computations the same snow density and soot particle density as those in the Warren and Wiscombe reference in order to perform inter-comparisons. A snow density of 0.4 g/cm³ and soot particle density of 2.05 g/cm³ were utilized in the snow_mie_driver.pl computations. It was assumed that southern hemisphere snow is clean snow and northern hemisphere snow is contaminated with 0.3 ppmw of soot.

Surface BRDF Computations (ISBRDF)

ISBRDF is utilized to perform BRDF table computations for input sea ice and snow IOPs and physical parameters. ISBRDF reads CASIO-DISORT generated LUT files that contain the Fourier coefficients for various coupled snow-ice CASIO-DISORT runs. ISBRDF was run with 62 streams using 105 wavelengths, 18 solar zenith angles, 18 view zenith angles and

19 azimuth angles. ISBRDF parameter files are defined for each ice type, thickness, snow depth and soot concentration combination. Clean snow is assigned to Southern Hemisphere locations and 0.3 ppmw snow is assigned to northern hemisphere locations. See table C3 for details.

3 Ice Type/Thickness bins: NY (10 cm), FY (50 cm), MY (150)

9 Snow Depth bins : 0, 2.5mm, 5mm, 1cm, 2cm, 3cm, 5cm, 10cm, 20cm

2 Soot concentrations : 0.0 ppmw (clean snow); 0.3 ppmw dirty snow

For a given set of ISBRDF required surface type definition parameters ISBRDF input files were constructed for each surface type run submitted to a Linux cluster.

ISBRDF Template File Format Example:

NUMBER OF WAVELENGTHS

105

WAVELENGTH VALUES (MICRONS)

0.400	0.425	0.450	0.475	0.500
0.525	0.550	0.575	0.600	0.625
0.650	0.675	0.700	0.725	0.750
0.775	0.800	0.825	0.850	0.875
0.900	0.925	0.950	0.975	1.000
1.025	1.050	1.075	1.100	1.125
1.150	1.175	1.200	1.225	1.250
1.275	1.300	1.325	1.350	1.375
1.400	1.425	1.450	1.475	1.500
1.525	1.550	1.575	1.600	1.625
1.650	1.675	1.700	1.725	1.750
1.775	1.800	1.825	1.850	1.875
1.900	1.925	1.950	1.975	2.000
2.025	2.050	2.075	2.100	2.125
2.150	2.175	2.200	2.225	2.250
2.275	2.300	2.325	2.350	2.375
2.400	2.425	2.450	2.475	2.500
2.550	2.600	2.650	2.700	2.750
2.800	2.850	2.900	2.950	3.000
3.100	3.200	3.300	3.400	3.500
3.600	3.700	3.800	3.900	4.000

NUMBERS OF THETA INCIDENT, THETA REFLECTED, AND PHI

18 18 19

THETA INCIDENT VALUES

0.00	5.00	10.00	15.00	20.00
25.00	30.00	35.00	40.00	45.00
50.00	55.00	60.50	65.00	70.00
75.00	80.00	85.00		

THETA REFLECTED VALUES

0.00	5.00	10.00	15.00	20.00
25.00	30.10	35.00	40.00	45.00
50.00	55.00	60.00	65.00	70.00
75.00	80.00	85.00		

PHI VALUES (NB!!! SOLAR AZIMUTH ANGLE is 180 degrees)

0.00	2.00	4.00	6.00	10.00	15.00	20.00
30.00	60.00	90.00	120.00	150.00	160.00	165.00
170.00	174.00	176.00	178.00	180.00		

OCEAN-ICE-SNOW PARAMETERS:

0.05	! Albedo of the ocean
1	! KEY: KEY=0 for PURE ice, otherwise KEY=1
1.0	! Thickness of ice (m)
1.0	! Thickness of ice for ISIOP calculations (m)

NB!!!! For the PURE ice case keep it always 1.0!

0.0	! Thickness of snow (m)
1.0	! Thickness of snow for ISIOP calculations (m)

DISORT PARAMETERS:

62	! NSTR - the number of stream
----	-------------------------------

Simulated TOA Reflectance Generation Scheme

Simulated TOA reflectance values are computed using MODTRAN for specified surface types and atmospheric conditions and other geophysical conditions for given dates and locations. The LUTgen software is utilized to implement a scheme for selecting the surface type and other conditions. The scheme for specification of the snow/ice surfaces is based on the following criteria. For a given pixel, date, and latitude, and surface temperature below sea water freezing temp. = 271.5 K ice is selected as one of the three ice types: New Young 10 cm, First Year 50 cm or Multi-year 150 cm. The frequency of ice types selected is required to match the frequencies defined in an ice type frequency table that is a function of date and hemisphere. Snow is defined corresponding to a 2 day old grain size (250 um) and density (300 g/cm³). Clean snow is assumed for the southern hemisphere and northern hemisphere snow is assumed to be soot contaminated (0.3 ppmw). Snow depths are varied across a range of sensitivity from 0 cm (bare sea ice) to 20 cm. Beyond 20 cm it was found that the computed surface spectral albedo values varied minimally.

Snow Cover Depth Specification Frequency

Snow cover depth spatial and temporal frequency is specified based on global NCEP snow water equivalent data. The snow water equivalent depth provided by NCEP is in millimeter (units of water equivalent snow depth) needed to be multiplied by 3 to be transformed into actual snow depth. The nearest neighbor available snow depth range bin value that corresponds to an ISBRDF computed BRDF run case file is assigned. As an example, a 1 mm NCEP water equivalent snow depth for equates to a snow depth of 0.3 cm, therefore the ISBRDF snow depth is identified as 0.25 cm. ISBRDF defined snow depth bin values were: 0, 0.25, 0.5, 1, 2, 3, 5, 10 and 20 cm.

Sea Ice Age Type Specification Frequency

Sea ice age type spatial and temporal frequency is specified based on the month and latitude of the truth specification scene. A sea ice age type frequency table has been constructed as a function of month and hemisphere based available sources of data and references. The frequencies are relative in the sense that there may be very little ice in a region, but if there were ice present the relative amounts of each ice type are specified.

Table C4. Northern Hemisphere Relative Ice Age Type Frequencies

	Jan	Feb	Mar	Apr	May	Jun	Jul	Aug	Sep	Oct	Nov	Dec
NY	10	10	10	5	5	5	5	5	5	30	25	10
FY	50	45	45	50	50	50	50	45	20	10	25	40
MY	40	45	45	45	45	45	45	50	75	60	50	50

Table C5. Southern Hemisphere Relative Ice Age Type Frequencies

	Jan	Feb	Mar	Apr	May	Jun	Jul	Aug	Sep	Oct	Nov	Dec
NY	5	10	40	70	60	40	30	20	15	15	10	5
FY	20	20	20	10	20	50	60	75	75	70	70	40
MY	75	70	40	20	20	10	10	5	10	15	20	55

Southern hemisphere sea ice age frequencies were determined by estimating values monthly ice thickness values for the Ross Sea (Figure C2) from the reference DeLiberty and C. Geiger, "Temporal and Regional Variations of Sea Ice Thickness in the Ross Sea During 1995 and 1998."

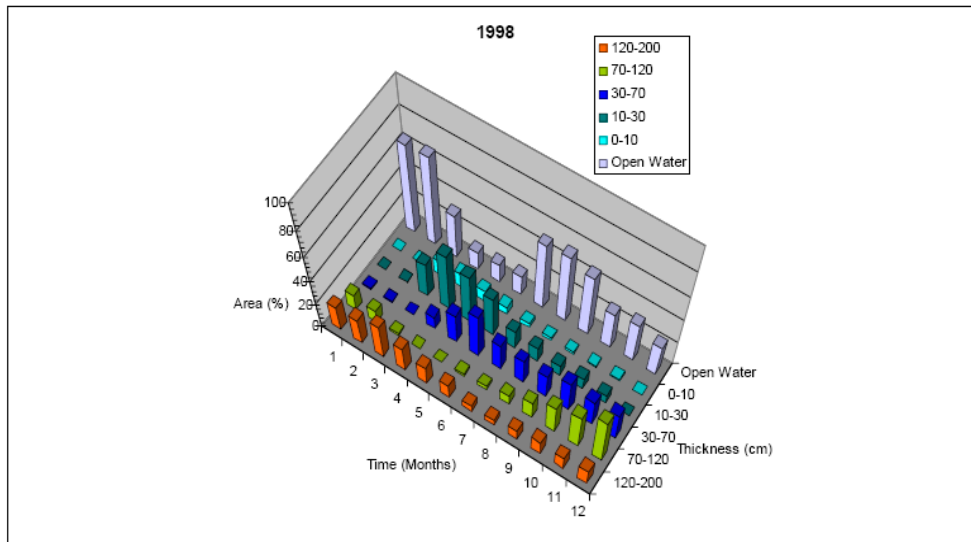


Figure C2: Relative Sea Ice thickness from the Ross Sea used to derive Ice classification for the Southern hemisphere.

The relative amounts of Ice thickness for each month were estimated from Figure C2. The ice thicknesses were binned to New Young (10cm), First Year (50 cm) and Multi-year (150 cm) ice age categories. The process was visually subjective. Northern hemisphere sea ice age type frequencies are based on digitized NIC ice chart partial concentrations for the Arctic provided by the National Snow Ice Data Centre. The process of defining ice age frequencies from the NSIDC partial ice concentration data is outlined below. NSIDC partial ice concentration images of the Arctic for New Young, First Year and Multi-year partial concentrations were processed to produce classification maps. Histograms of the ice age classes for each ice age classification map were used to determine the relative frequency of each ice age class.

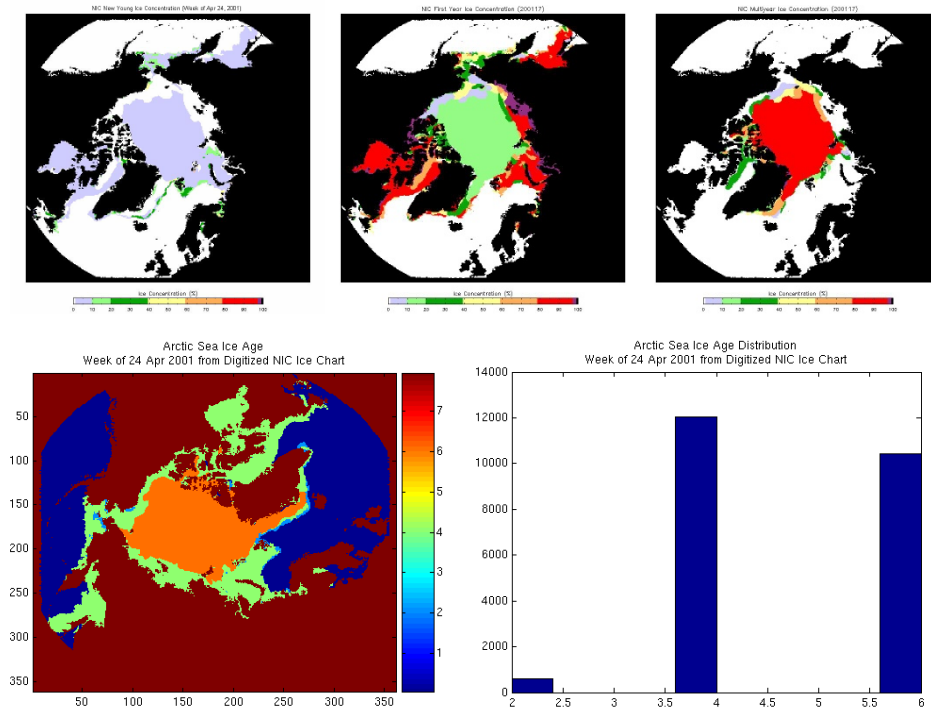


Figure C3. NSIDC partial ice concentrations for New Young (upper left), First Year (upper middle) and Multi-year (upper right). NGST derived ice age classification map (lower left) and histogram of ice age classification map values.

Note the ice age classifications values are defined such that New Young ice is assigned a value of 2, First Year ice has a value of 4 and Multi-year ice a value of 6. Fill values were assigned to 8 and open water as 0. The predominant ice type was determined as the based on upon the ice type with the highest partial concentration.

Verification

A series of test runs were made to verify that the snow BRDF tables generate realistic results. Directional Hemispheric Reflectances were computed using the `brdf_gaussint` routine and compared with published values (Warren and Wiscombe, 1980) the results closely match those of published values. Additional comparisons of Directional Hemispheric Reflectance were made with BRDFs independently computed with the Ice Snow BRDF algorithm (ISBRDF) and ASTER spectral library measurements.

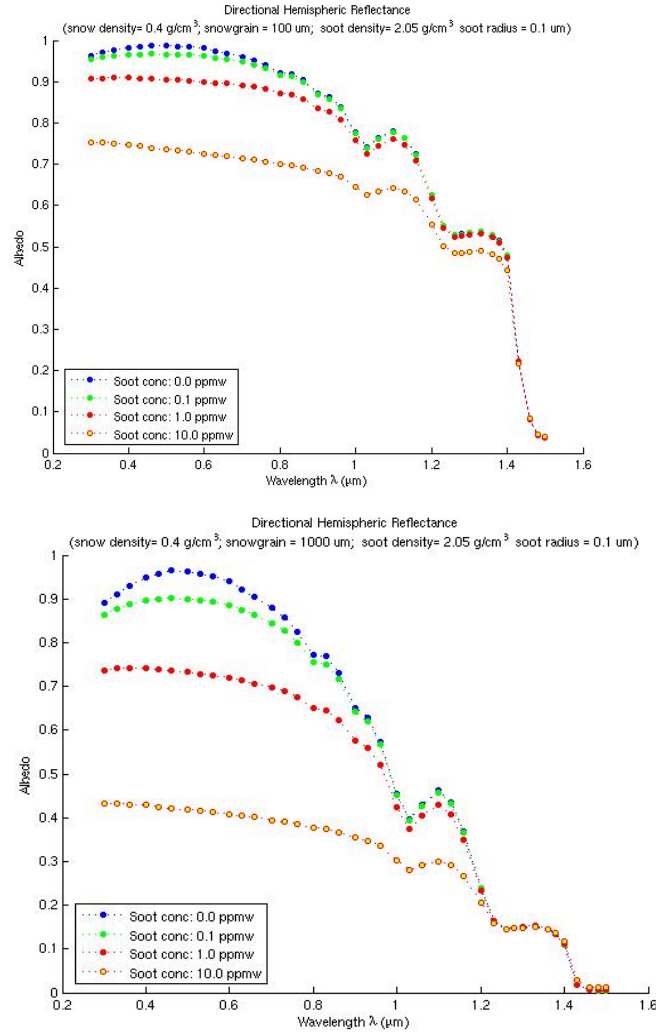


Figure C4: Sensitivity of Directional Hemispheric Reflectance to soot concentration.

Directional hemispheric reflectance (direct beam albedo) is plotted for a) 100 μm and b) 1000 μm snow grain sizes.

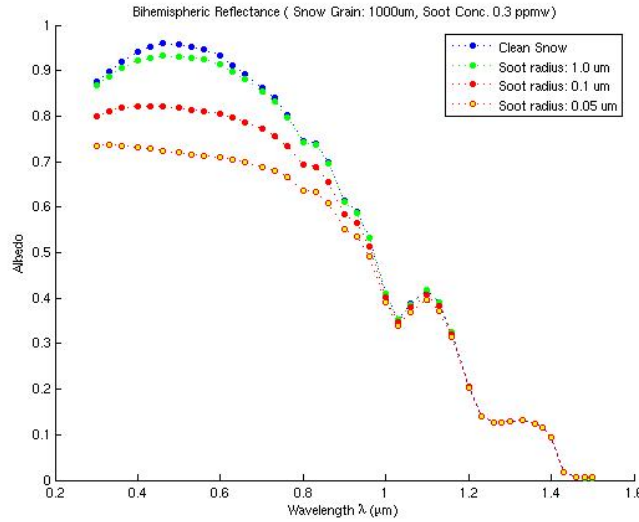
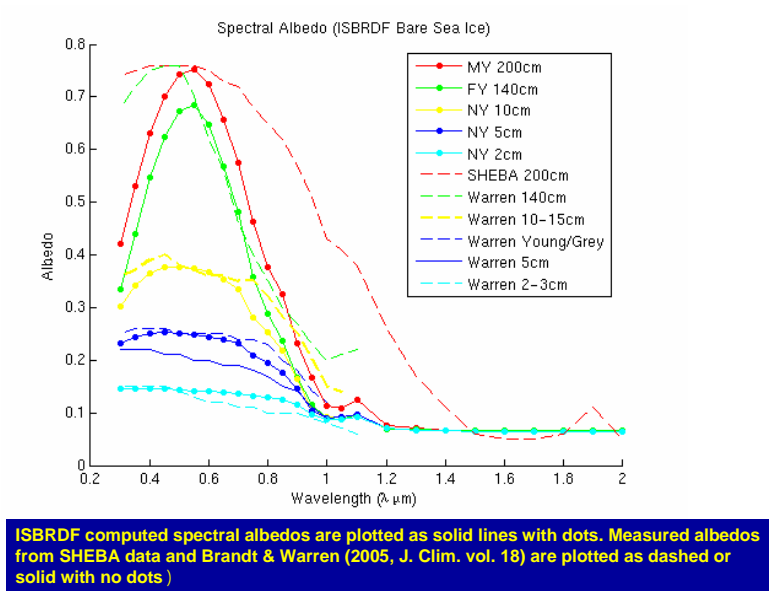


Figure C5: Sensitivity of Bi-hemispheric Reflectance (albedo) to soot particle radius for coarse grain (1000 μm) dirty snow containing 0.3 ppmw of soot. Clean snow albedo is also plotted for reference.

Tests were also performed comparing snow covered sea ice spectral albedo values generated using the ISBRDF routine. The following figures show the comparisons:

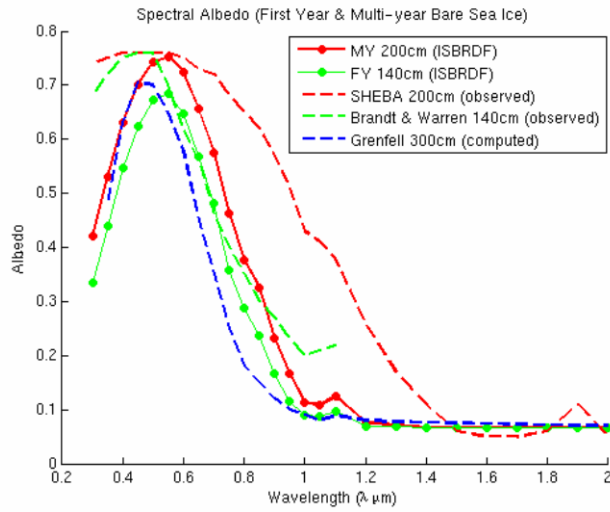
Comparison of Computed and Observed Sea Ice Albedos



ISBRDF computed spectral albedos are plotted as solid lines with dots. Measured albedos from SHEBA data and Brandt & Warren (2005, J. Clim. vol. 18) are plotted as dashed or solid with no dots

Figure C6: Comparison of computed and observed sea ice albedos

Comparison of Computed and Observed Sea Ice Albedos



ISBRDF computed spectral albedos for First Year and Multi-year ice are (solid lines with dots) are compared with albedos from SHEBA data (dashed red), Brandt & Warren (2005, J. Clim. vol. 18, dashed green), and computed albedos from Grenfell (1991, J. Geophys Res. v 96)

Figure C7: Comparison of computed and observed sea ice albedos

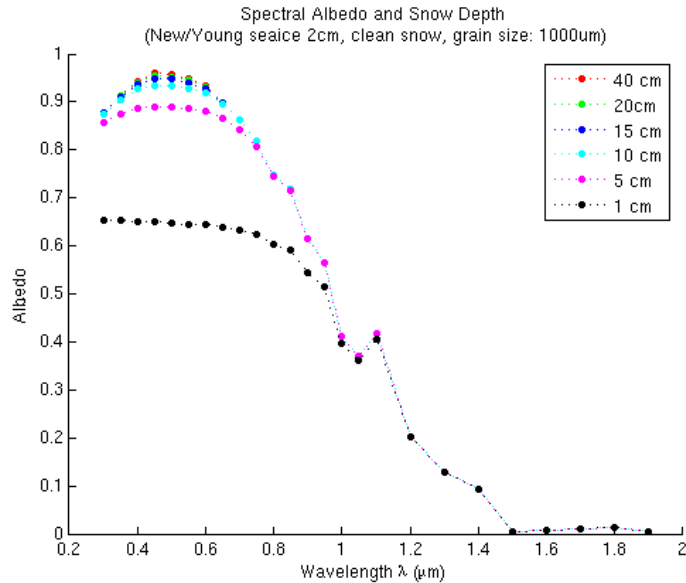
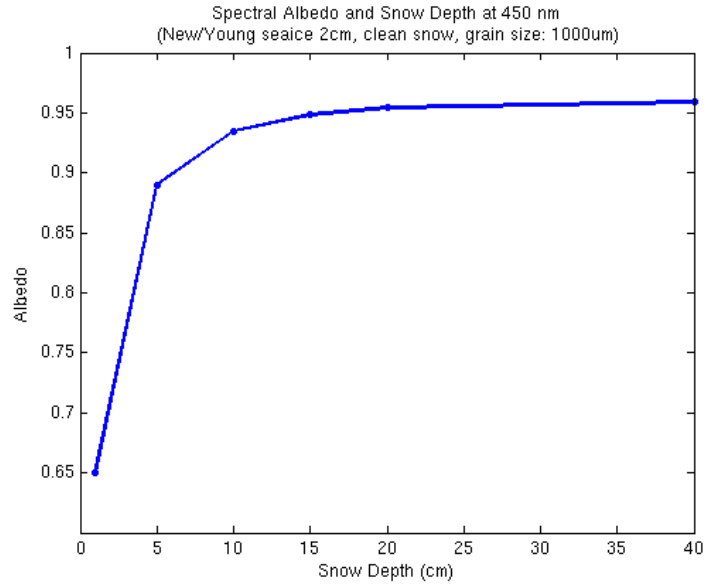


Figure C8: Sensitivity of albedo to snow depth (1)



ISBRDF spectral albedo sensitivity to snow depth at 450

Figure C9: Sensitivity of albedo to snow depth (2)

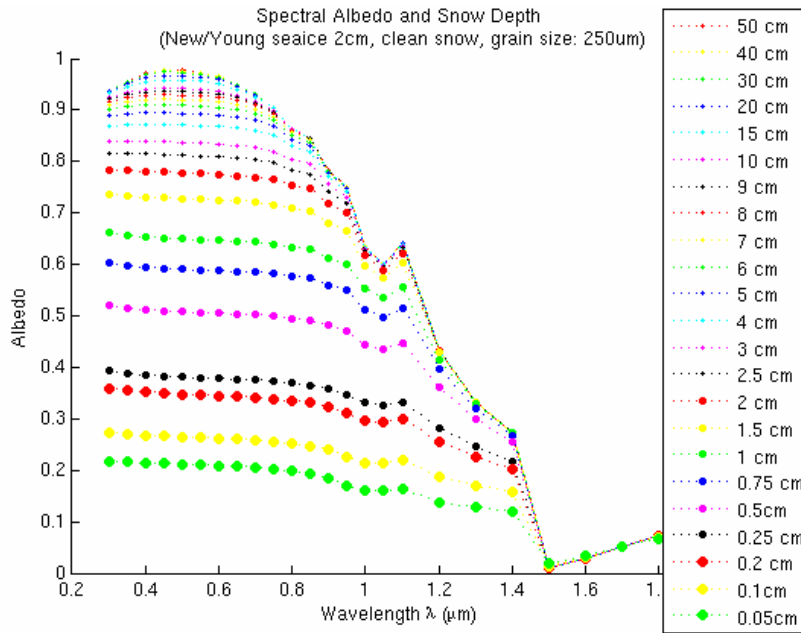


Figure C10: Sensitivity of albedo to snow depth (3)

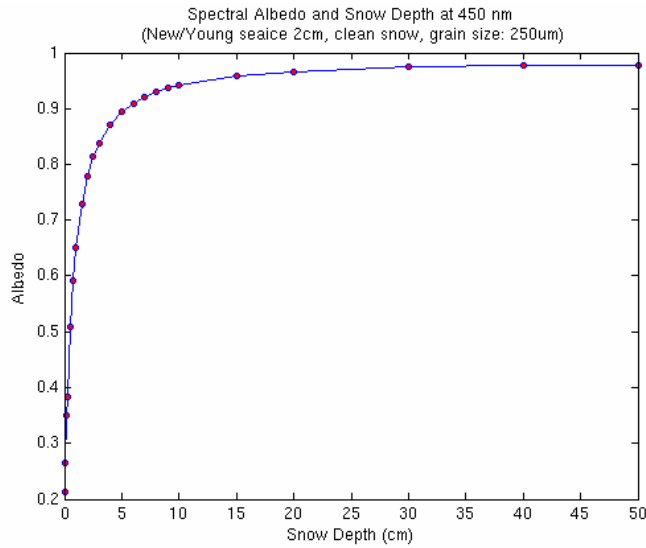


Figure C11: Sensitivity of albedo to snow depth (4)

Procedure for Determining Ice Type Distribution

Several sources of data were utilized to construct the ice type distribution for northern and southern hemispheres. A limited number of digitized ice charts were available and utilized.

Ice Age (Years) derived from NSIDC Digitized Ice Charts

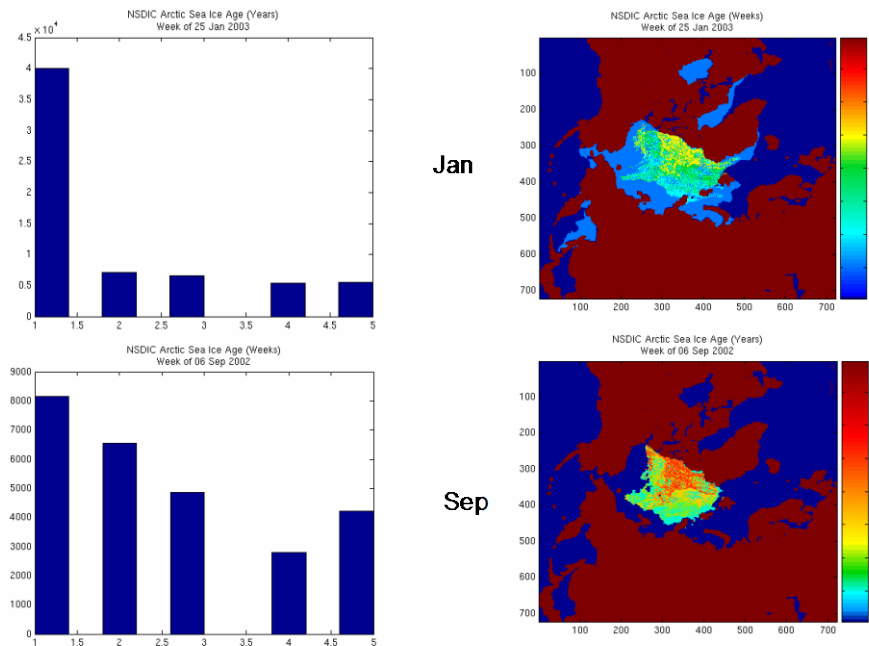


Figure C12: Ice age classification derived from NSIDC Data (1)

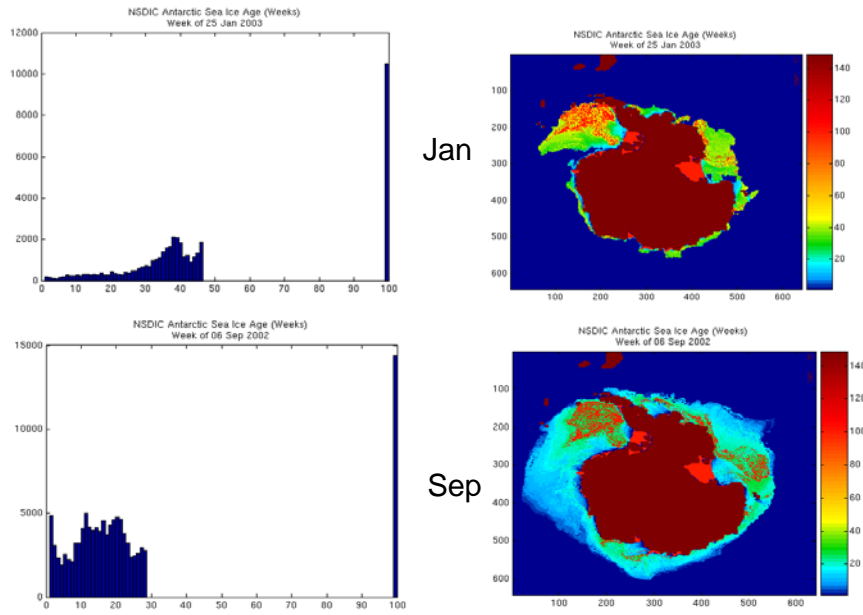


Figure C13: Ice age classification derived from NSIDC Data (2)

Sea Ice Age Class (Arctic, 2001) derived from NSIDC Partial Concentrations

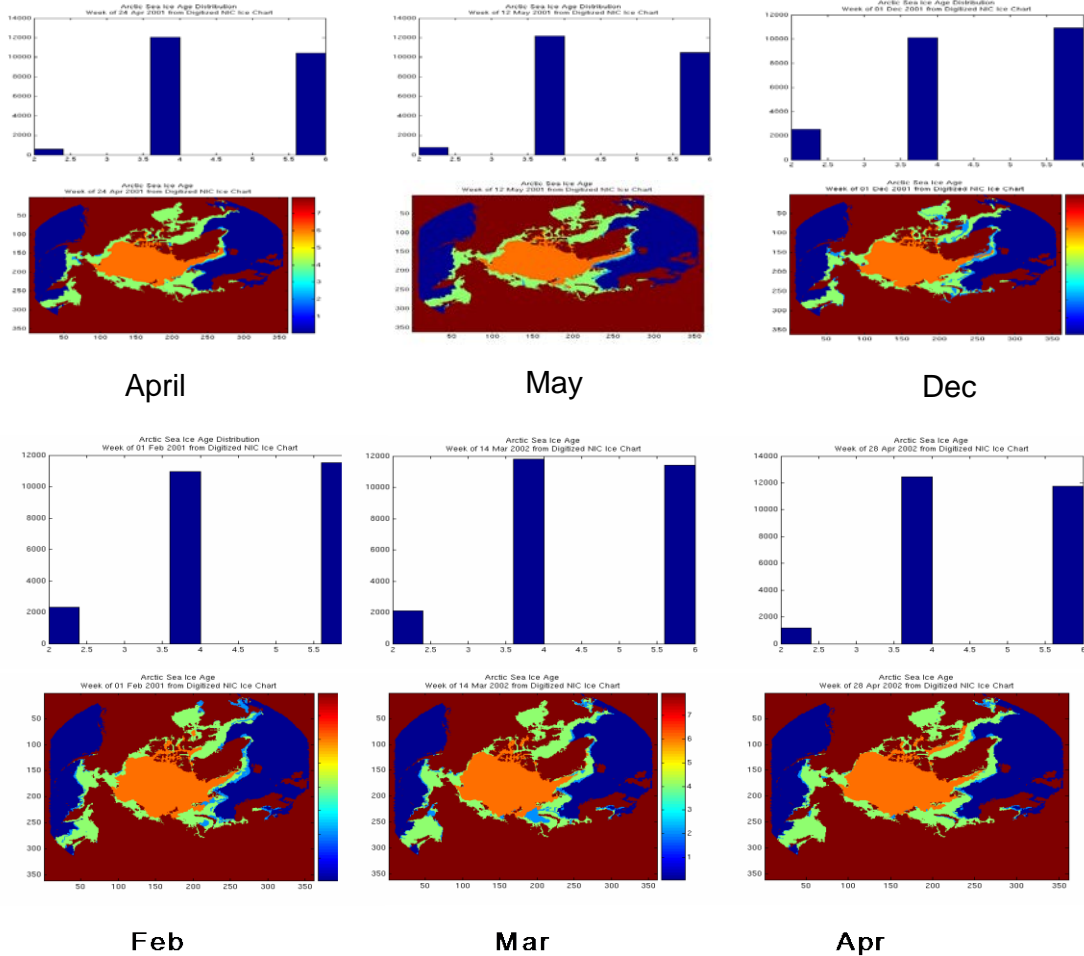


Figure C14: Ice age classification derived from NSIDC Data (3)

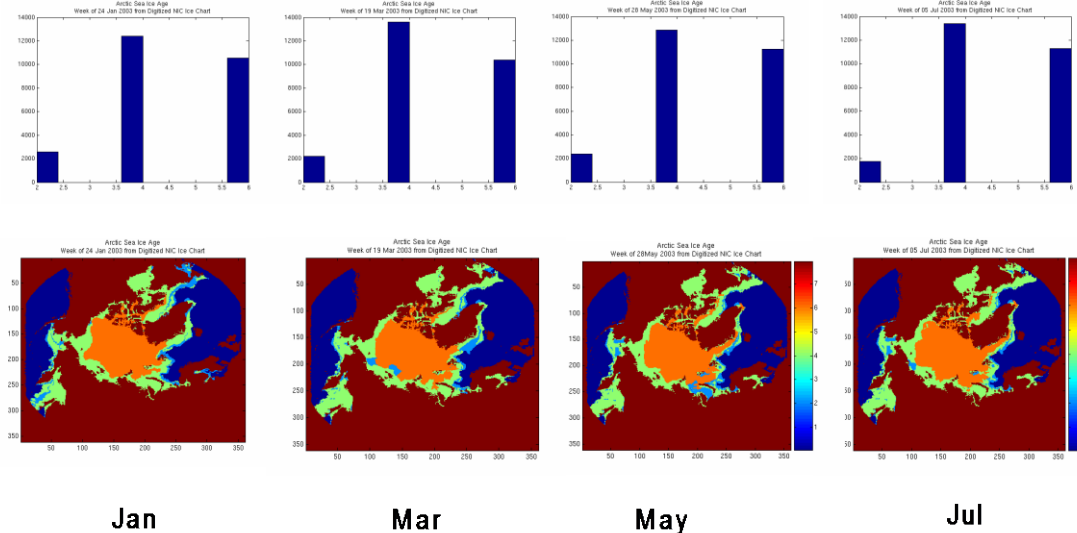


Figure C15: Ice age classification derived from NSIDC Data (4)

TOA Reflectance Computation (MODTRAN)

The MODTRAN radiative transfer code is invoked by the LUTgen software to compute the TOA reflectances. It accounted for the sea ice snow covered BRDF coupling with the atmosphere at the bottom of the atmosphere. The calculation performed on a Linux cluster was run with 16 streams and 5cm⁻¹ spectral resolution. It produced the top of the atmosphere radiances as well as the upwelling and downwelling fluxes at the surface. The broadband albedo was then obtained by computing the ratio of the upwelling and downwelling fluxes which is the exact definition of the albedo as specified in the NPOESS specification.

Global Surface Albedo Algorithm Regression Training

Once the “truth” albedo and the TOA reflectances were computed (after multiplication by each nominal VIIRS sensor response) a simple least squares minimization yielded the regression coefficients. We performed the regression initially on the entire dataset and then proceeded to increase the fit by proceeding by solar angle bins. This can be seen in the increased R² correlation coefficient.

Results without binning in Solar Angles

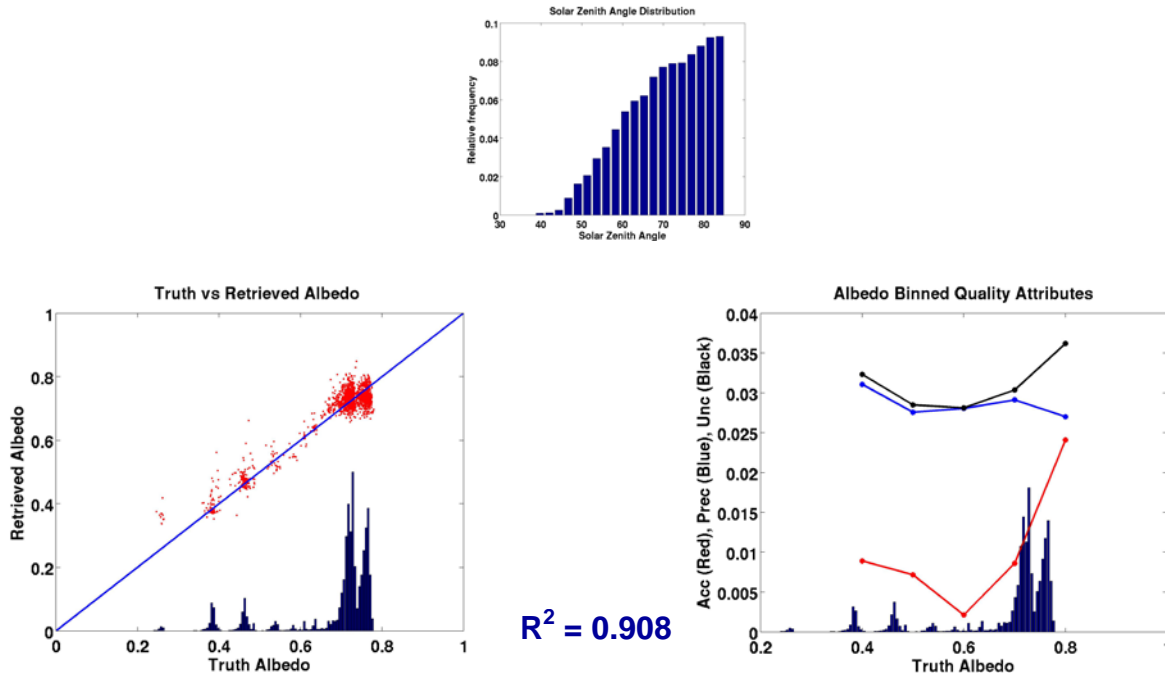


Figure C16: Regression for the entire dataset

Results with binning in Solar Angles

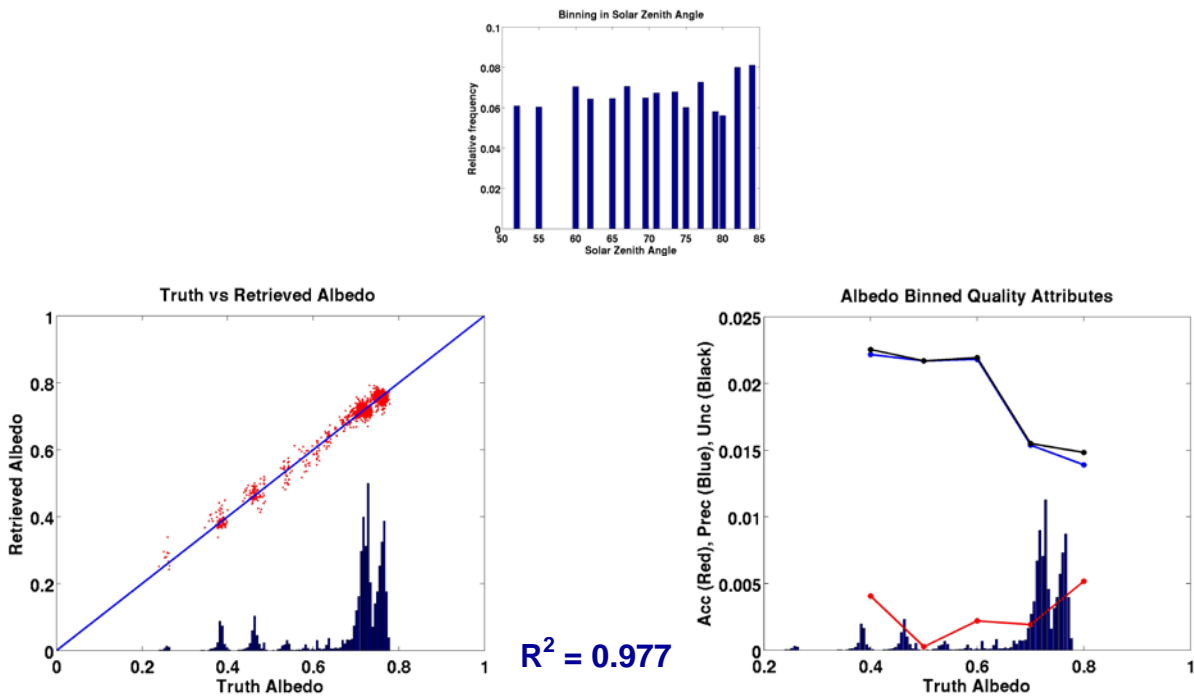


Figure C17: Regression with solar zenith angle binning

References

1. Wiscombe W.J. and S.G Warren, 1980: A Model for the spectral albedo of snow. I: Pure Snow J. Atmos. Sci., 37, 2712-2733
 2. S.G Warren and W.J Wiscombe, 1980: A Model for the spectral albedo of snow. II: Snow Containing Atmospheric Aerosols. J. Atmos. Sci., 37, 2734-2745
 3. Stamnes, K., S-C. Tsay, W. Warren, and K. Jayaweera, Numerically stable algorithm for discrete-ordinate-method radiative transfer in multiple scattering and emitting layered media, Appl. Opt., 27, 2502-2509, 1988.
 4. Frew, J., and J. Dozier, The Image Processing Workbench - portable software for remote sensing instruction and research, Proceedings of the 1986 International Geoscience and Remote Sensing Symposium, ESA SP-254, pp. 271-276, European Space Agency, Paris, 1986.
 5. T. DeLiberty and C. Geiger, Temporal and Regional Variations of Sea Ice Thickness in the Ross Sea during 1995 and 1998, AMS Annual Conference, 2005.
- Liang, S. (2003b). A direct algorithm for estimating land surface broadband albedos from MODIS imagery. *IEEE Transactions on Geosciences and Remote Sensing*, 41, 136-145.
- Liang, S., Strahler, A., and Walthall, C. (1999). Retrieval of land surface albedo from satellite observations: A simulation study. *J. Appl. Meteor.*, 38, 712-725.
- Lucht, W., Schaaf, C. B., and Strahler, A. H. (2000). An algorithm for the retrieval of albedo from space using semi empirical BRDF models. *IEEE Transactions on Geoscience and Remote Sensing*, 38, 977-998.
- Ricchiazzi, P., Yang, S., Gautier, C., and Sowle, D. (1998). Sbdart: A research and teaching software tool for plane-parallel radiative transfer in the earth's atmosphere. *Bull. Amer. Meteor. Soc.*, 79, 2101-2114.
- Schaaf, C., Gao, F., Strahler, A., Lucht, W., Li, X., Tsung, T., Strugll, N., Zhang, X., Jin, Y., Muller, P., Lewis, P., Barnsley, M., Hobson, P., Disney, M., Roberts, G., Dunderdale, M., Doll, C., d'Entremont, R., Hu, B., Liang, S., Privette, J., and Roy, D. (2002). First operational BRDF, albedo nadir reflectance products from MODIS. *Remote Sensing of Environment*, 83, 135-148.

APPENDIX D

THE BPSA ALGORITHM UPDATE FOR PROVISIONAL VERSION RELEASE

The BPSA algorithm has been updated in April 2014, for VIIRS land surface albedo provisional release. This update is basically on the BPSA LUT update, as shown below.

lvza represents 17 bins (18 steps) of viewing zenith angle:

1	0-5
2	5-10
3	10-15
4	15-20
5	20-25
6	25-30
7	30-35
8	35-40
9	40-45
10	45-50
11	50-55
12	55-60
13	60-65
14	65-70
15	70-75
16	75-80
17	80-85

Iraa represents 22 bins (23 steps) of relative azimuth angle:

1	0-5
2	5-10
3	10-15
4	15-20
5	20-30
6	30-40
7	40-50
8	50-60
9	60-70
10	70-80
11	80-90
12	90-100
13	100-110
14	110-120
15	120-130
16	130-140
17	140-150
18	150-160
19	160-165
20	165-170
21	170-175
22	175-180

The 17 solar zenith angle bins (18 steps) are:

- 1 0-5
- 2 5-10
- 3 10-15
- 4 15-20
- 5 20-25
- 6 25-30
- 7 30-35
- 8 35-40
- 9 40-45
- 10 45-50
- 11 50-55
- 12 55-60
- 13 60-65
- 14 65-70
- 15 70-75
- 16 75-80
- 17 80-85